UNIVERSITAT POLITÈCNICA DE CATALUNYA BARCELONATECH

CHALMERS UNIVERSITY OF TECHNOLOGY

Optimisation of Tungsten Ore Processing through a deep Mineralogical Characterisation and the Study of the Crushing Process

Jordi Bascompte Vaquero

Bachelor Thesis

Mineral and Energetic Resources Engineering

Director: OptimOre

Abstract

The unstoppable increasing global demand for metals calls for an urgent development of more efficient extraction and processing methods in the mining industry. Comminution is responsible for nearly half of the energy consumption of the entire mining process, and in the majority of the cases it is far from being optimised. Inside comminution, grinding is widely known for being more inefficient than crushing, however, it is needed to reach liberation at an ultrafine particle size. Sometimes the material is excessively reduced in size, while liberation could be achieved at a coarser scale.

Therefore, in this work a deep characterisation of a specific tungsten ore is performed in order to find guidance in optimising the processing. Either by discarding and avoiding the unnecessary crushing of uneconomic material or any other useful recommendation. The aim is that the methodology utilised for the characterisation of the material, can be applicable to other ores, with the purpose of initiating the optimisation of the mineral processing.

This thesis is divided in two main parts: the mechanical characterisation of the breakage and the mineralogical characterisation. For the first part, the breakage behaviour of the sample material will be studied and described in terms of particle size distribution after interparticle breakage. The latter will be assessed in terms of the different minerals and tungsten concentrations and mineral associations, through the use of image analyses (scanning electron microscope), X-Ray diffraction of crystalline dust and chemical analyses.

The liberation and fracture characteristics that occur due to compressive crushing will be analysed. Furthermore, recommendations in the processing of the ore will be detailed, along with potential problems that should be avoided during its exploitation or the own processing.

Results show that it is possible to obtain ore liberation during coarse comminution. Moreover, preconcentration of the tungsten ore at coarse scale and early rejection of gangue has been determined to be achievable due to the tendency of the ore to concentrate in specific size fractions.

Keywords: tungsten, comminution, compressive crushing, mining, breakage behaviour, mineral characterisation.

Index

1. Introduction

Our society is deeply dependent on the mining industry, more precisely on the so-called Critical Raw Materials. They form a list created by the European Union of strategical mineral commodities of those which Europe should be less dependent on the importation. Most of them are scant in the EU and of poor purity, usually found in low-grade aggregates which need to be processed by means of highly energy consuming separation methods, even in some cases, the exploitation is not possible due to an unfeasible profit margin. In order to achieve dependency on this raw materials, the European mining industry will have to be led to a higher efficiency ore processing.

Tungsten is recognized as a Critical Raw Mineral. In a market currently dominated by China and Russia as the main world producers, in Europe Tungsten production is mostly concentrated in UK, Spain, and Portugal.

The mining industry nowadays is facing several challenges, two of the most notorious are energy efficiency and productivity. Reduction of the ore grade and volatile commodity prices are adding more incertitude to the industry. Due to this facts the mining industry can no longer rely on the strategy of increasing production scale to be able to cope with periods of tight operation margins. Two other strategies are still possible to explore further, reduction of operation costs or improvement of the processing efficiency, this work is based on the later.

Early gangue rejection or preconcentration of the ore at coarse scale based on size has been identified as a feasible operating alternative whereby energy efficiency and unit metal productivity can be greatly increased. This is achieved by understanding and exploiting specific preferential grade responses by size of each ore type. Preferential grade by size refers to the propensity of some ores to naturally concentrate metal into specific size fractions during breakage (CARRASCO ET AL., 2016).

In this bachelor thesis a tungsten ore from a mine site in the West of Spain, named La Parrilla, Cáceres, has been used in all the experimental work. This ispart of a larger EU-funded project named OptimOre: Increasing yield on tungsten and tantalum ore production by means of advanced and flexible control on crushing, milling and separation process.

The research performed through this study can be divided into two main parts. First, the compressive crushing involved Interparticle Bed Breakage (IPB) as EVERTSSON,(2000) presented in his research, and was carried out at Chalmers Rock Processing Research Laboratory. The

second part focuses on the mineralogical characterization of the studied material in both states, previous to the compressive crushing and posterior to it, being divided in particle-size ranges to investigate what happens with the material in each fraction. The mineralogical characterization will be composed of a Scanning Electron Microscope (SEM-EDS) analysis so as to evaluate the liberation of the tungsten minerals in every particle size range, as well as to identify the mineral associated with the ore. Furthermore, a quantitative geochemical analysis of said samples will be performed to know the exact amount of elements in the rock. Conclusively, a semi-quantitative mineralogical analysis will be realized using the X-ray diffraction technique.

2. Goals

The aim of this work is to obtain a detailed characterization of a specific tungsten ore from a mine site in the Iberian Peninsula, and to be a first step for the optimisation of the comminution stage in the mineral processing, with later modelling. This will be achieved by performing a deep mechanical and mineralogical characterization of the ore, to describe how it behaves at any moment. An early pre-optimisation could be achieved if there are conditions that reflect it is possible to reject gangue at coarse scale, especially before arriving in the grinding phase.

The grinding stage is known for its energetic unefficiency. Therefore if we are able to achieve early rejection of gangue, there is no need to reduce the size of uneconomic material, consequently, the energy consumption will be greatly diminished.

An additional aim of this work is to evaluate if mineral liberation occurs at a coarse scale, before entering the milling stages. If that is the case a preconcentration of tungsten ore will be proposed in specific size fractions due to the propensity of some ores to preferentially separate out metal into certain size ranges.

The general idea is to perform experiments on a laboratory scale and carefully measure material characteristics and machine conditions. The experimental conditions obtained from this work, if they are found to be aspects worth considering, will act as an input to improve the functioning of the pilot plant in the Mining Department of the UPC-Manresa.

3. State of art

3.1. Geology

The La Parrilla Project is located in the Autonomous Community of Extremadura, on the border of the provinces of Caceres and Badajoz, about 310 km southwest of Madrid and 240 km north of Seville. The nearest towns are Mérida to 50 km and Miajadas to 15 km and it is, located almost entirely in the municipality of Almoharín, in the province of Caceres

The Autonomous Community of Extremadura is considered a metallogenic and mining region of great importance for the richness and variety of its minerals. The mining activity in Extremadura began in the Roman period, whose most important stage coincides with the mining development of precious metals such as gold and silver. There was also a significant zinc and lead extraction activity at the end of the nineteenth century, coinciding with the national mining boom of the last third of that century (GUMIEL ET AL., 1995).

The La Parrilla Mine, has a total diameter of about 240 m adding up the mine area and the open pit. It is the best European example of mineralized Scheelite veins that fit into rocks of the Upper Proterozoic. The mineral association mainly consists of scheelite, the most important economic mineral, arsenopyrite, cassiterite, wolframite, sphalerite, chalcopyrite, pyrite, pyrrhotine, quartz, muscovite and tourmaline, and weathering products like scorodite, tungstite, limonite, covelline and meymacite (ANAWAR ET AL., 2006). The Scheelite richness of its veins made it known internationally and, along with the Barruecopardo Mine in Salamanca, was the largest tungsten exploitation in Spain, in the 80' it was the second biggest producer of tungsten in Europe (DE LA FUENTE, 2016).

At present, its exploitation is inactive due to the past market conditions of tungsten, although recently opening works have started, to initiate the exploitation again in a near future. At the end of its stage of exploitation, the production was close to the 5,000 tons of Scheelite and the reserves were estimated at about 40 million tons of tungsten ore. The deposit was exploited from 1951 by the companies Minera Bonilla S.A. And Minera Adelaida S.A. Initially the exploitation was underground, being converted to open sky in 1968, in a cut of semi-circular shape that currently most of it is flooded. The mine stopped being exploited in the year 1987 (DE LA FUENTE, 2016).

The mineralized Scheelite veins of La Parrilla undergo a clear structural control since there are several systems of late Hercynian faults that favoured the development of the same, allowing the placement of dikes and the circulation of the hydrothermal fluids that gave rise to the

mineralization. The main mineralized vein set of Scheelite has the NE-SO orientation, with directions between N30ºE and N50ºE, and dips between 45º and 60º towards the SE. The thickness varies from millimetre to 0.6 meters (GUMIEL ET AL., 1995). The veinsare commonly presented discontinuous and the branches are frequent. Subordinates appear crossing reefs with directions NO-SE, that often present and display very verticalized, or with inclinations to the NE or to the SO.

The Parrilla is a classic example of greisen-type deposits of Scheelite related to non-outcropping granite domes (Figure 1), and its mineral association may be considered as a model worldwide (GUMIEL ET AL., 1981). The paragenesis is constituted by Scheelite, which is the main mineral of economic interest of the deposit. Usually, it is yellowish to cream, medium to heavy grain and sometimes well crystallized in small quartz geodes, often filled with clay material. The distribution of the Scheelite in the veins is irregular, appearing in small irregular pockets, in quartz nests, or growing together with quartz, and sometimes together with arsenopyrite and mica. Crystals are rare at the site, but some of several centimetres in length have been found (GUMIEL, 1984).

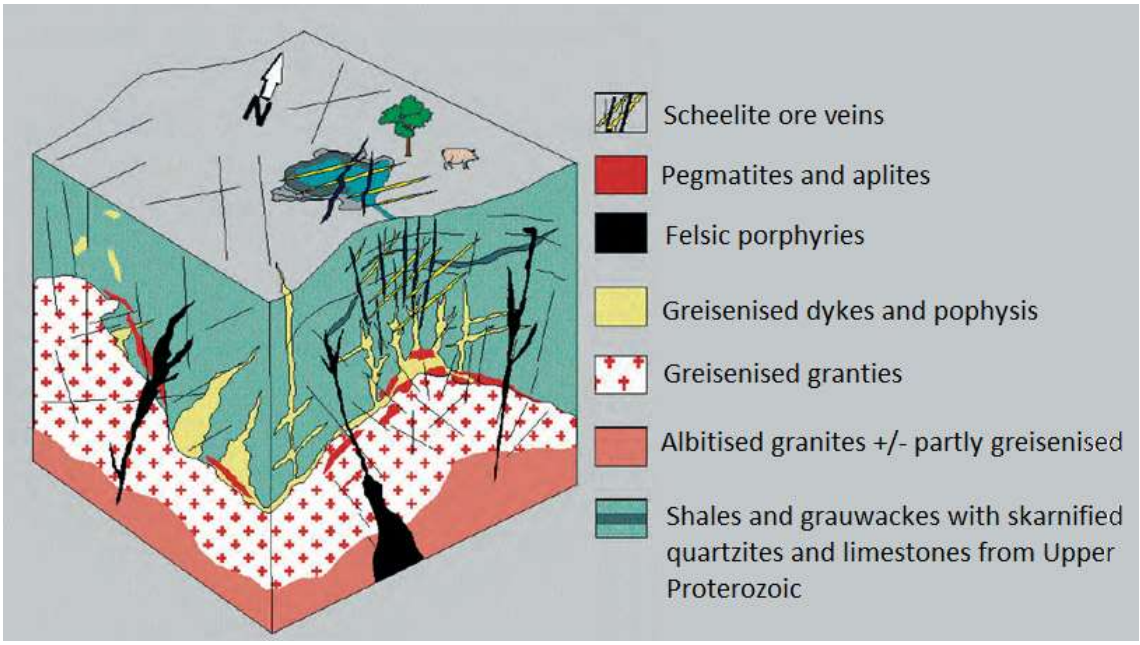

Figure 1. An idealized model of the Scheelite deposit of La Parrilla, in relation to a non-outcropping granite dome(Gumiel et al., 1981).

Cassiterite, also of economic interest in the deposit, is found in a really similar way than the arsenopyrite, located in the centre of the quartz veins, though more frequently, close to the edges. At times, well-developed euhedral crystals occur on bundles of quartz, and are composed by shining prisms between 4 cm and 5 cm of length.

Arsenopyrite is a very abundant mineral in the reservoir. Frequently the crystals are arranged in the quartz or forming geodes along with it. The size varies between millimetres and centimetres. Arsenopyrite frequently appears semi-oxidized to scorodite, but well-formed and shiny isolated crystals are not uncommon, separated from the matrix and with the typical striation of their faces (JUNTA DE EXTREMADURA, 2010).

Genetic considerations about the origin of this mineralization point to the existence of a granite dome in depth, a hypothesis that was confirmed, since a deep granite was cut, in one of the deepest surveys conducted by the Company Rioibex S.A. (GUMIEL ET AL., 1981). An important argument in favour of this hypothesis is also the existence of a contact metamorphism aureole in the fitting materials of La Parrilla Mine. But, in turn, the solutions that originated the mineralization and the granite dome itself may be spatially associated with a shear zone.

3.2. Comminution

In this section, the theoretical background will be presented for different areas of interest in this thesis, giving the reader a framework and introduction so as to follow the discussion and the analysis in upcoming chapters.

Comminution can be defined as the reduction of solid materials from a coarser particle size to a smaller particle size, by crushing or grinding processes. In the past it was referred to finer particles rather than coarser pebbles, however nowadays it refers to all the range from pebbles to minute particles.

The different objectives of comminution processes are to reduce:

- Mine waste to a size where it is transportable by conveyor to a deposit area.
- Coarse ore rocks to a size at which particles of valuable minerals are liberated and can be concentrated efficiently.
- The pebbles of clinker leaving the cement kiln to a size at which the surface area is large enough to optimize the reaction of cement with water.
- The size of mined coal to particles with surface area that will optimize the burning rate.

Waste breakage is a special case that is typically carried out in a single stage using a size breaker and is only practised where the waste characteristics and the geography are suitable.

The first stage of breakage for extracting ores from the deposits is blasting. Blasting is an energy and cost-efficient way of preparing ores for the comminution, which then takes place in a concatenation of crushing and grinding processes.

Crushing reduces the size of the particles from run-of-mine to a size where the mills can generate ore or gangue as separated particles. It is operated dry and in several stages, due to small reduction ranges, the reduction ratio usually goes from 3 to 6. Reduction ratio is understood as the relation between the maximum particle size in the feed and the maximum particle size in the product. Different types of crushers are: gyratory, jaw, cone, impact and roll crushers.

Grinding is the stage where most of the mineral liberation occurs, when the rock material has been reduced to a fine enough size particle will then proceed to the separation phase. Grinding is performed in wet ores because most of the concentration processes are performed as slurries, although for cement and coal it is carried out dry. Grinding occurs when the media such as balls or rods or pebbles, in case of Autogenous Grinding (AG) and Semi-Autogenous Grinding (SAG) mills, contacts the ore inside the mill. More detailed information on grinding can be found in LYNCH (2015).

3.2.1. Comminution Theory

Classical comminution theory focuses on describing the relationship between energy input and the particle size generated from a given feed size due to the energy consumption. The main problem is that generally the machine itself consumes the lion's share of the energy input to a crushing or milling process, and only a reduced fraction of the energy is used in breaking the material. There is a relationship between energy required for breaking the material and the new surface area produced in the process; however, this relationship can only be explained if the energy consumed in creating the new surface can be separately measured (LYNCH, 2015). All comminution theories assume that the size reduced material is brittle, in order that no energy is absorbed in creating contraction or elongation, which is not utilised in the breakage.

There are three principle comminution theories, all of them are versions of the general equation (1) (HUKKI, 1961):

$$E = -K \cdot \frac{dx}{x^n} \quad (1)$$

Where, the energy used is related to the change in particle size.

The first of these three theories was proposed in 1867 by Von Rittinger (2) (VON RITTINGER, 1867), who suggested that the energy consumed by comminution is proportional to the new surface area generated:

$$E = k \cdot \left(\frac{1}{x_2} - \frac{1}{x_1}\right) = k \cdot \left(\frac{1}{p_{80}} - \frac{1}{f_{80}}\right) \quad (2)$$

E is the energy input, f_{80} is the size which 80% of the feed passes, p_{80} is the size which 80% of the product passes and *k* is a constant.

The second classical theory was proposed in 1885 by Kick (3) (KICK, 1885), who suggested that the energy consumed in comminution is proportional to the reduction achieved in volume of the particles:

$$E = k \cdot ln\left(\frac{x_1}{x_2}\right) = k \cdot ln\left(\frac{f_{80}}{p_{80}}\right) \quad (3)$$

The third and last classical comminution theory was proposed in 1952 by Bond (4) (BOND, 1952), who suggested that the energy consumed is proportional to the length of the crack tip generated and is also equal to the difference in energy of the product and the feed:

$$E = k \cdot \left(\frac{1}{\sqrt{x_2}} - \frac{1}{\sqrt{x_1}}\right) = k \cdot \left(\frac{1}{\sqrt{p_{80}}} - \frac{1}{\sqrt{f_{80}}}\right) = Wi \cdot \left(\frac{10}{\sqrt{p_{80}}} - \frac{10}{\sqrt{f_{80}}}\right) \quad (4)$$

Where f_{80} and p_{80} are represented in microns. W_i is the so called Bond Work Index, defined as the amount of energy required, in kWh, to reduce a metric ton of material from a theoretical infinite size in the feed to a product size where 80% passes the 100 µm sieve. It represents the resistance of a given material to size reduction, is often used by manufacturers to approximate the energy required for a particular comminution event.

These three equations are obtained by substituting 2, 1 and 1.5 for *n* in the general equation. HUKKI (1975) suggested that the theories could be applied to different parts of the size reduction curve.

MORRELL (2004) proposed a modification to Bond's equation, although, as LINDQVIST (2008) stated, still lack in precision due to the use of only two points of the size distribution feed and product curves. He, then, proposed a model to calculate the energy consumed in generating a specific product size distribution curve. Other authors have developed methods which work in a similar way (SCHÖNERT, 1990, 2002; LIU, 1996; VOGEL AND PEUKERT, 2003, 2004). Compared to these models EVERTSSON (2000) also developed a form-conditioned crushing model to describe

the behaviour of different rock materials during compressive breakage. Said model will be used later on in this thesis.

Good reviews on the comminution theory are available at LEE (2012) and LYNCH (2015).

3.2.2. Comminution Principles

The three main comminution principles are:

- Compression
- Impact
- Abrasion and attrition

INGLIS (1913) first described the breakage as the initiation and propagation of cracks in rocks that occur at the atomic scale. Likewise, to reduce the particle size of a rock material we have to divide each particle into smaller ones. For a given volume of material, the total surface area increases as the number of particles increases. The increase of the overall surface is a process which is energy consuming, due to an atom on a free surface having a higher potential compared to an atom in the matrix, the creation of a free surface is an energy consuming process EVERTSSON (2000).

During crushing the energy is preserved in the crystal lattice in form of stress, when the stress level exceeds the stress resistance of the material a crack will be generated and propagated, creating a new surface. If there is presence of pre-existent cracks in the rock material, the stress will concentrate there.

Compression

Compressive crushing can be either *force* or *form conditioned*. When it is force conditioned the displacement, and consequently the size reduction, is a function of the applied force. By controlling the force, and therefore the energy input, the size reduction can be controlled. When the form conditioned case takes place, the size reduction and the applied force are a function of the displacement. Size reduction can be controlled by controlling the compression. The energy input and the resulting force are secondary parameters in the form conditioned case. (EVERTSSON, 2000). This is why the energy consumed per unit of size reduced rock mass has to be calculated subsequently or else it is unknown. Crushing machines that use form conditioned compression are: gyratory, cone, roller and jaw crushers (Figure 2).

Breakage by applying compression to a particle bed is the most efficient method of size reduction in terms of energy utilized. Energy is transferred to particles by means of surrounding particles, hence interparticle breakage occurs (LYNCH, 2015). The crushing tests performed in this

thesis use this method. For this reason, more time is dedicated explaining the compressive crushing than the rest.

Out of all the mentioned compression crushers, jaw, cone and gyratory crushers operate cyclically. Particles entering the crushing chambers of these compression crushers are repeatedly nipped and crushed as they pass through the cavity (LEE, 2012). In contrast there are High Pressure Grinding Rolls (HPGRs) and roll crushers (similar to HPGRs but used at higher roll speeds, lower feed rates and lower pressures) where the compression event only happens once.

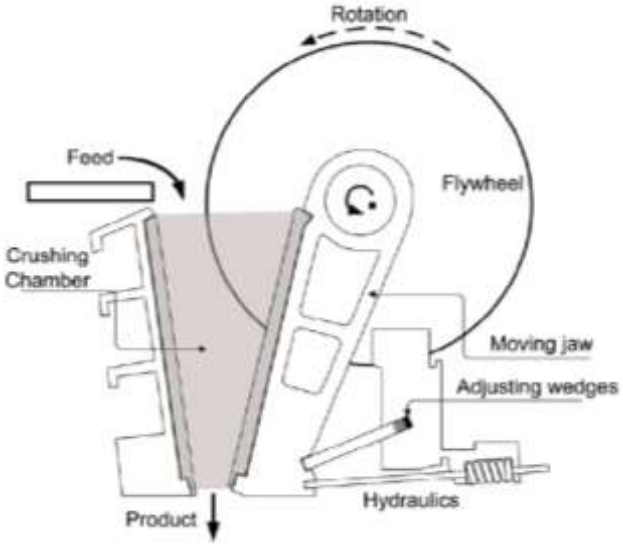

Figure 2. Schematic illustration of a jaw crusher (Quist, 2017).

When the rock is broken using compression the products fall into two main size ranges, which are: coarse particles as consequence of induced tensile stress and fine particles resulting from the breakage near the loading points. PARTRIDGE (1978) stated that often in compressive crushing devices corrugated crushing surface is used, reducing the loading area and hence minimizing the amount of fines generated.

Impact

In the event that a particle is reduced in size by forces acting on the particle, consequence of the kinetic energy of other particles or the grinding media, it is said that impact breakage has occurred. This type of breakage is an energy-controlled form of size reduction. The energy is used in accelerating the particles by a rotor and then letting them impact against a bed of particles or a solid wall, the machine itself (Figure 3). The size reduction accomplished can be controlled by the energy provided to the rotor. Impact crushers are crushing machines that use energy-controlled breakage.

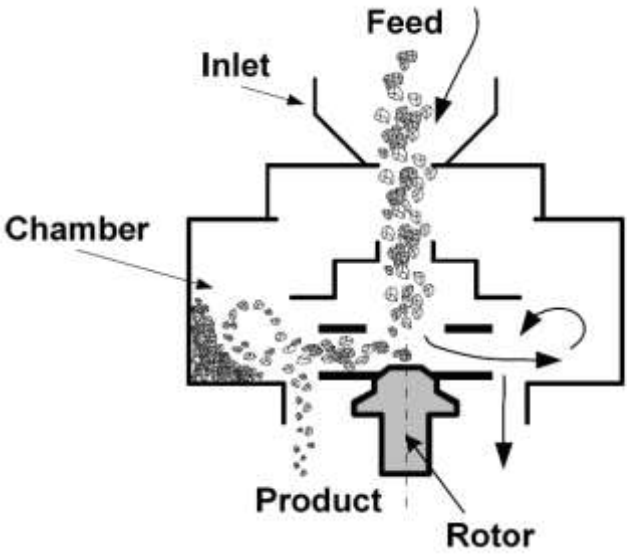

Figure 3. Schematic illustration of a VSI crusher (BENGTSSON, 2009).

When impact breaking takes place, because of the quick loading, the rock experiences a larger average stress than necessary to create a simple fracture and cracks immediately. Usually the product is of similar shape and size.

Abrasion and attrition

Abrasion occurs when the shear forces break the particles due to them rubbing against each other. Grinding media can also generate abrasion by rubbing. It mostly generates fine material. Usually fines generation is unwanted.

Attrition is similar to abrasion. It occurs when a smaller particle is trapped between two larger particles. As the particle edges are chipped and abrasion occurs, the combination is called attrition (LYNCH, 2015).When abrasion happens, it generates particles of a much tinier size than the feed size, the product is usually rounded due to rougher edges being smoothed off.

4. Methodology

4.1. Experimental crushing tests

Test methods to characterize the breakage behaviour of different rock materials can generally be divided into fundamental *rock mechanics tests* and *rock aggregate tests* (often referred to as comminution tests). The focus of rock mechanics tests lies mainly in determining the mechanical properties of a given rock material, whereas the aim of rock aggregate tests is to determine the comminution behaviour of the material (LEE, 2012). A variety of rock aggregate tests will be performed in this study and are explained bellow.

The majority of the comminution tests are energy conditioned, as well as conducted for single particles. Due to that compressive crushers work using a form-conditioned principle instead of energy conditioned, it would be more accurate to perform form conditioned tests. In addition, particles in compressive crushers also break in particle beds, not only single particles (note that HPGRs do not crush single particles), for this reason interparticle breakage should be also characterised. A form conditioned test for particle beds breakage test was developed by EVERTSSON (2000).

In this thesis, EVERTSSON's test procedure will be used for characterizing the breakage behaviour of tungsten ore from a mine site in Spain. The product of said tests will be later separated in different size fractions and mineralogical characterization will be realised out of each size fraction to study the behaviour of the ore under compressive breakage conditions.

4.1.1. Compressive breakage test. Interparticle Breakage (IPB)

Cone and gyratory crushers, and in occasions jaw crushers also, work with a combination of single and interparticle breakage. If the crushers are fed very little there will not be the possibility to form particle bridges and therefore generate interparticle crushing. However, most of the manufacturers, such as the Swedish company of Sandvik say that it is not the correct way to feed a crusher. They recommend that the crusher has to be choke fed, so that there is a level of particles above the crusher, there should be enough material in the crusher so that interparticle breakage takes place together with single particle breakage.

The compression ratio normally is low high up in the crusher, because as can be seen in Figure2 the throw is small at the entrance of the material and the opening is bigger, so the compression ratio is small and very little will happen. The further down the particles go inside the crushing

chamber, the throw is bigger and the opening is smaller, therefore the compression ratio increases.

What happens in a gyratory crusher and in a cone crusher, is because of the conical surface, and the distance between the mobile and fixed parts is decreasing and the cross sectional area is decreasing too, down to a point where it is increasing again. The narrowest section in terms of cross sectional area and flow is not at the outlet, it is in the middle between the inlet and the outlet. So that means that it is getting more and more difficult for material to pass, down to a level and then the crusher is opening up again, the distance is decreasing but the total area is increasing. To form a bed of particles, a certain density of particles is needed, so down to this narrow section single particle, if the particle is big enough, or interparticle, most commonly, can occur. When the particle is opening up again, there may not be enough material to form bridges, so it can only be single particle. However it cannot be confirmed that single particle does most of the crushing, it can only be said that both can happen.

For the characterization of interparticle breakage, the compressive crushing tests were performed using a hydraulic press (Table 1 and Figure 4) by means of a piston and die, following the form conditioned test procedure that first developed by EVERTSSON (2000) and BENGTSSON (2006) adapted for the characterization of single particle breakage.

Table 1. Technical specifications of compression testing system

Model	Instron 400RD
Loading capacity	2000 kN
Maximum stroke	76 mm
Load measurement accuracy	± 1.0% of reading down to 4% of frame capacity
Strain measurement accuracy	± 0.5% of reading down to 1/50 of full range
Position measurement accuracy	± 0.5% or 0.13 mm displacement
Position resolution	1 µm
Max test speed	75 mm/min
Data acquisition rate	1 kHz on load and strain
Diameter of the die	100 mm

Figure 4. Instron 400RD hydraulic compression from the Chalmers University laboratory.

During this form conditioned piston and die tests for interparticle breakage (IPC, also known as bed breakage) measurements of piston displacement, applied compression ratio as well as applied force are continuously logged.

The basic concept of compressive breakage is to analyse the rock behaviour in terms of the breakage, particle size distribution (PSD) and energy consumption after compressive forces. During the compression test, the displacement of the piston and the compression ratio are fixed values, which will allow information such as the generated particle size distribution and the energy used to generate the breakage to be understood and extracted (GULDRIS, 2016). Compression ratio is the quotient of the displacement of the piston over the initial bed height of the sample, and it is explained by equation (5) (EVERTSSON, 2000):

$$S_{s/b} = \frac{s}{b} \tag{5}$$

Where b = bed height

s = piston displacement

s/b = compression ratio

The sample characteristics are appointed by the pre-stablished test procedure. At a material density of around 2.7 g/cm^3, at least 6 kg of the size fraction 8-11.2 mm if bias towards larger particles is to be avoided. Note that in the original test procedure rock particles of the size

fraction 16-19 mm were used, later a switch to 8-11.2 mm particles was made in order to increase the statistical significance of the results.

Due to a lack of material in the range size 8-11.2 mm, the size interval was increased to 8-16 mm. This was consulted with the researcher that adapted the original procedure, BENGTSSON (2006), before being carried out, the large amount of time that would take to send more material from the mine site made this the most suitable solution. Even though the pre-established size range was modified, the statistical significance of the results would still be proper enough.

The compression ratio values and the compression repetitions are appointed by the original test procedure, as well. The test procedure is represented in Figure 5, and explained in detail bellow:

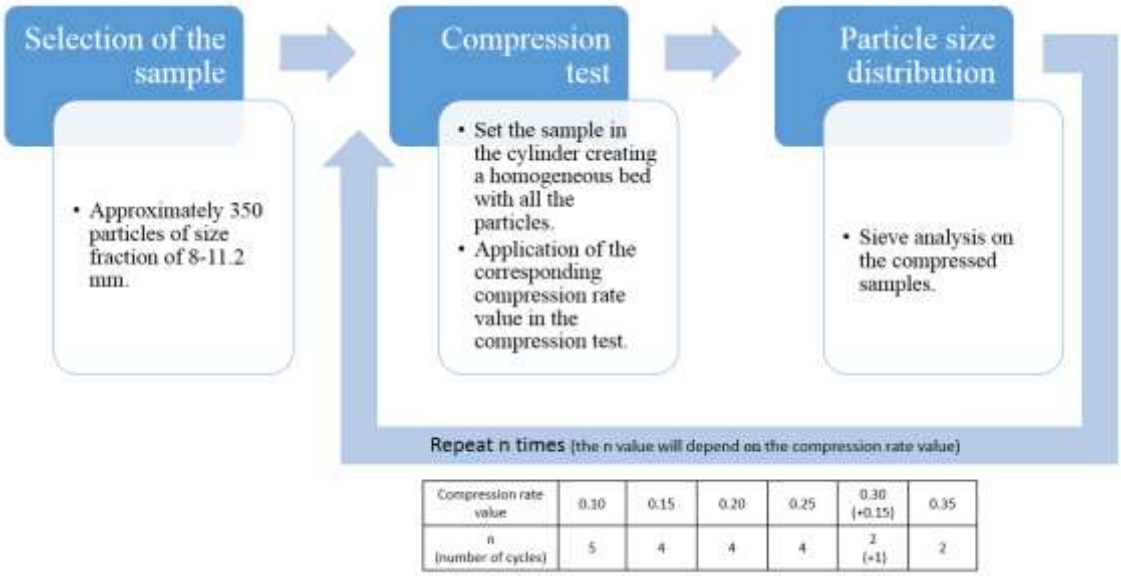

Figure 5. General test procedure for Interparticle Breakage (Guldris, 2016).

Text procedure for IPB

1. Collect sis samples; each containing 350 particles of the size fraction 8-11.2 mm. Weigh the samples and make sure that all samples weigh roughly the same.
2. Pour a sample into the die and easily shake the die to even the surface of particles.
3. Place the piston in the die and measure how much it sinks into the die.
4. Empty the die and repeat 2 and 3 a number of times. Make sure that the piston sinks to its most common level in the last attempt before proceeding to 5.
5. Place the die on the hydraulic press table.
6. Start and continue the compression of the sample until the required compression ratio (Table 2) is attained.
7. Perform sieve analysis on the sample.

8. If additional tests are to be conducted at the same compression ratio, repeat 2-7 with the same sample. Otherwise, start over with a new sample by repeating 2-7 for the remaining compression ratios.

Table 2. Test plan for IPB

Test nº	Test material	Compression ratio [s/b]
1	350 particles of +8/-11.2 mm	0.10
2	from nº 1	0.10
3	from nº 2	0.10
4	from nº 3	0.10
5	from nº 4	0.10
6	350 particles of +8/-11.2 mm	0.15
7	from nº 6	0.15
8	from nº 7	0.15
9	from nº 8	0.15
10	350 particles of +8/-11.2 mm	0.20
11	from nº 10	0.20
12	from nº 11	0.20
13	from nº 12	0.20
14	350 particles of +8/-11.2 mm	0.25
15	from nº 14	0.25
16	from nº 15	0.25
17	from nº 16	0.25
18	350 particles of +8/-11.2 mm	0.30
19	from nº 18	0.30
20	from nº 19	0.15
21	350 particles of +8/-11.2 mm	0.35
22	from nº 21	0.35

There is a similar experimental procedure to the IPB test, adapted by BENGTSSON (2006) from EVERTSSON's IPB named Single Particle Breakage (SPB), as the reader can imagine the main difference is that it the compressive breakage is performed with only one particle at a time. It is used to evaluate the breakage behaviour of single particles in a compressive crushers. As mentioned before, the crushing process in most compressive crushers can be described by dividing the crushing chamber in two main zones. A particle can be broken through interparticle breakage or single particle breakage, interparticle breakage can only occur above the choke level of the crushing chamber, while single particle breakage usually occurs below the choke level (EVERTSSON, 2000; LEE, 2012).

Single Particle Breakage tests could not be performed in this thesis due to a limitation in time, however the author thinks it is highly recommendable for any similar research in the future.

4.1.2. Size Reduction Modelling

In a compressive crusher the feed is transformed to product by a number of reduction steps, which varies between different crushers (HPGRs perform compression crushing with a single compression repetition) and its crushing chamber (Figure 6).

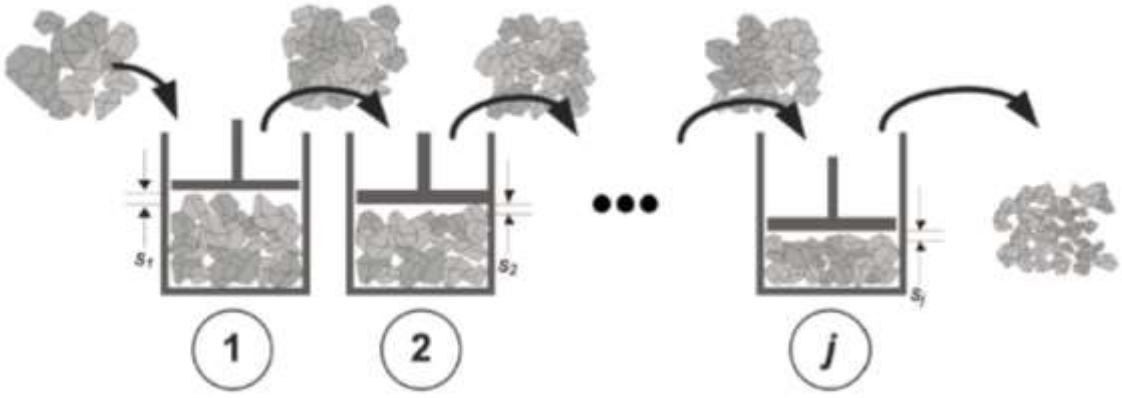

Figure 6. Approximation of a compressive crusher with a series of consecutive compressions (Hulthén, 2006).

It has been shown that for a cone crusher the number of steps can be ten or more (EVERTSSON, 1999). In Figure 7, a model where each reduction is described only by two basic mechanisms is shown; it is believed that they can describe all the aspects of breakage behaviour: selection and breakage (Evertsson, 2000). The feed for a crushing event is the product of the previous one.

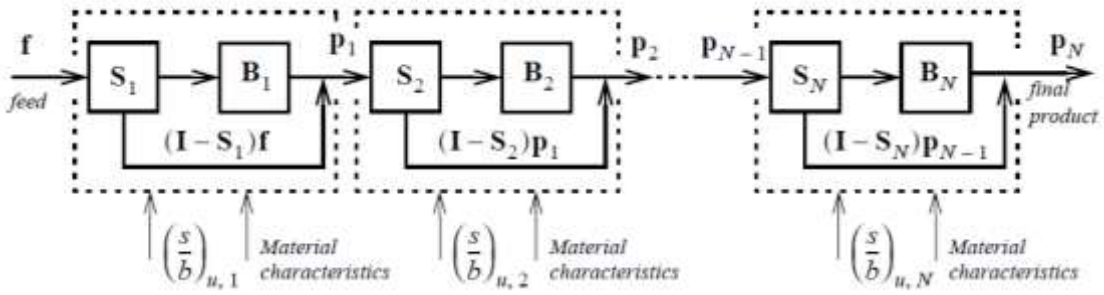

Figure 7. Process model of a cyclically operating crusher with N consecutive crushing events. The utilized compression ratio $(s/b)_u$ is determined from the location of each crushing event, crusher dynamics and rock material density. S=selection, B=breakage. (Evertsson, 2000)

Selection is equal to the probability of a particle of being crushed, while Breakage describes the way that the particle is broken, using the PSD of the product. From the IPB test the breakage behaviour is obtained.

The selection function depends on the feed size distribution width and the compression ratio. It varies in the size distribution width but not in the particle size if it is within the given size distribution. The width of the size distribution is described by a single number, being it the normalised standard deviation of the frequency function of the PSD.

The breakage function only depends on the compression ratio for a given original particle size. It is a cumulative function that describes the passing mass of particles of a given relative size.

To quantify the selection and breakage functions, IPB tests will be performed. The equipment is designed to simulate the conditions in a real crushing chamber when a certain amount of material is compressed. At regular operating conditions, at the maximum velocity that the liners move toward each other in any type of compressive crusher, the selection and breakage appearance are considered to be independent of the strain rate. The loading speed of the used hydraulic compression is 5 mm/min.

This and more information is available at EVERTSSON (1995, 1999 and 2000).

4.2. Mineralogical characterization

Often, the study for the evaluation of a mineral deposit implies only the generic study of the grades of the interesting elements of the deposit, obviating the detailed study of the mineral associations. However, a detailed study of mineralogy does not only has academic connotations as it is sometimes believed, but also it can help to increase the value of exploitation, and even only by itself can help to discard or confirm the interest of the deposit. A deep study of the mineral associations can represent a great support during the mineral processing of the ore. To know the mineral textures (particle size, morphology of the grains) is necessary to design an efficient processing circuit.

Considering the low cost of mineralogical analyses, when compared to other methods, the wrong doing in this topic by many mining companies is surprising.

During the following chapters the different analysis performed to the rock samples will be explained in detail, as well as the sample preparation process and the equipment used.

4.2.1. Chemical Analysis

The analysis of whole rocks is often very important for understanding the economic potential of the material. There exist several methods of analysis to evaluate the chemical composition of a rock sample. In this thesis, due to the elevated complexity of made the necessary analyses, the samples have been sent to a professional laboratory to obtain the chemical analyses. All samples were quartered and pulverized to a particle size <63 µm using a diminutive size ball mill in the Faculty of Geosciences of the University of Gothenburg and then they were sent to ALS Geochemistry Laboratories. The aim of this chapter is to give a brief explanation of how each different analysis performed works.

Firstly, it is necessary to specify the different groups of elements that form the whole rock sample. Generally, any sample has three types of elements: major, minor and traces (including rare earth elements). Major elements are those whose oxides represent more than 1 wt.% of a common garden variety rock in the earth's crust, on average. Minor elements are those whose oxides constitute 0.1-1 wt.% of the whole rock. Trace elements are all other elements in the periodic table, they occur in really small concentrations, of several parts per million (ppm) or parts per billion (ppb), of a common crustal rock.

The first type of analysis performed is a whole rock analysis, a 13 element package by Lithium Borate Fusion and ICP-AES; which stands for Inductively Coupled Plasma Atomic Emission Spectroscopy.

A lithium borate fusion of the sample prior to acid dissolution and ICP-MS; which stands for Inductively Coupled Plasma Mass Spectrometry, analysis provides the most quantitative analysis approach for a broad suite of trace elements. This technique solubilizes most mineral species, including those that are highly refractory. Options for adding the whole rock elements from an ICP-AES analysis from the same fusion or base metals from a separate four acid digestion are available. The minimum sample size required for this analysis is 2g. In Table 3 below, the chemical formula from said 13 oxides are shown, along with the percentage range of concentration of each oxide that the method can detect in the sample, in this case it goes from 0.01% to the entirety of it.

Table 3. Description of 13 Element Package by Lithium Borate Fusion and ICP-AES, extracted from ALS Geochemistry catalogue.

ANALYTES AND RANGES (%)								DESCRIPTION
Al_2O_3	0.01-100	Fe_2O_3	0.01-100	Na_2O	0.01-100	TiO_2	0.01-100	Fused bead, acid digestion and ICP-AES
BaO	0.01-100	K_2O	0.01-100	P_2O_5	0.01-100	LOI	0.01-100	
CaO	0.01-100	MgO	0.01-100	SiO_2	0.01-100			
Cr_2O_3	0.01-100	MnO	0.01-100	SrO	0.01-100			

The last and most important chemical analysis of the rock evaluates low grade mineralization for low level resistive elements. A single element analysis by Fusion and ICP-MS was used to identify the concentration of tungsten in the samples.

Lithium metaborate fusion followed by acid dissolution of the fused bead quantitatively digests most mineral species, including those that are highly refractory. ICP-MS techniques allow elements in these difficult-to-analyse minerals to be determined at trace levels. Additional elements are available on request. . In Table 4 the different elements for whose this method is available are displayed, together with the range of concentration of each element in ppm that the method can detect in the sample, it varies for each element.

Table 4. Description of Single Element Analysis by Fusion and ICP-MS, extracted from ALS Geochemistry catalogue.

ANALYTES & RANGES (ppm)							
Ce	0.5-1,000	Rb	0.2-1,000	Ta	0.1-1,000	W	1-1,000
La	0.5-1,000	Sn	1-1,000	Th	0.05-1,000	Y	0.5-1,000
Nb	0.2-1,000	Sr	0.1-1,000	U	0.05-1,000	Zr	2-1,000

4.2.2. X-Ray Diffraction Analysis (XRD) or diffraction of crystalline dust

Diffraction of dust is a method of structural analysis, which allows the identification of minerals by their crystalline structure. It is not a chemical analytical method, but, as we shall see, indirectly allows to estimate the composition of the analysed sample with a good approximation of the content in majority elements. The use of this analysis in this thesis will be to study the propensity of the different minerals in the processed material to be crushed and appear into

specific size fraction. Knowing the content of the main minerals in every size fraction can be used during the design of the processing circuit, during comminution and the separation.

There is a high number of documentation about the method (eg. KLUG AND ALEXANDER, 1954; BISH AND POST, 1989; CULLITY AND STOCK, 2001; MELGAREJO ET AL.,2010).

All the minerals are crystalline, this means, they dispose their chemical components (atoms, ions, molecules) on a regular manner, filling the space. Eventually, all crystals can develop polyhedral outer shapes, although much of the mineral mass does not necessarily manifest this property. The regular distribution in the space of the mineral components is described by the crystalline networks, which show the periodic repetition of the mineral cell. A cell is a unit, in the shape of a parallelepiped, which repeated identically fills the entire space of the crystal. The description of the cell provides all the information about the crystalline structure of the mineral. There are two levels of description of a unit cell:

- the parameters of the parallelepiped, three edges and three angles that we call a, b, c, α, β, γ.
- the arrangement of the atoms in the cell.

Each mineral is characterized, first, by its cell parameters. It may happen that two different minerals have almost identical cell parameters. In these cases, to distinguish them, it is necessary to take into account the second level, that is, which atoms (composition) are in the cell and how they are arranged (structure). As we will see, the crystalline powder diffraction gives information about these two levels and, therefore, allows to perfectly distinguish minerals with similar networks. Here are some notions about the phenomenon of diffraction.

The crystalline periodic networks are formed by regularly spaced reticular planes, in the same way that a two-dimensional lattice is formed by rows of regularly spaced points (MELGAREJO ET AL. 2010). A crystal lattice contains lattice planes in various orientations. Bragg's law of diffraction allows to obtain for each mineral the values of its spacing and thus to allow its identification (MELGAREJO ET AL, 2010).

Each mineral is characterized by a series spacing values. These values are known and tabulated in a database. Hence, through the values obtained in the diffraction experiment, and by consulting the database, we can identify the mineral.

It may happen that two different minerals have nearly identical cell parameters, in which case the spacing will be almost equal. In these cases, another result of diffraction must be taken into

account: the intensity in which each reticular plane reflects X-rays. The intensity depends on the second level of information, on the atoms of the cell, and their distribution.

In summary, the reticular spacings of the minerals depend on the parameters of the lattice, while the intensity of the X-rays reflected by the lattice planes depends on the structure. The identification of minerals by diffraction uses, in the first instance, the values of the spacings and, secondarily, the reflected intensities. The crystalline powder method makes it possible to obtain a list of spacings and intensities in the quickest and easiest way.

The sample of mineral or rock to be identified was properly quartered and pulverized using a diminutive size ball mill in the Faculty of Geosciences of the University of Gothenburg. In general, some mm^3 is sufficient. The sample is grinded to ultrafine powder (less than 63 μm) to produce a very large number of small crystallites, for example 10^9. Each crystallite can reflect X-rays if it is in the proper orientation with respect to the X-ray beam. The high number of crystallites in the sample guarantees that all reticular planes will have the opportunity to produce Bragg reflections because, for each spacing there will always be a number of crystallites in the proper orientation relative to the X-ray beam.

Typically, to perform the analysis the powder is placed in a sample holder (Figure 8), arranged to form a flat surface of 1-2 cm^2.

Figure 8. Sample holder for X-Ray Diffraction analysis of crystal dust.

The instrument for measuring the diffractogram is called powder diffractometer. It consists of an X-ray source, a sample holder mounted on a rotating goniometer and a detector. The diffraction of crystal dust was performed in the *Centres Cientifics i Tecnològic de la Universitat de Barcelona*, using a Bragg-Brentano PANalytical X'Pert Diffractometer (graphite monochromator, automatic gap, Kα-radiation of Cu at λ = 1.54061 Å, powered at 45kV-40mA, scanning range 4-100º with a 0,017º 2θ step scan and a 50s measuring time. Identification at

Rietveld semi-quantitative evaluation of phases was made on PANalytical X'Pert HighScrore software. The diffractogram is a graph that on the abscissa indicates the angle of diffraction and in the ordinates the corresponding intensity. The peaks of intensity correspond to Bragg's reflections.

Once the diffractogram is obtained, and the diffraction data extracted from the specific sample, the identification consists in finding in the database the mineral whose diffractogram corresponds to the problem. Since the powder diffraction database consists of many thousands of inputs, it is necessary to use a systematic method that leads safely to the solution of the problem.

Since 1936 there is a manual method of identification, the Hanawalt Method, very efficient (MELGAREJO ET AL., 2010). However, most laboratories use automatic identification using a software provided by the same diffraction equipment suppliers.

Whether the identification is manual or automatic, it is necessary to have a diffraction database. Although each operator can build their own database, it is easier to subscribe to the International Centre for Diffraction Data (ICDD) database.

It is evident that the problem sample may be a mixture of two, three or many minerals. In these cases, the experimental diffractogram is the overlap of the individual diffractograms of each mineral separately, called multiphase diffractogram (Figure 9). Therefore, in a complex mixture of many minerals, the diffractogram will also present a great complexity. Identification, in these cases, will require the user's good sense and experience of the method. In the multiphase diffractogram there is the possibility of quantifying the percentage of each mineral in the mixture. The most abundant mineral will produce higher diffraction intensities and the relative height of the diffraction peaks allows to obtain the quantity of each phase. In this method, minerals with less than 1% by weight can be detected.

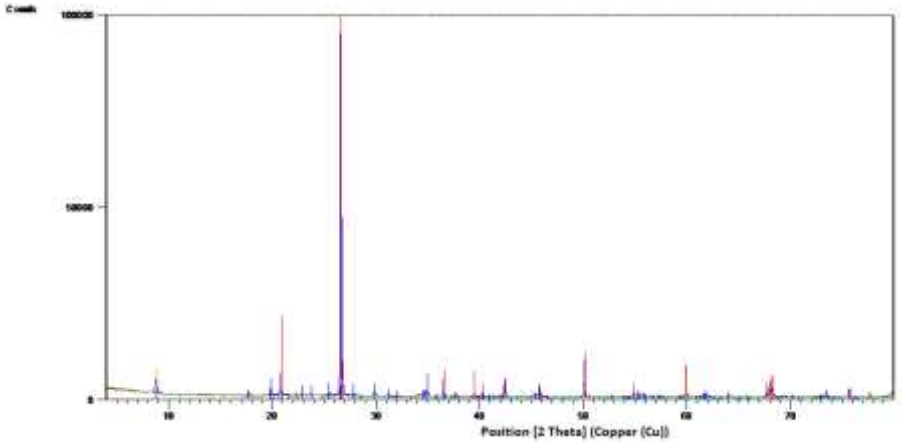

Figure 9. Multiphase diffractogram obtained from the XRD analytical method.

X-Ray Diffraction of dust has been widely used, qualitatively, to identify minerals in a mixture. However, quantitative applications have been improved in recent years from the Rietveld method (MELGAREJO ET AL., 2010).This method offers enormous possibilities for phase characterization in cryptocrystalline mixtures this includes soils, laterites, sands, batter concentrates, mine dumps or metal ores, among others.

In conclusion, we can affirm that the method of diffraction of dust is a very efficient method of identifying minerals, individual or mixed.

4.2.3. Scanning Electron Microscopy with Energy Dispersive Spectroscopy (SEM-EDS)

The scanning electron microscope (SEM) is based on obtaining an image of the sample from the scan of it with an electron beam, as a result of the interactions between the incident electrons and the sample.

The SEM consists of several basic elements: an electron gun with an electron-emitting filament, magnetic lenses that direct and focus the electron beam on the sample, scanning system, mobile and universal swivel holder, systems for obtaining the mage and the analysis.

In order to analyse a sample in the SEM, it is generally required strict vacuum conditions inside the microscope, otherwise, the electrons can be dispersed by the air molecules. In addition, the best results are obtained with conductive samples or converted into conductors by a film coating of conductive material, in this thesis the most common coating was used, graphite, although there are cases where aluminium or gold can be used too. However, currently there are electronic microscopes that do not require either sample coating or high vacuum in the chamber.

The interactions between the incident electrons and the sample originate the emission of secondary electrons, backscattered electrons, and x-rays characteristic of the elements present in the sample (MELGAREJO ET AL., 2010). In SEM, different detectors amplify the signal emitted by the surface of the sample when it is swept by a thin beam of electrons. The amplified signal strength is displayed on a conventional computer screen.

The amount of secondary electrons produced during sample bombardment varies with the beam angle of incidence on the sample but, on the other hand, the average atomic number of the elements present in the sample has very little influence. In contrast, the number of backscattered electrons increases almost linearly with the atomic number Z.

The number of incident beam electrons that are backscattered depends on the average chemical composition of the excited mineral. Thus, the higher the average of the atomic numbers of the elements that form the mineral, the greater the number of backscattered electrons. Consequently, heavy minerals emit more backscattered electrons than light electrons, so that the detectors pick up much more intensity and therefore transmit a brighter image to the screen. Hence, areas, where there are more heavy elements, appear brighter and where lighter elements exist, the image is darker. Above all, backscattered electron images will be very useful for locating heavy element minerals, since tungsten's atomic number is 74 and its standard atomic weight is 183.84, all minerals containing tungsten will be really dense and easily detectable in the displayed image (Figure 10).

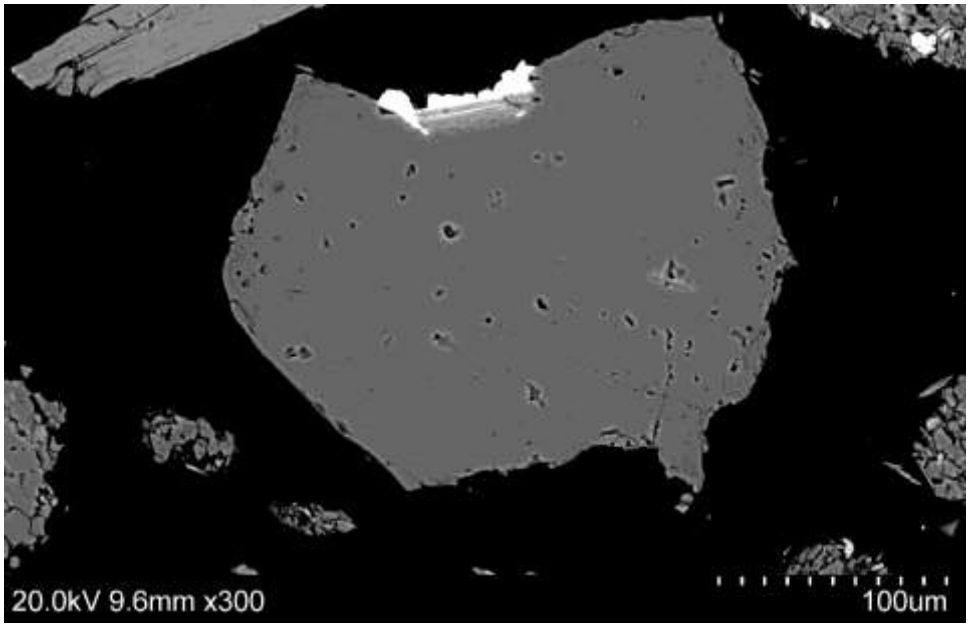

Figure 10. Grains of Ferberite tungsten ore (light) attached to a large matrix of Quartz (grey).

The interactions between the incident electrons and the sample atoms are classified as elastic, inelastic and emission of braking radiation. Elastic collisions modify the path of the incident electrons, while inelastic collisions cause a loss of energy. Secondary electrons are sample electrons that are emitted during inelastic collisions. On the contrary, the backscattered electrons are those electrons of the incident beam that are reflected by the sample after suffering multiple elastic and inelastic collisions (MELGAREJO ET AL., 2010).

On the other hand, during inelastic collisions, the incident electrons can pull electrons from the deeper layers of atoms, as long as the energy of the incident electron is higher than the ionization threshold of the atomic layer in question (MELGAREJO ET AL., 2010). When an atom has a vacancy in an inner layer, a jump of one electron from an upper layer occurs to fill that vacancy, which will leave another vacancy in the upper layer. This will be filled in turn by an electronic

jump from a top layer and so on. During each jump, the atom emits characteristic X-rays, in which the energy is characteristic of each chemical element (the energy of an X-ray equals the energy difference of the atomic levels involved). As a result of the electronic impact, the atom emits a number of characteristic x-rays.

Hence, in the continuous spectrum of X-rays, caused by the braking radiation, appears a series of peaks that correspond to the radiation characteristic of each of the elements present in the sample (Figure 11). This spectrum is generated in very few seconds and the identification of the element that generates each of the peaks is immediate so that the qualitative analysis can be performed rapidly. Unfortunately, many elements produce X-rays with energies close to those of other elements and because of the low spectral resolution of the EDS spectrometers, the analyses obtained are not always very accurate.

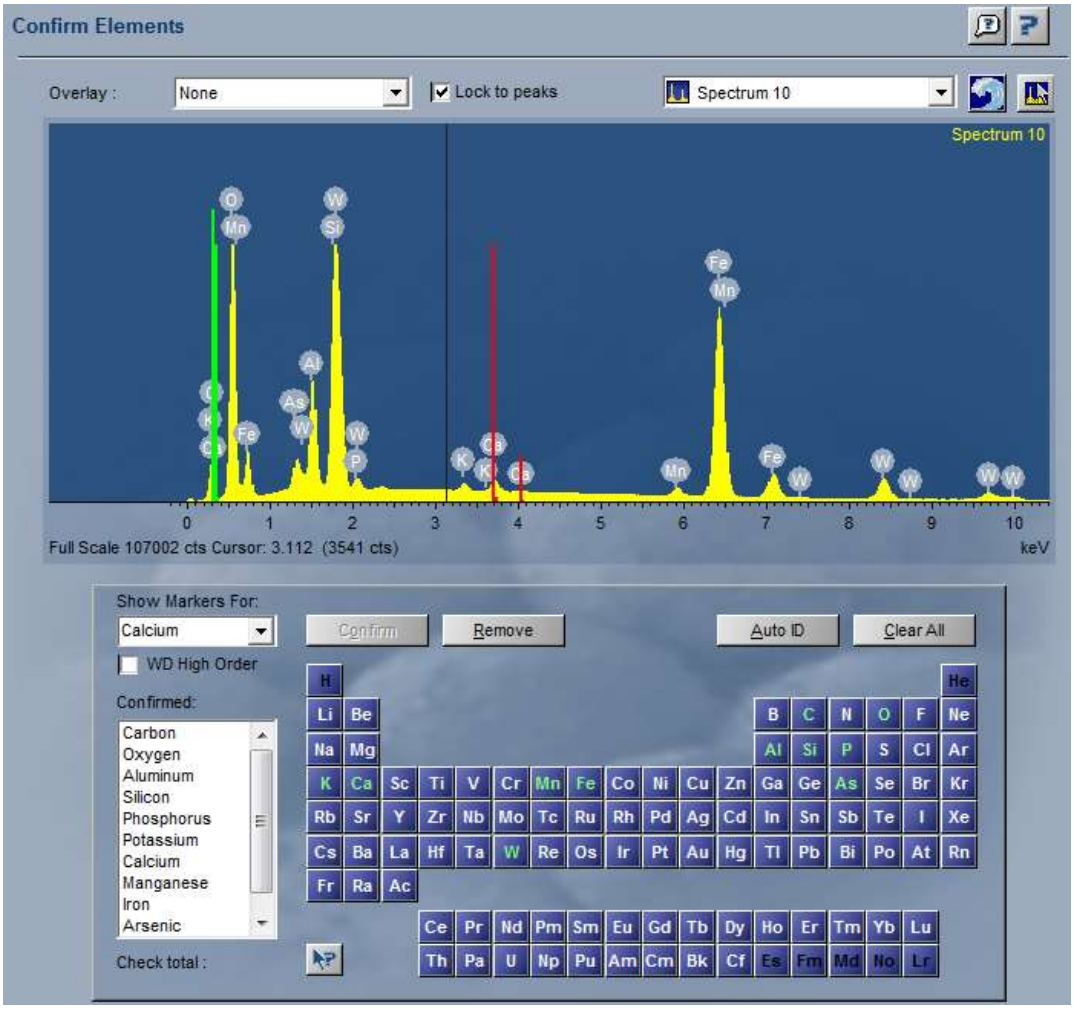

Figure 11. Spectrum for a tiny grain of Ferberite, with pollution from the surrounding minerals.

Conclusively, the intensity of the X-rays produced by each element depends on the quantity of the same in the sample, so that the energy spectrum of the X-rays emitted contains two levels of information: on the one hand, the characteristic spectrum where the position of each peak indicates the energy of a characteristic X radiation of an element; on the other hand, the intensity of each peak (represented by its height) is directly proportional to the amount of the element in the measured sample. Therefore, this method can be used to determine the chemical composition of a sample volume. Note that if the device is calibrated with suitable patterns of known composition, this qualitative analysis can be transformed into semi-quantitative.

Sample preparation

For the preparation of the sample for the SEM-EDS an entire sub-chapter will be dedicated, since it is complex and very time-consuming. Following, a step by step guide explains how the samples were prepared:

1. Prepare the epoxy resin.

A volumetric mixture should be made at the rate of 2 parts of epoxy resin per 1 of catalyst (hardener). The mixture shall be in a graduated beaker. The mixture must be removed until homogeneous and transparent. A spicy smell is normal and the mixture gets hot. It is important to carry out the mixture under the smoke hood, as the vapours it releases is irritating to the eyes and skin. A 60 ml mixture is required for the production of approximately 10 specimens.

2. Encapsulation

The base of the moulds must be removed; once separated, a Teflon layer must be sprayed to make it easier to separate them later. Next, the samples in the form of sand or gravel obtained in each particle size should be carefully placed on the mould. It is recommended to fill between a third and a half of the height of the mould with material, since when polishing we will be eroding the material and if the layer is not thick enough, we could finish it. The identification tag is then placed on one side of the capsule. Once the sample is placed, the epoxy is emptied until the sample is completely covered with it, we must ensure that there are no air bubbles, due to the high viscosity of the epoxy it must be emptied slowly. Once the samples have been covered with epoxy, the moulds should be ultrasonically passed for about 10 min, this is done to remove any small air bubbles that may have remained.

3. Drying the samples

After ultrasound, all specimens should be allowed to dry at ambient conditions for 24 hours, after this period of time, they should be placed in the freezer for one hour in order to ensure an adequate process to remove the specimens from the moulds. Once the specimens have been

removed, if it is not sufficiently hardened, the specimens should be placed in the oven at 60 ° C for a period of up to 72 hours to ensure optimal drying of the epoxy resin. The epoxy is considered to have optimum drying when it behaves as a fragile material.

4. Cutting of test pieces

When obtaining the specimens, they should be cut by the side of the base, with a laboratory saw. Once cut by the base, the polishing (~ 100 rpm) should be run through the polishing with #80 sandpaper, the polishing should be very thin (<1mm) and by hand, it is simply a matter of removing the superficial layer of epoxy to be able to begin the process of polishing with carbide of the test piece.

5. 1st step of polishing

Once the face is polished, it must pass through the different carborundum sizes (during this approximate lengths):

a. 320 → 5 min
b. 600 → 5 min.
c. 800 → 5 min.
d. 1000 → 10 min.
e. 1200 → 10 min.

The time depends on the hardness of the sample, for minerals of hardness ≤7 with 5 min for the different carborundum (glasses) is sufficient.

Before changing to the next carborundum, the specimen must be cleaned with diets, to ensure that abrasive particles from the previous phase do not reach the next. If this happens, the glass will be scratched by particles of bigger size than the one that belongs to it and would not fulfil its function well, therefore it should be changed.

6. 2nd step of polishing

Turn on the automatic polisher at a few revolutions (approx. 200 rpm). Lubricate using DP-Lubricant Blue Struers, allow constant dripping at 0.1 drops/second.

Put a drop of 3µm diamond paste and let it polish 45 minutes, over time clean the specimen with toothpaste.

Change the disc of the polisher to 1 µm, put the corresponding diamond paste and polish for another 45 minutes.

Note: When there are minerals of hardness ≥7 in the sample, it is necessary to leave the polisher to work longer, in our case some samples had more than 50% quartz, and were left 30 minutes more.

At the end of the polishing phases, it is recommended to pass the test pieces through the ultrasound to ensure the cleaning of the polished surface.

7. Carbon coat film

The samples need to be coated with a carbon film so that the surface is conductive and the SEM analysis can be performed. This will be done inside a vacuum machine to ensure that no environmental particles interfere in the spraying of the coating. The samples are placed in a sample holder inside the vacuum machine. Using the measuring tape the sample holder is moved up or downwards until it is at exactly 50 mm from the top. Carbon filament is prepared in a specific manner in the inner part of the cover, then the cover is putted in place. Start creating the vacuum and leave for 40-60 min.

Once the vacuum is created, a high intensity current conducted through the carbon filament will cause that filament is burned and the carbon covering is sprayed in all directions, including over the polished samples that, now, have a carbon coating and are ready to be analysed.

5. Presentation of Results

5.1. IPB test. Particle Size Reduction

Compressive interparticle breakage tests were performed as explained in Chapter 4.1.1. Then the obtained data was treated, so that to represent it in a comprehensive and graphical way.

When a general view on the particle size reduction of one or more compressive test is aimed, it is easier to represent PSDs using cumulative fraction. However, when it is aimed to evaluate the behaviour of the material in specific size fractions, the more practical representation is using frequency fraction.

Particle size distribution for interparticle breakage test results are shown in Figure 12 and 13.

A comparison of the cumulative passing fraction particle size distribution of all the compression tests performed is represented in Figure 6. It can be seen that the initial compression events of low compression ratio (s/b) tests (10% and 15%) generate a product with more coarse particles and fewer fines than the rest. Then it is followed by the first compression event of medium and high compression ratio (20%, 25% and 30%, 35%) and the last events of 10 and 15% s/b. Finally the last events of medium and high compression ratio are the ones that generate bigger amount of fines and lesser coarse particles as product. This behaviour will be explained more in detail in posterior graphs.

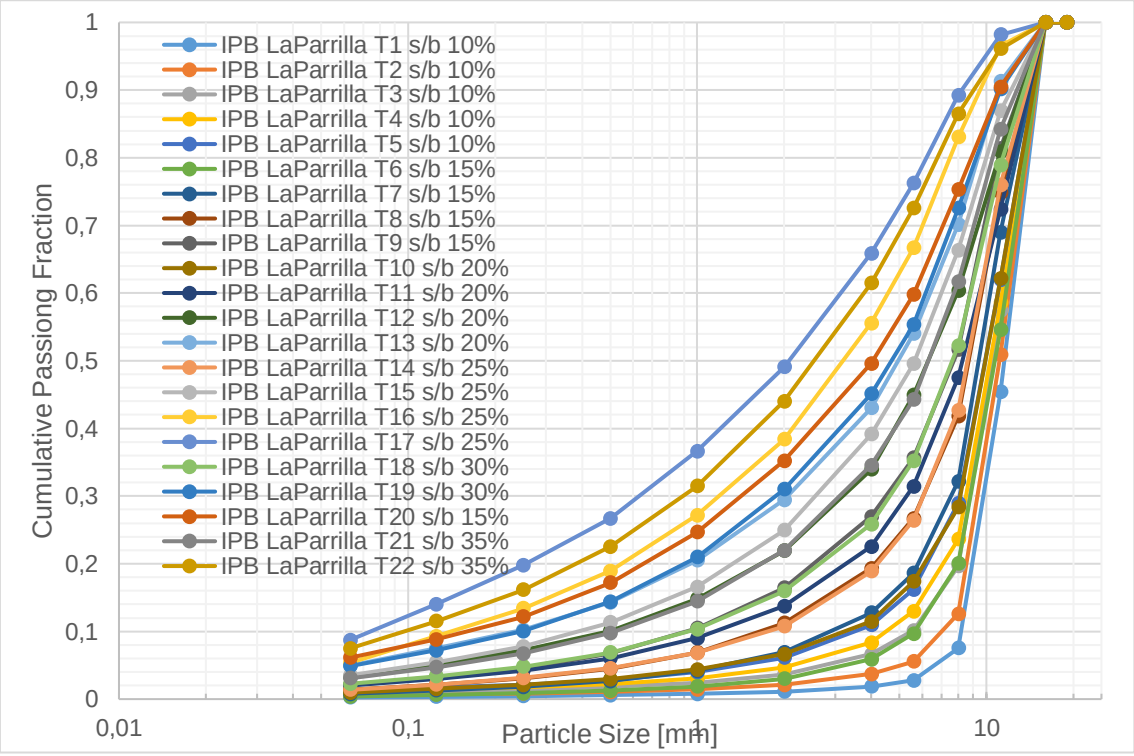

Figure 12. Cumulative PSD of the product of each compression test.

In Figure 13 the same data than in Figure 12 is represented, this time using the frequency fraction. The behaviour explained above is reinforced by Figure 13, although this is not the most notorious aspect of this graph. By studying the frequency diagrams it can be noted that there are three particle size ranges accumulations: firstly an accumulation of particles in the size range 1-2 mm and 2-4 mm, then an accumulation of particles in the range <0.063 mm, and lastly the usual accumulation of coarse particles that have merely been broken, in the size range 5.6-11.2.

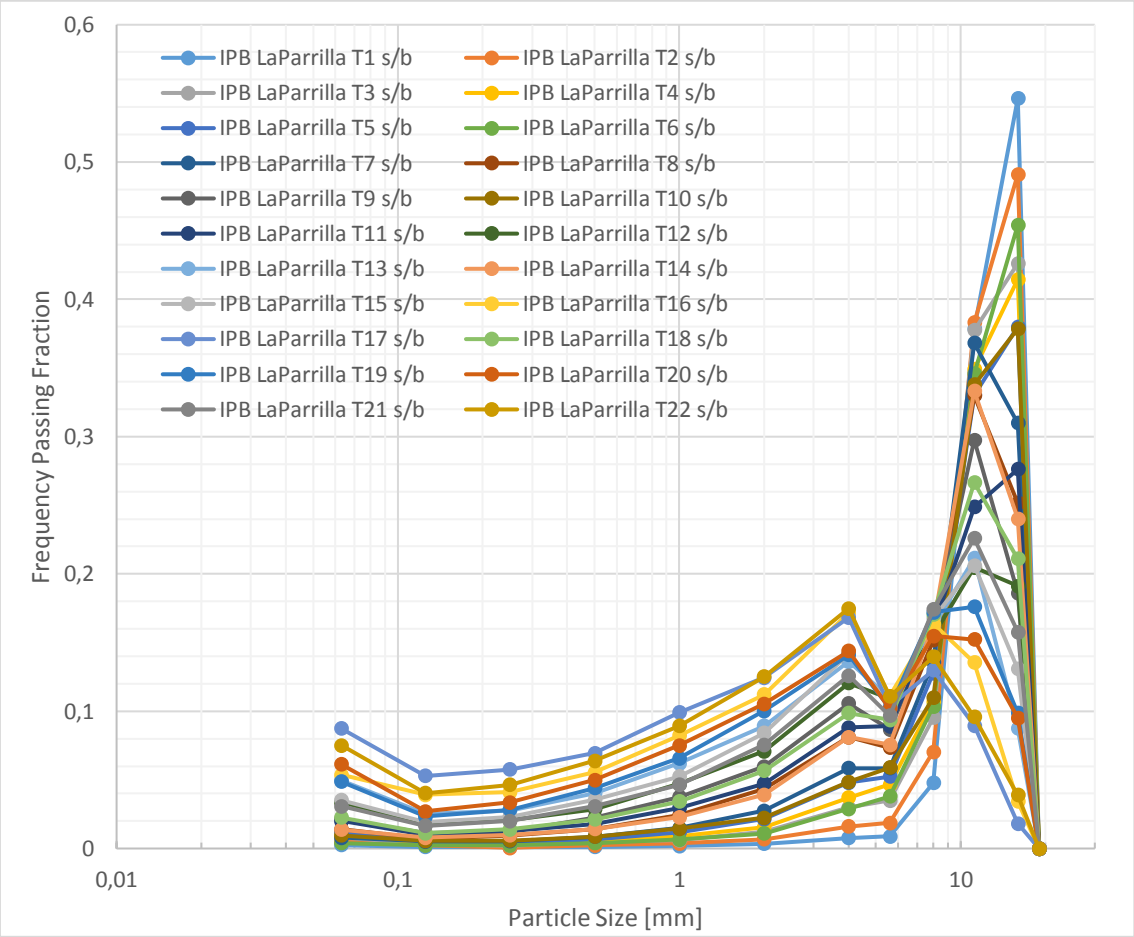

Figure 13. Frequency PSD of the product of each compression test.

Figures 14 and 15 represent the frequency and cumulative PSD of only the first compression of each different compression ratio. They perfectly reflect the dependence of the compression ratio and the particle size distribution. Due to the fact that all of the tests plotted in these graphs have the same feed the difference in the product's PSD clearly expresses that for higher compression ratio the particle size reduction will be higher.

The PSD of the product of the last compression event for each compression ratio is shown in Figures 16 and 17. These graphs show the final product of every compression ratio, making possible to see which one achieves a higher particle size reduction, the compression tests order from lower to higher particle size reduction is 10, 15, 20, 30 (note that in the legend of the graphs

there is written 15% for T20 because the last compression event of 30% was carried out only to 15% of s/b), 35 and 25. Also, in Figure 16 the three particle size range accumulations explained above are reflected. These two graphs represent the final product of the compressive crushing tests, the product and PSD represented here have been used for analysing the chemical and mineralogical composition in the other stages of the thesis, specifically the compression ratios of 10, 20 and 30%, which are shown in Figure 18.

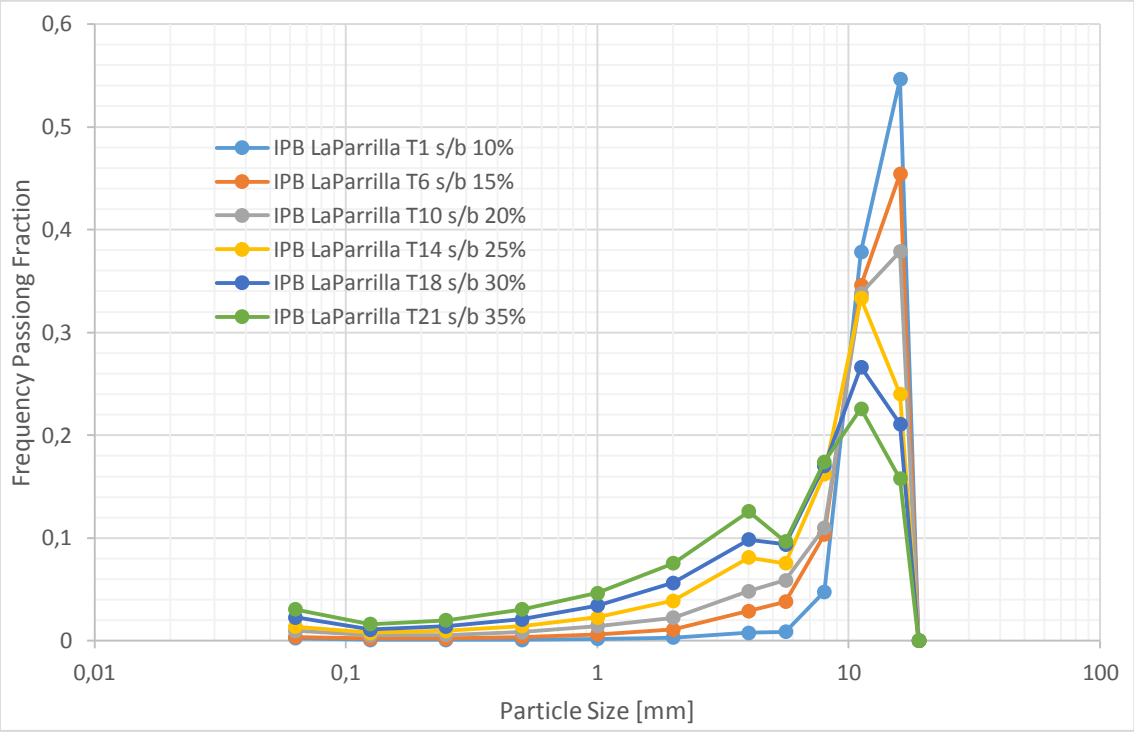

Figure 14. Frequency PSD of the product of the first compression in each series of s/b.

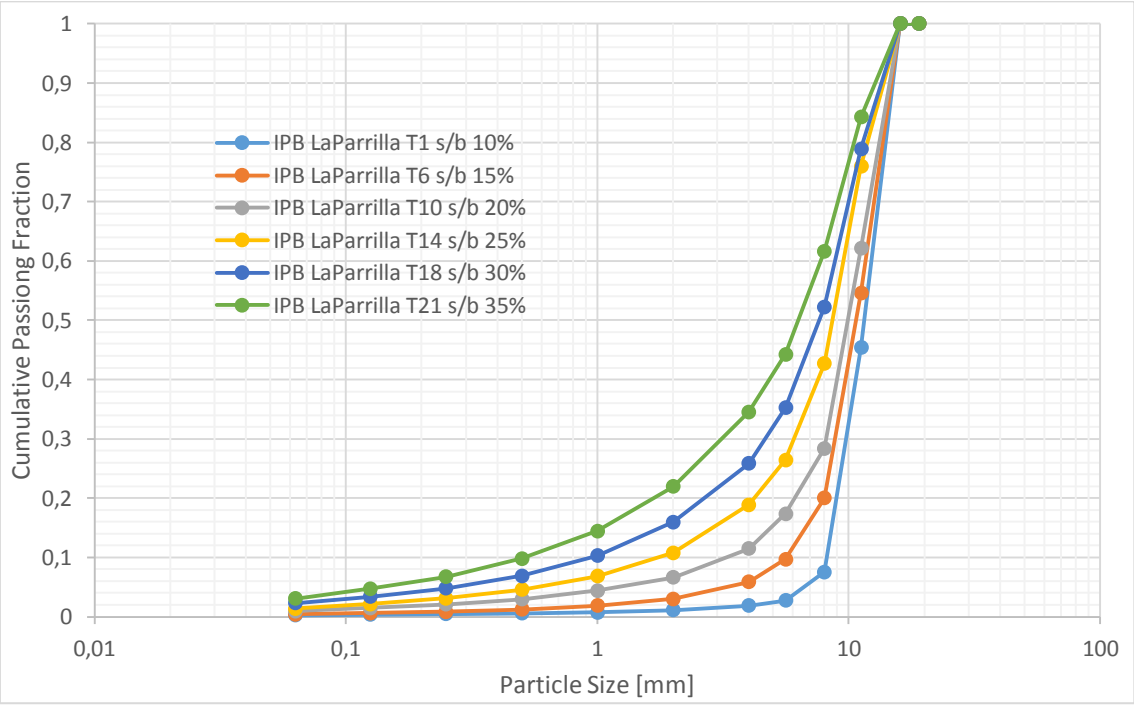

Figure 15. Cumulative PSD of the product of the first compression in each series of s/b.

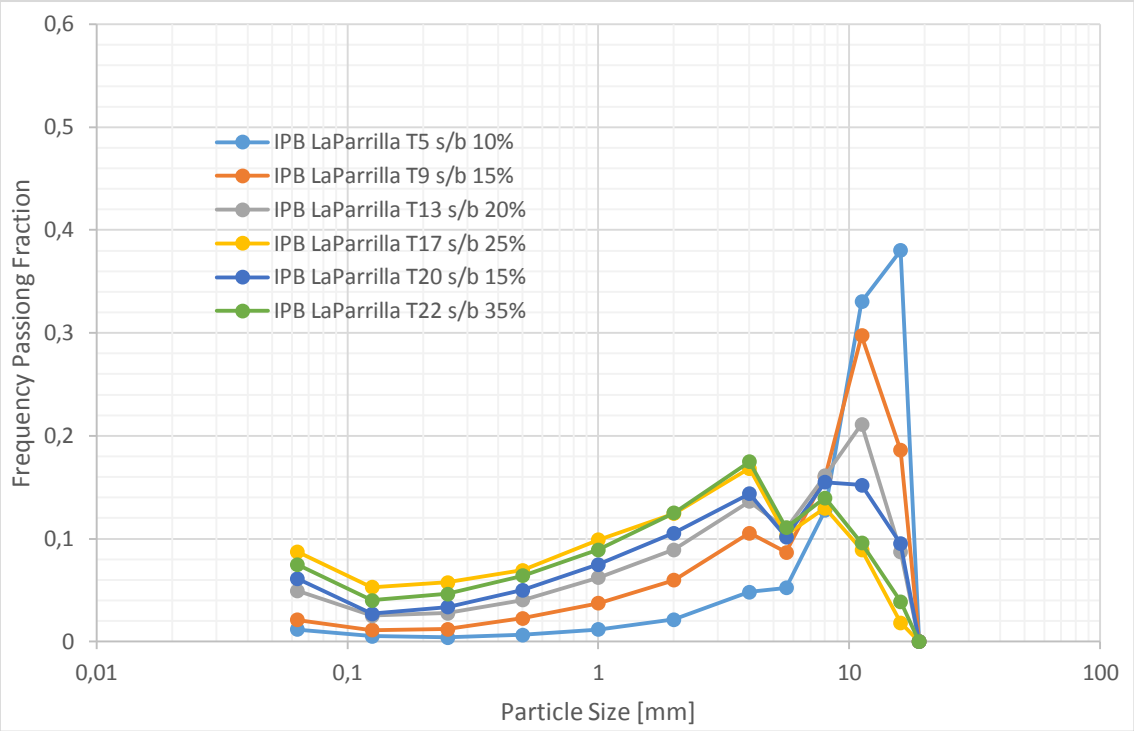

Figure 16. Frequency PSD of the product of the last compression in each series of s/b.

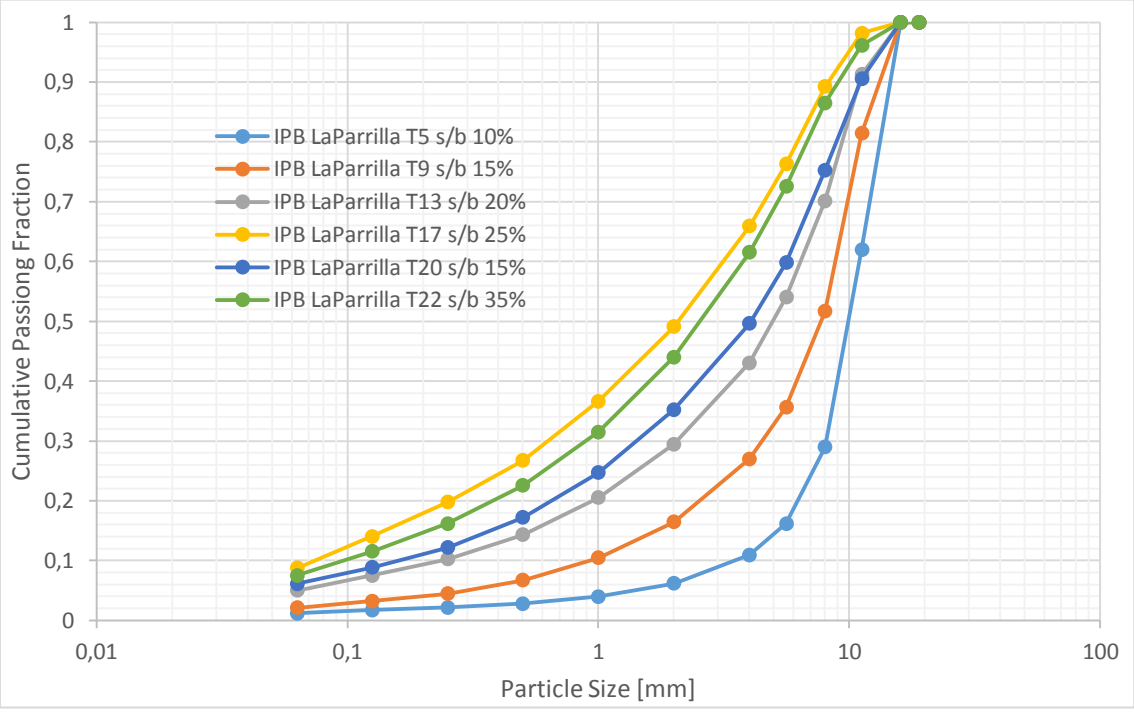

Figure 17. Cumulative PSD of the product of the last compression in each series of s/b.

In Figure 18 a comparison between compression ratios 10, 20 and 30% is plotted. The resulting size distributions from all the interparticle breakage tests with compression ratios ranging from 10 to 35% are shown for each series individually in Appendix A.

Here a correlation between compression ratio and particle size reduction can be observed, so that, the higher the compression ratio is, the bigger the particle size reduction that will be

acomplished. From a smaller s/b a product containing a bigger fraction of coarse particles (a peak in the size range 5.6-16 mm occurs) and fewer fines will be obtined. In the other hand, when the s/b is larger, the peak in coarse particles mentioned previously is blurred, while an accumulation of particles in the range of 1-4 mm is being marked, and a bigger amount of fines are generated, making a more homogeneous frequency distribution. A logic, although worth mentioning, fact that is represented in these graphs is that for more compression events, a larger particle size reduction is achieved.

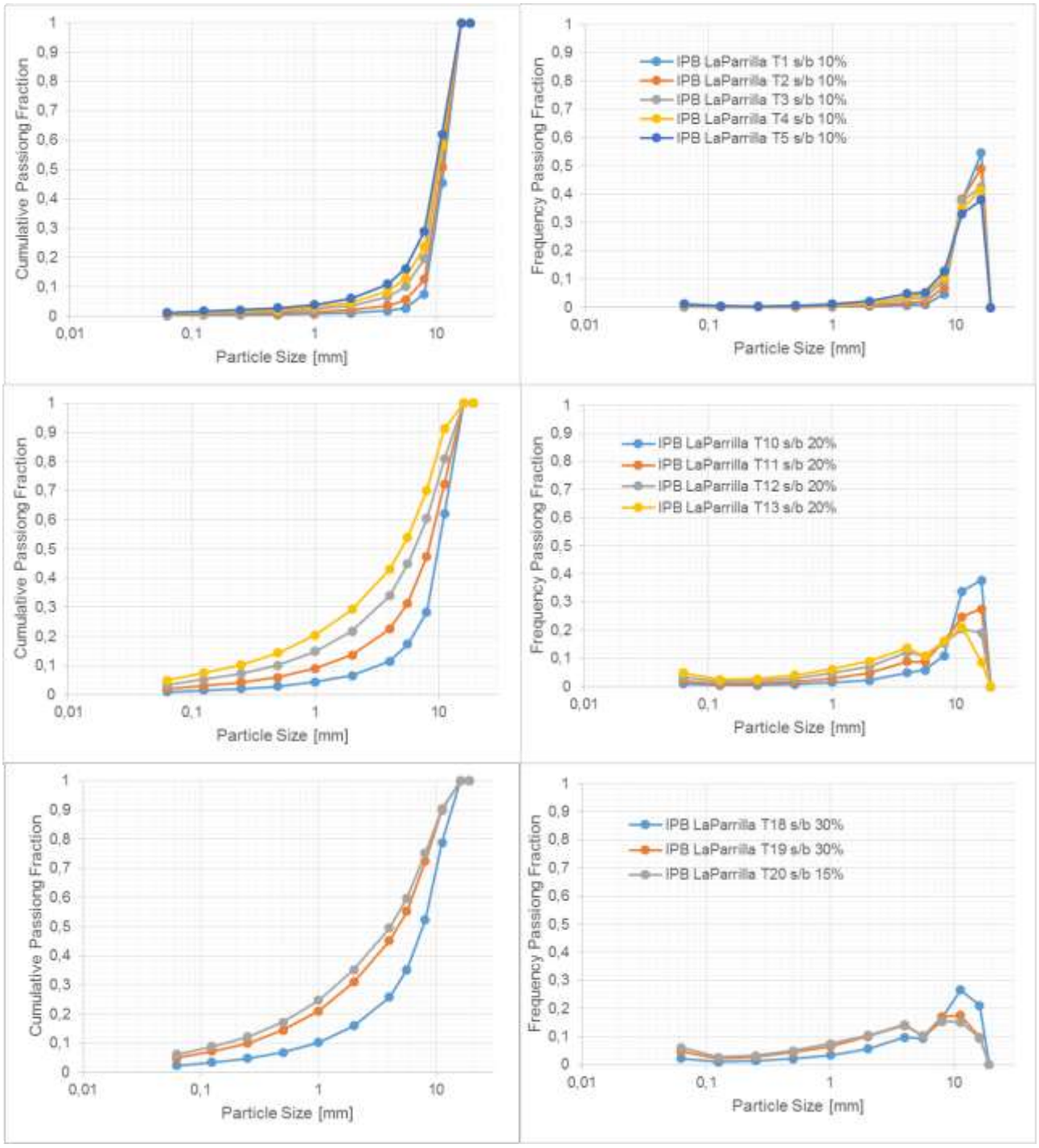

Figure 18. Cumulative and frequency comparative between compression ratio 10, 20 and 30%.

In Figure 19, an example of a force-displacement plot for the 15% IPB compression test can be seen. The force-displacement plots for all compressive crushing tests performed is found in Appendix B. Figure 19 shows how the force level increases for each consecutive compression event as the material is being reduced in size and getting finer.

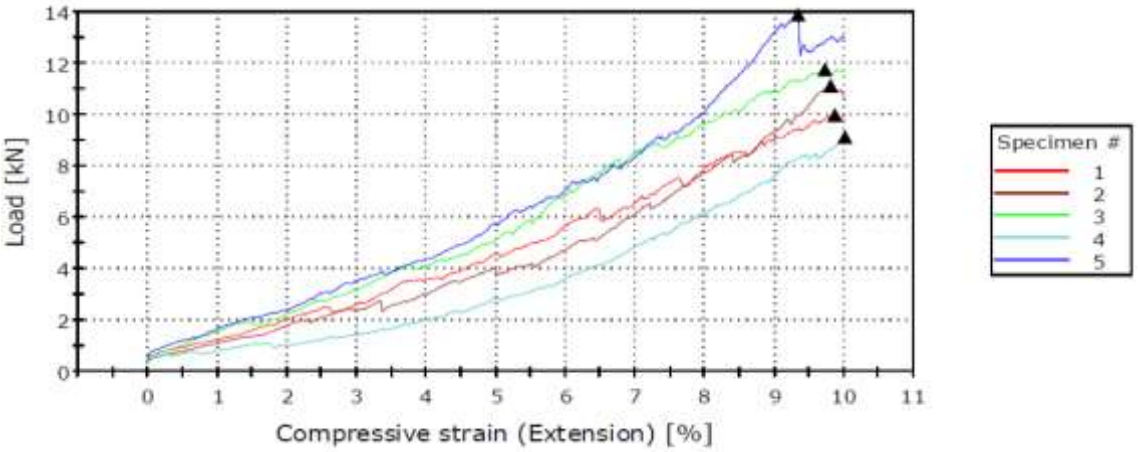

Figure 19. Force-displacement plot for the 5 compression tests of the 10% compression ratio IPB.

5.2. Bond Work Index

The Instron 400RD hydraulic compression used for the crushing tests, after each test series gives as an output a variety of files containing all the data from the measurements of piston displacement, applied force and applied compression ratio that have been continuously logged during the tests. From this data the area under the curve of load applied against compressive stain is automatically calculated, this value is the total energy used for each compression event. In Figure 19 the force-displacement plot for the 15% IPB compression test can be seen.

With the data obtained from the hydraulic compression the energy used for each compression event is known. The particle size distributions of the product after each compression event is also known, as well as the PSD of the initial feed. Bond Work Index (W_i) for the studied material will be tried to calculate from this data and using Bond's equation for energy consumption for comminution processes (4).

As a reminder, Bond Work Index represents the resistance of a given material to size reduction, and is defined as the amount of energy required, in kWh, to reduce a metric ton of material from a theoretical infinite size in the feed to a product size where 80% passes the 100 µm mesh size.

So that to be able to calculate the Bond Work Index of the material, three different parameters need to be calculated or measured. The first value is Bond's Energy (E), for which, as we said, the Instron 400RD calculates the value.

Then the p_{80}, meaning the mesh size where 80% of the product mass passes through, must be measured for each size reduction due to the fact that each compression experiment gives a different resulting particle size distribution.

At last the f_{80}, meaning the mesh size where 80% of the mass from the feed passes through, will be extracted from the particle size distribution of the feed. Some values measured in the p_{80} section will be used for the f_{80} parameter.

The calculation will be carried out for each compression ratio, and then the results will be analysed, so that one different value of W_i will be obtained for each compression event.

Bond Energy (E)

No calculous was made to obtain the energy used in the compressions, they were extracted from the output files from the hydraulic compression machine, and are shown in Table 5. The energy values are extremely variable, and go from less than 20 J to nearly 2000 J, depending on the compression ratio and the number of event in every series.

Table 5. Energy used in each compression event.

10% of s/b		15% of s/b		20% of s/b		25% of s/b		30% of s/b		35% of s/b	
Test nº	***E* (J)**	**Test nº**	***E* (J)**	**Test nº**	***E* (J)**	**Test nº**	***E* (J)**	**Test nº**	***E* (J)**	**Test nº**	***E* (J)**
T1	24,7	T6	71,6	T10	146,6	T14	271,4	T18	448,7	T21	732,5
T2	22,0	T7	63,1	T11	130,7	T15	363,2	T19	413,4	T22	1957,2
T3	27,1	T8	74,1	T12	167,2	T16	478,7	T20	62,3		
T4	17,2	T9	95,1	T13	189,2	T17	418,9				
T5	25,4										

The first parameter to Bond's equation (4) is now known.

Parameter p_{80}

For the posterior calculation of Bond's Work Index for particle size reduction, the value p_{80} of every compression test needs to be measured. Figure 20 represents the cumulative PSD of the product obtained after each compression test, it is basically the same graph as Figure 12 but, represented in a linear scale instead of logarithmic.

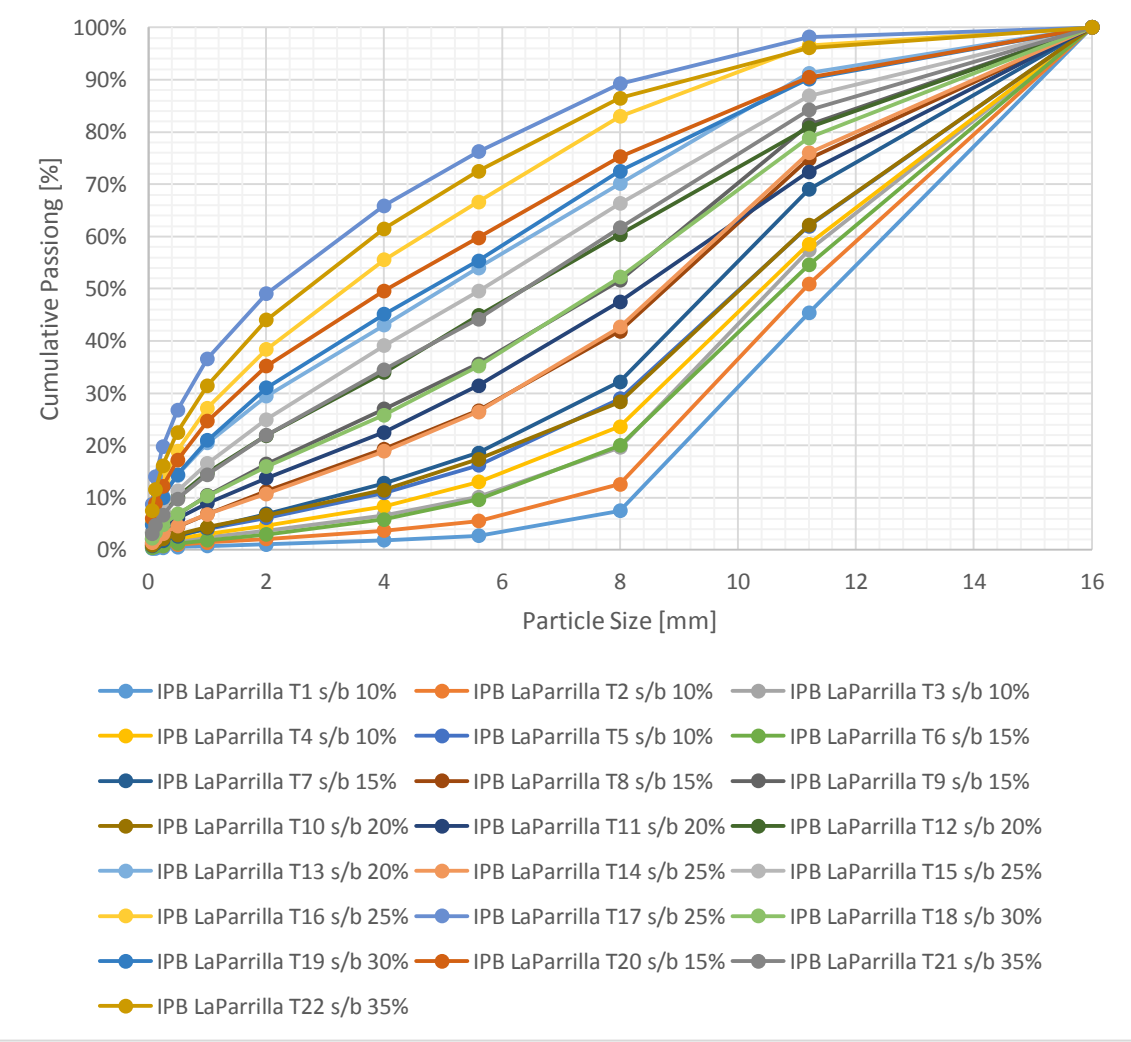

Figure 20. Cumulative PSD of the product of each compression test.

From Figure 20, using the excel file and a substantial amount of zoom, all values of p_{80} can be measured with enough accuracy. They are shown below, in Table 6.

Table 6. Values of p_{80} for each compression test.

Test nº	p_{80} [mm]	Test nº	p_{80} [mm]
T1	**14,24**	T12	**11,08**
T2	**14,04**	T13	**9,50**
T3	**13,74**	T14	**12,00**
T4	**13,68**	T15	**10,12**
T5	**13,48**	T16	**7,56**
T6	**13,88**	T17	**6,29**
T7	**12,90**	T18	**11,44**
T8	**12,18**	T19	**9,35**
T9	**11,05**	T20	**9,00**
T10	**13,46**	T21	**10,60**
T11	**12,52**	T22	**6,88**

The different values for the second parameter of Bond's equation (3) are calculated

Parameter f_{80}

According to Table 2 where the test plan for IPB is detailed, tests number 1, 6, 10, 14, 18 and 21 use material in the range 8-16 mm as feed (as explained in Chapter 4.1.1.). For the remaining tests the feed material used is the product of the previous compression test, so that test nº 2 would use test nº 1's product as feed, or in the same way test nº 17 would use as feed test nº 16's product.

The uncompressed feed material had a size in the range 8-16 mm. Due to the lack of meshes in between these values (the only mesh in this range is 11.2 mm), after contemplating possible solutions to obtain the most representative value for the f_{80}, the conclusion that doing an interpolation from the initial PSD from the received material was the most practical solution was reached.

Firstly, after receiving the material from La Parrilla mine site, a sieve analysis of a representative sample (previously quartered) was realized in order to know the PSD of the said material. The result is represented bellow in a plot where the particle size is on the abscises axis in a logarithmic scale and the cumulative weight fraction in the ordinates (Figure 21).

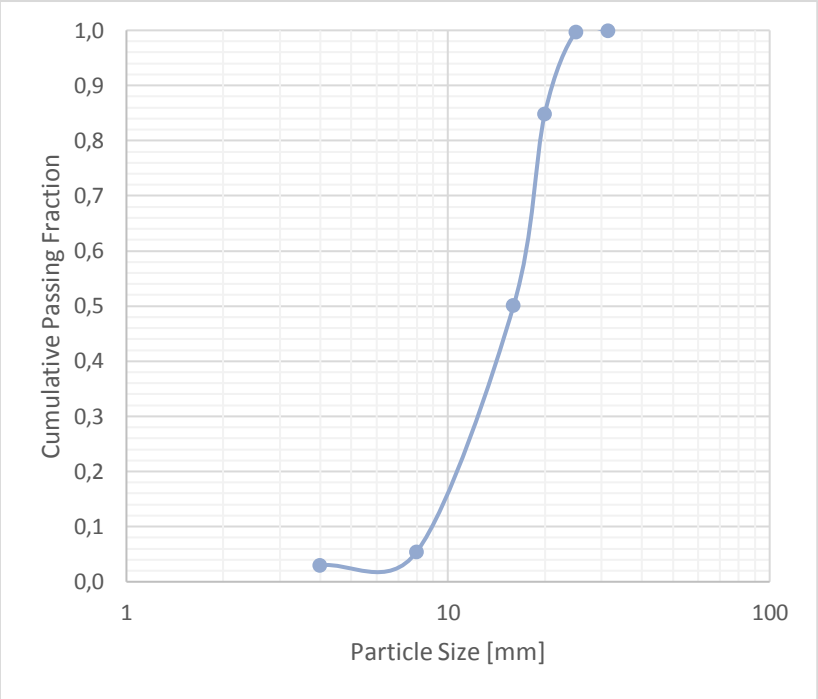

Figure 21. Feed Particle Size Distribution of the received material.

An interpolation was figured: in the range of particle size from 8 to 16 mm, what would be the mesh size that 80% of the mass would go through? The calculated solution results that f_{80} = **14.41mm**, for tests number 1, 6, 10, 14, 18 and 21.

According to the results measured for p_{80} in the previous section, f_{80} for the remaining tests can be easily deduced. In Table 7*Table 7* all values for the f_{80} parameter are shown.

Table 7. Values of f80 for each compression test

Test nº	f_{80} [mm]	Test nº	f_{80} [mm]
T1	**14,41**	T12	**12,52**
T2	**14,24**	T13	**11,08**
T3	**14,04**	T14	**14,41**
T4	**13,74**	T15	**12,00**
T5	**13,68**	T16	**10,12**
T6	**14,41**	T17	**7,56**
T7	**13,88**	T18	**14,41**
T8	**12,90**	T19	**11,44**
T9	**12,18**	T20	**9,35**
T10	**14,41**	T21	**14,41**
T11	**13,46**	T22	**10,60**

The third and last parameters to Bond's equation (4) are calculated.

Bond Work Index

First, to remember it, Bond's equation for energy consumption during particle size reduction is shown in equation (4) (BOND, 1952):

$$E = Wi \cdot \left(\frac{10}{\sqrt{p_{80}}} - \frac{10}{\sqrt{f_{80}}} \right) \quad (4)$$

In the equation E and W_i are in kWh/t, while f_{80} and p_{80} are in µm. E will have to be transformed from J to kWh/t taking into account the mass used in every compression test, which was 500 g of rock material. Once this is done and the representative values for the feed and the product are in microns, Bond Work Index can be easily calculated, as it is shown in Table 8.

Table 8. Calculation of Bond Work Index for every compressive crushing event.

Test nº	f_{80} (um)	p_{80} (um)	E (J)	E (kWh/t)	W_i (kWh/t)
T1	14374,6	14240	24,7	0,0137	**34,9**
T2	14240,0	14040	22,0	0,0122	**20,5**
T3	14040,0	13740	27,1	0,0151	**16,5**
T4	13740,0	13680	17,2	0,0095	**51,0**
T5	13680,0	13480	25,4	0,0141	**22,3**
T6	14374,6	13880	71,6	0,0398	**27,0**
T7	13880,0	12900	63,1	0,0350	**11,1**
T8	12900,0	12180	74,1	0,0412	**16,1**
T9	12180,0	11050	95,1	0,0529	**11,7**
T10	14374,6	13460	146,6	0,0815	**29,2**
T11	13460,0	12520	130,7	0,0726	**22,9**
T12	12520,0	11080	167,2	0,0929	**16,5**
T13	11080,0	9500	189,2	0,1051	**13,8**
T14	14374,6	12000	271,4	0,1508	**19,1**
T15	12000,0	10120	363,2	0,2018	**24,9**
T16	10120,0	7560	478,7	0,2660	**17,0**
T17	7560,0	6290	418,9	0,2327	**21,0**
T18	14374,6	11440	448,7	0,2493	**24,7**
T19	11440,0	9350	413,4	0,2297	**23,1**
T20	9350,0	9000	62,3	0,0346	**17,4**
T21	14374,6	10600	732,5	0,4069	**29,7**
T22	10600,0	6880	1957,2	1,0873	**46,4**

5.3. Size Reduction Modelling

The Selection function is obtained from the IPB compression tests. The value of S for the first test in each compression series, which have a pre-established size distribution (+8 -16 mm, defined as $+x_1 - x_0$), is the mass fraction that pass the sieve size of x_1 = 8 mm. For the following compression events the value of S if calculated by equation (6) (EVERTSSON, 1999):

$$S_i = \frac{W_i^{x_1} - W_{i-1}^{x_1}}{1 - W_{i-1}^{x_1}} \tag{6}$$

Where $W_i^{x_1}$ is the passing mass fraction the sieve size x_1 after test number *i* and S_{i-1} is the value of the selection function from the previous compression event. The probability of breakage increases with increasing the compression ratio and with short fractions of feed size distribution.

A selection function of two variables developed by Evertsson (1999), shown in equation (7), describes the breakage probability of a particle.

$$S(S_{s/b}, \sigma_{s/b}) = a_1 \ {s_{s/b}}^2 \ {\sigma_{s/b}}^2 + a_2 \ {s_{s/b}}^2 \ \sigma_{s/b} + a_3 \ {s_{s/b}}^2 + a_4 \ s_{s/b} \ {\sigma_{s/b}}^2 + a_5 \ s_{s/b} \ \sigma_{s/b} + a_6 \ s_{s/b} + a_7 \ {\sigma_{s/b}}^2 + a_8 \ \sigma_{s/b} + a_9 \tag{7}$$

To calibrate the breakage function only the results from the first test of each compression ratio are needed, because the breakage behaviour is only dependent of the compression ratio. This data can be obtained from Figure 14. Equation (8) mathematically describes the breakage function, the outcome of this function is the cumulative particle size distribution of the product.

$$B\left(x_{S/b}, S_{s/b}\right) = \left(1 - \left(\alpha_3 + \alpha_4\left(s_{s/b}\right)\right)\right) x_{s/b}^{\alpha_1 + \alpha_2\left(S_{s/b}\right)} + \left(\alpha_3 + \alpha_4\left(s_{s/b}\right)\right) x_{s/b} \tag{8}$$

$S_{s/b}$ is the compression ratio. $X_{s/b}$ is a vector of particle sizes relative to the initial particle size value (x_o) and is defined by equation (9). Finally, the values of the four constants α_i can be fitted to the experimental data obtained.

$$x = \frac{log_2(\frac{x}{x_{min}})}{log_2(\frac{x_0}{x_{min}})} \tag{9}$$

After fitting the breakage function (equation XXX) to the data obtained from the interparticle breakage tests the calculated numerical values of the constants are:

α_1 = 34.416277 α_2 = -77.159956 α_3 = -0.090126 α_4 = 0.927232

At last, both obtained functions: selection and breakage, are applied to each compression test in order to simulate the particle size reduction of the characterized material using the calculated functions, and to compare it with the test results (seen in Figure 22).The theory and formulations above has been extracted from EVERTSSON (1999, 2000).

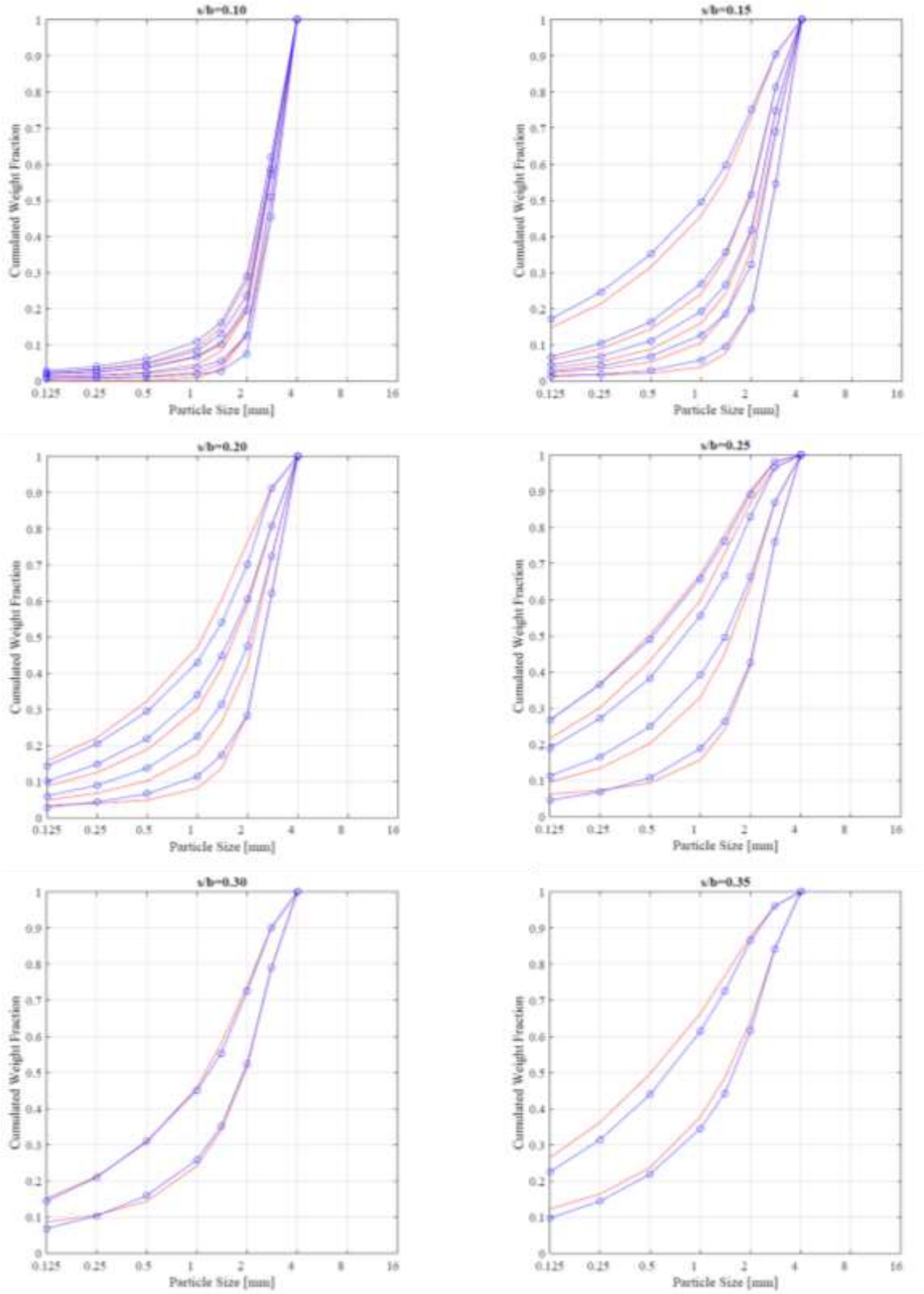

Figure 22. Real (in blue) and simulated (in red) particle size distribution results of the IPB compressive crushing tests.

5.4. Chemical composition

The compressive crushing experimental work on particle size reduction, energy consumption and modelling calibration is all presented before this chapter. From now on, the results of the characterisation of the studied material will be presented.

The aim of this chapter is first, give information on the chemical composition of the material used in the experimental work and second, to analyse the concentration of tungsten in different particle size fractions.

A sample of rock previously quartered and ground to fine particle size (<0.063 mm) was sent to ALS Geochemistry Laboratories to perform a quantitative analysis of 13 elements (mayor and minor) done by Lithium Borate Fusion and ICP-OES. The output of this analysis is the concentration of every oxides shown in Table 3.

So that the whole has the following chemical composition (Table 9):

Table 9. Composition of the whole rock used in the experimental work, expressed in wt. %

	SiO_2	Al_2O_3	Fe_2O_3	CaO	MgO	Na_2O	K_2O	Cr_2O_3	TiO_2	MnO	P_2O_5	SrO	BaO
Total	73,6	15,00	4,1	0,04	1,58	0,23	4,08	0,02	0,62	0,03	0,1	<0.01	0,05

SiO_2 is the most abundant component, also there is an important amount of Al_2O_3 followed by K_2O. This is because the main minerals are quartz and micas. The remaining oxides' concentrations do not attract attention in comparison with an average earth's crust rock.

As is explained above, the next step is related to the composition of tungsten. In order to know the concentration of tungsten for each different size fraction, samples of the compressed material, previously quartered and ground to the same size as before, were sent to ALS Geochemistry Laboratories. ME-MS analysis for every size fraction at 20% compression ratio, as well as the whole rock, were performed (Table 10).

Table 10. Tungsten concentration in ppm in each size fraction and the whole rock.

Sample	s/b	Passing sieve size [mm]	W [ppm]
LP-12	20%	16,000	**113**
LP-13	20%	11,200	**146**
LP-14	20%	8,000	**164**
LP-15	20%	5,600	**138**
LP-16	20%	4,000	**116**
LP-17	20%	2,000	**153**
LP-18	20%	1,000	**185**

LP-19	20%	0,500	**196**
LP-20	20%	0,250	**185**
LP-21	20%	0,125	**213**
LP-22	20%	0,063	**277**
LP-34	Whole rock		**253**

By performing chemical analysis of tungsten concentration we aim to find any existing correlation between particle size and amount of tungsten. For this purpose the results show above are graphically represented in Figure 23.

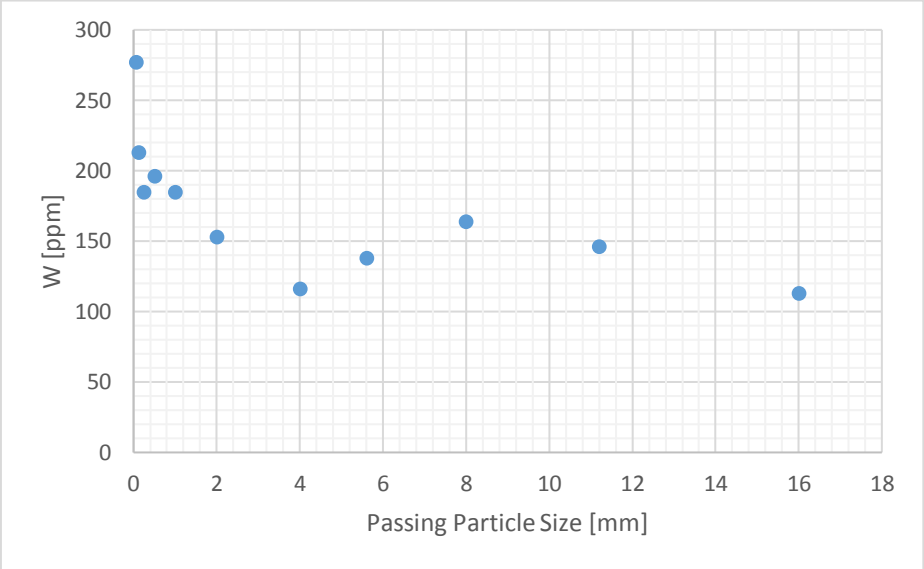

Figure 23. Tungsten concentration in ppm in each size fraction of 20% of s/b.

At a glance there is a slight correlation between particle size and tungsten concentration. It seems like an inversely proportional relation, meaning that the smaller is the particle size the higher the concentration of tungsten existing in the sample.

GULDRIS (2016) performed a compressive crushing study following the IPB test procedure, developed by EVERTSSON (2000), using two tungsten ores and one tantalum ore and later analysed the content of a said elements for the different compression ratios. No difference in the metal content was generated by the different compression ratios. Due to this results and the elevated price of the quantitative analysis, in the present research it was not thought to be necessary to carry out the analyses for more than one different compression ratio, 20% was the chosen series to analyse. Unfortunately, the analysis results do not give any direct information on the mineral that contains the tungsten. These quantitative analytical methods only give information about the content of specific elements, and not about the mineralogy of the sample. For this reason we will proceed to the next chapter.

5.5. Mineralogical composition

In this chapter the mineralogical composition will be investigated. The material used for the mineralogical characterization is the product obtained from the compressive crushing tests. Two different analytical methods have been used for this purpose: X-Ray Diffraction of crystalline dust (XRD) and Scanning Electron Microscopy with Energy Dispersive Spectroscopy (SEM-EDS).

In order to see the minerals that form the sample rock and the proportions of each one the highly accurate semi-quantitative method of diffraction is used. There is no need to know all the minerals in the material; only those in quantities large enough that can affect the breakage behaviour and the mineral liberation, those who accompany the metal ore and, in case of its existence, any mineral that can be interesting for economic use. In the studied case the material comes from a mine site that is not currently being exploited, but in the past it was exploited for a long period of time, therefore it is highly unlikely that any unknown mineral that could be economically exploited is found. To evaluate which minerals are in contact with the tungsten ore and how they are distributed an image analysis method is used, a SEM-EDS.

In Table 11 the different samples that have been mineralogically characterised are identified, using its particle size and the compression ratio to which they have been exposed in the compressive crushing tests. In green the samples that have been subjected to the XRD analysis as well as to the SEM and in blue those who have only been subjected to the XRD. Also mention that a sample of the whole rock has been evaluated using the XRD.

Table 11. Samples subjected to mineralogical characterization methods.

Retaining size fraction [mm]	Compression ratio, s/b		
	10%	20%	30%
11,2	LP-01	LP-12	LP-23
8	LP-02	LP-13	LP-24
5,6	LP-03	LP-14	LP-25
4	LP-04	LP-15	LP-26
2	LP-05	LP-16	LP-27
1	LP-06	LP-17	LP-28
0,5	LP-07	LP-18	LP-29
0,25	LP-08	LP-19	LP-30
0,125	LP-09	LP-20	LP-31
0,063	LP-10	LP-21	LP-32

0	LP-11	LP-22	LP-33

Coarse particle size has not been assessed using the SEM because the polished section that is used in it has a diameter of 24mm, therefore the amount of particles that fit in it is too low to be representative. The smallest particle size has not been assessed either because when polishing it, due to the small size of its grains they were being stripped off instead of being polished.

Samples subjected at different compression ratios have the same ratio in their mineralogical associations. However, for larger compression ratios there is a higher degree of liberation achieved, although the mineral associations for the not liberated particles will remain equal regardless of the compression ratio. Therefore, due to the large amount of time needed to prepare and evaluate a sample and due to the high price of a SEM-EDS session, only the 20% of compression ratio was chosen to be analysed in the SEM. To ensure the fact that mineral associations are not affected by compression ratio, two samples were evaluated from the 10 and 30% compression ratio.

Not all the samples were assessed, instead, following the same procedure than for the SEM, three samples were evaluated to see if there are changes in the mineralogy depending on the compression ratio.

In Table 12 the mineralogical composition of the material is shown. There is a dominance of two main minerals in all the samples assessed, they are: quartz and muscovite. Quartz is the mineral with a larger fraction in each and every sample, then there is muscovite that in all the samples is the second largest mineral fraction. Quartz's fraction goes from 70% in the particle size of 11.2-16 mm of 30% of s/b to 48% in the size fraction of 0-0.063 mm of 20% compression ratio. Whereas muscovite's fraction goes from 45% in the size fraction 0.5-1 mm in the 20% of s/b to 27% in the particle size of 11.2-16 mm of 30% compression ratio.

Besides of these two main minerals 4 other minerals have been found. The third most present mineral is Dravite, a type of Turmaline, in quantities that in an occasion reaches 10% of the total fraction, although most of the time is less than 5%. Then there are three other minerals that have low concentration, none of them goes upper than 2% in any occasion, they are Cassiterite (a tin ore), Kaolinite (a clay mineral)).

Table 12. Mineral composition of the samples assessed using XRD.

Sample	s/b	Particle size [mm]		Quartz	Muscovite	Dravite	Cassiterite	Kaolinite
		Passing	Retaining					
LP-01	10%	16	11,2	67%	29%	4%	0%	0%
LP-07	10%	1	0,500	56%	32%	10%	0%	2%
LP-09	10%	0,25	0,125	61%	39%	0%	0%	0%
LP-12	20%	16	11,2	59%	38%	2%	1%	0%
LP-13	20%	11,2	8,0	54%	38%	7%	0%	0%
LP-14	20%	8	5,6	56%	41%	3%	0%	0%
LP-15	20%	5,6	4,0	57%	40%	3%	0%	0%
LP-16	20%	4	2,0	65%	31%	4%	0%	0%
LP-17	20%	2	1,0	60%	36%	3%	1%	0%
LP-18	20%	1	0,500	52%	45%	3%	0%	0%
LP-19	20%	0,5	0,250	55%	42%	3%	0%	0%
LP-20	20%	0,25	0,125	52%	44%	2%	0%	2%
LP-21	20%	0,125	0,063	58%	39%	3%	0%	0%
LP-22	20%	0,063	0	48%	47%	5%	0%	0%
LP-23	30%	16	11,2	70%	27%	3%	0%	0%
LP-29	30%	1	0,500	60%	38%	2%	0%	2%
LP-31	30%	0,25	0,125	63%	29%	6%	0%	2%
LP-34	Uncrushed rock sample			63%	33%	2%	0%	2%

An SEM-EDS scan for high density mineral phases was performed on eleven different polished cylindrical sections, impregnated with epoxy resin, with a diameter of 24 mm. Below, the most characteristic and notorious mineral associations and mineral grains observed in the SEM are deployed, starting from high compression ratio and large particle size.

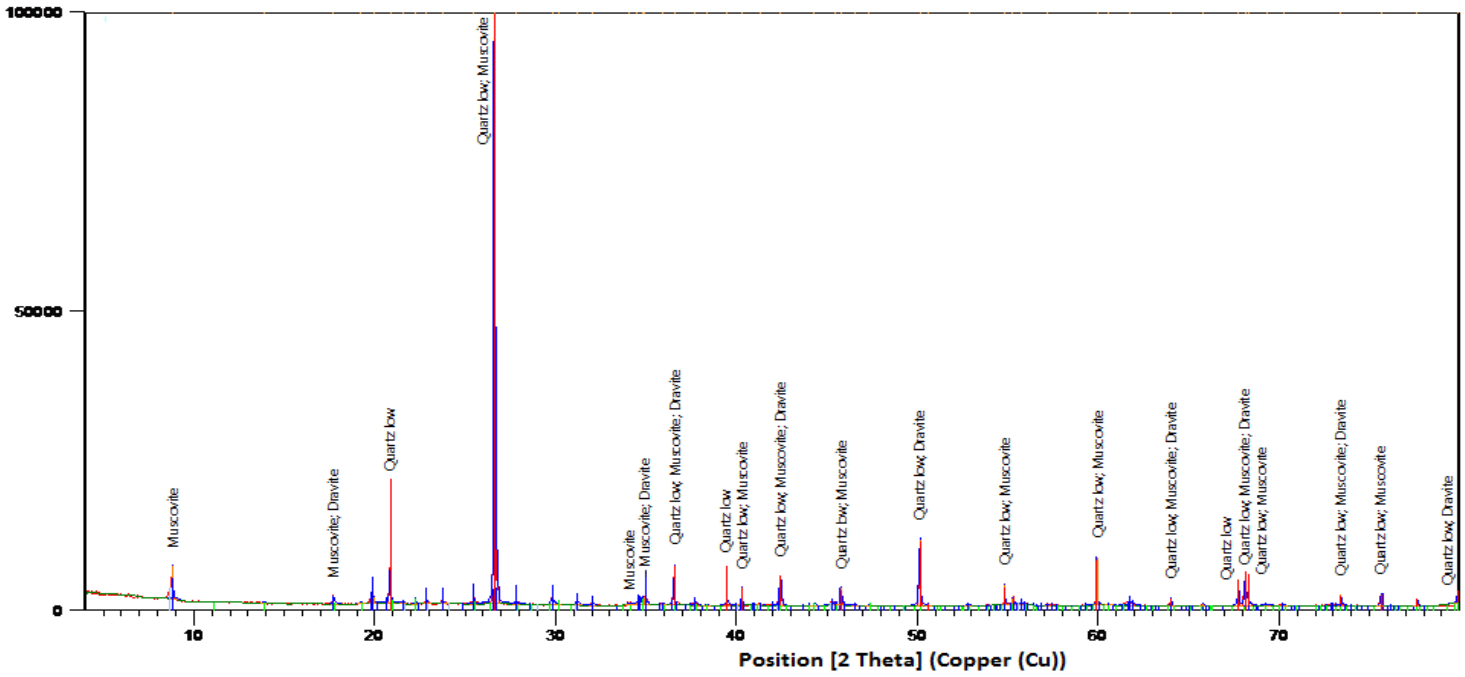

Figure 24. Diffractogram of sample LP-01, obtained with the XRD method.

For 30% of s/b and a particle size range of 1-0.5 mm the only detected particle containing tungsten is shown in Figure 25 and 26. The tungsten ore is Ferberite, it forms veins concurrently to a larger vein of Jarosite, of around 0.7x 0.2 mm of size, and they are contained in a matrix of Quartz and Muscovite, both of them are in contact with the ore in question. In Figure 27 the same picture is shown, this time the contrast and brightness have been adjusted to clearly see the denser minerals. The veins of Ferberite, in a whiter grey, are highlighted from the other minerals.

Not a single grain containing tungsten was found in the polished slab of 30% compression ratio and a particle size range 0.25-0.125 mm. The same situation occurred with the polished sample sections containing material of particle size ranges 5.6-4 mm, 4-2 mm and 2-1 mm, tungsten ore grains were found in neither of these three slabs.

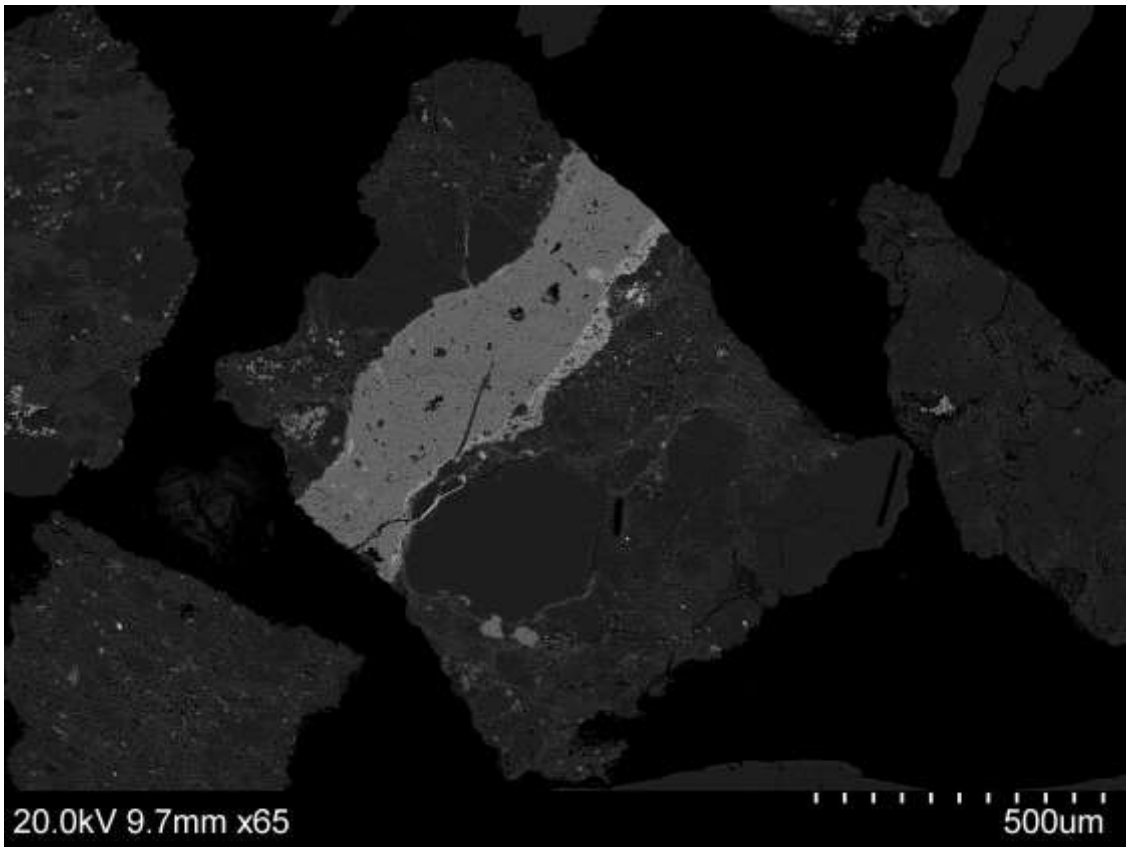

Figure 25. Half grain of Ferberite forming veins from the size fraction <1 mm, after a compression ratio of 30%, observed through SEM.

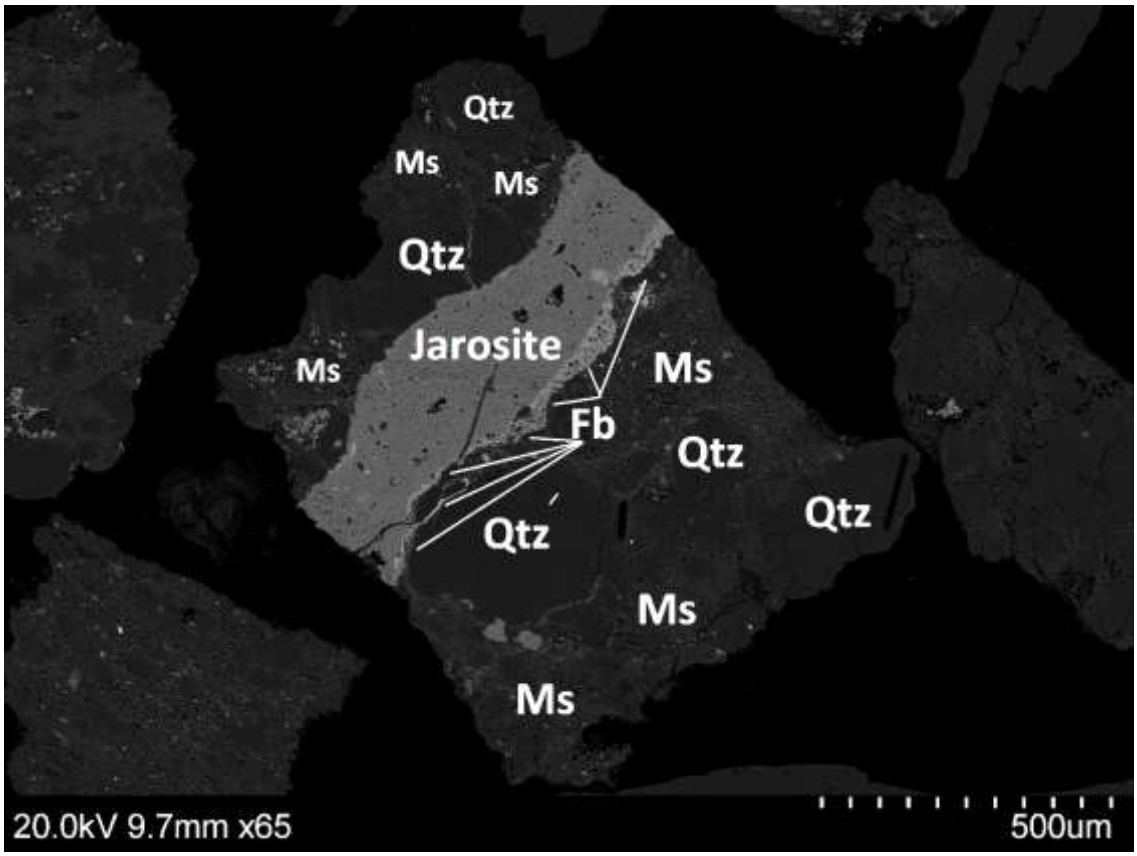

Figure 26. Half grain of Ferberite forming veins from the size fraction <1 mm, after a compression ratio of 30%, observed through SEM with mineral names.

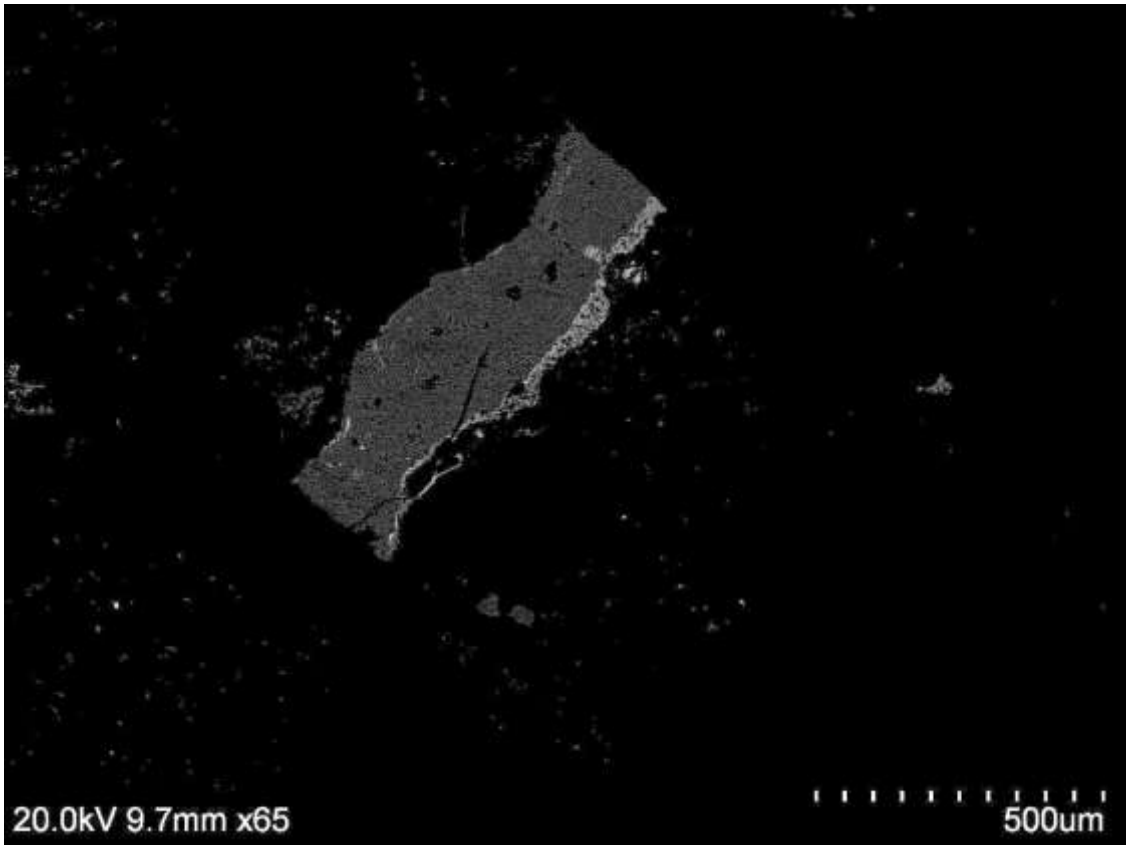

Figure 27. Half grain of Ferberite forming veins from the size fraction <1 mm, after a compression ratio of 30%, observed through SEM with adjusted contrast and brightness to see clearly the dense minerals.

For the 20% of compression ratio and a particle size range of 1-0.5 mm only one tungsten containing particle was found, it is shown in Figure 28 and 29. As in the case before, the tungsten ore is Ferberite, it forms thin veins in a nearly rectangular large matrix of Quartz, of more than 1 mm of length and a little less than 1 mm in width. The particle also contains some Muscovite grains and little Pyrite veins. Iron sulphide as well as the tungsten ore veins are mostly found in the grain boundaries, meaning the cracks have developed in the material through them.

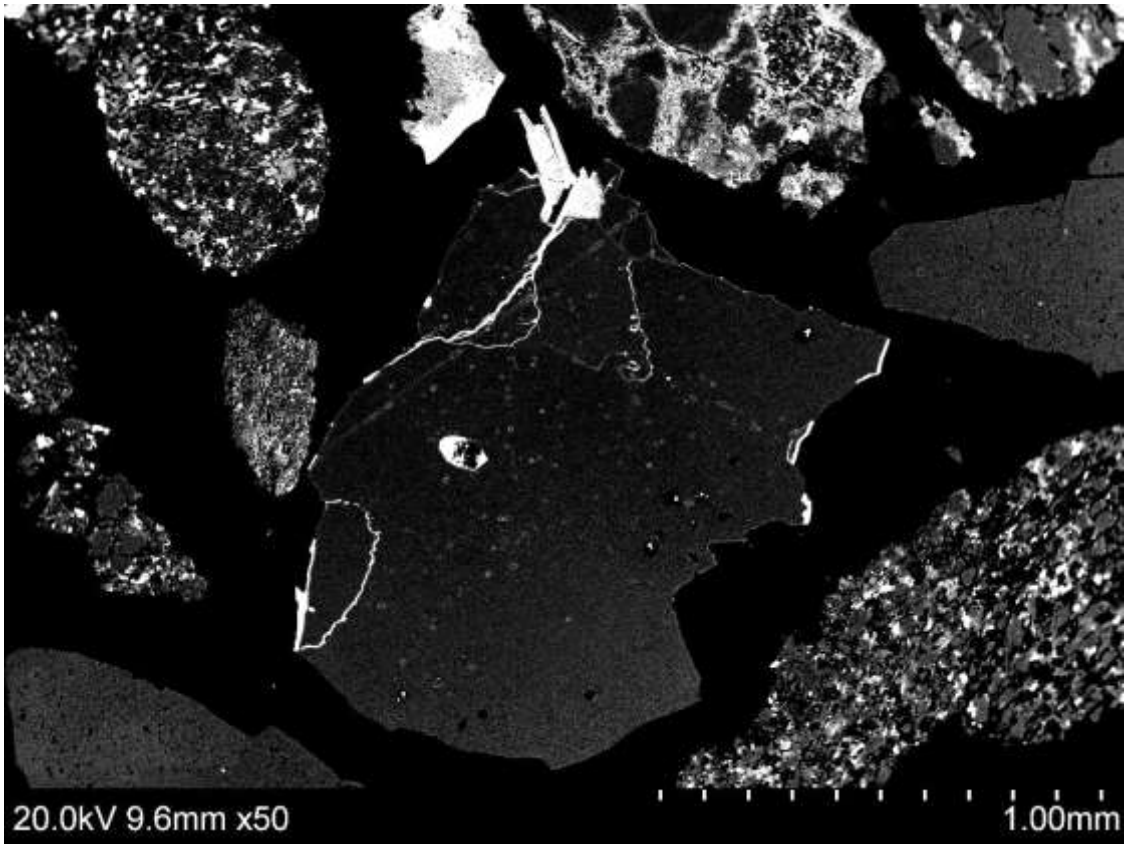

Figure 28. Half grain of Ferberite forming veins from the size fraction <1 mm, after a compression ratio of 30%, observed through SEM.

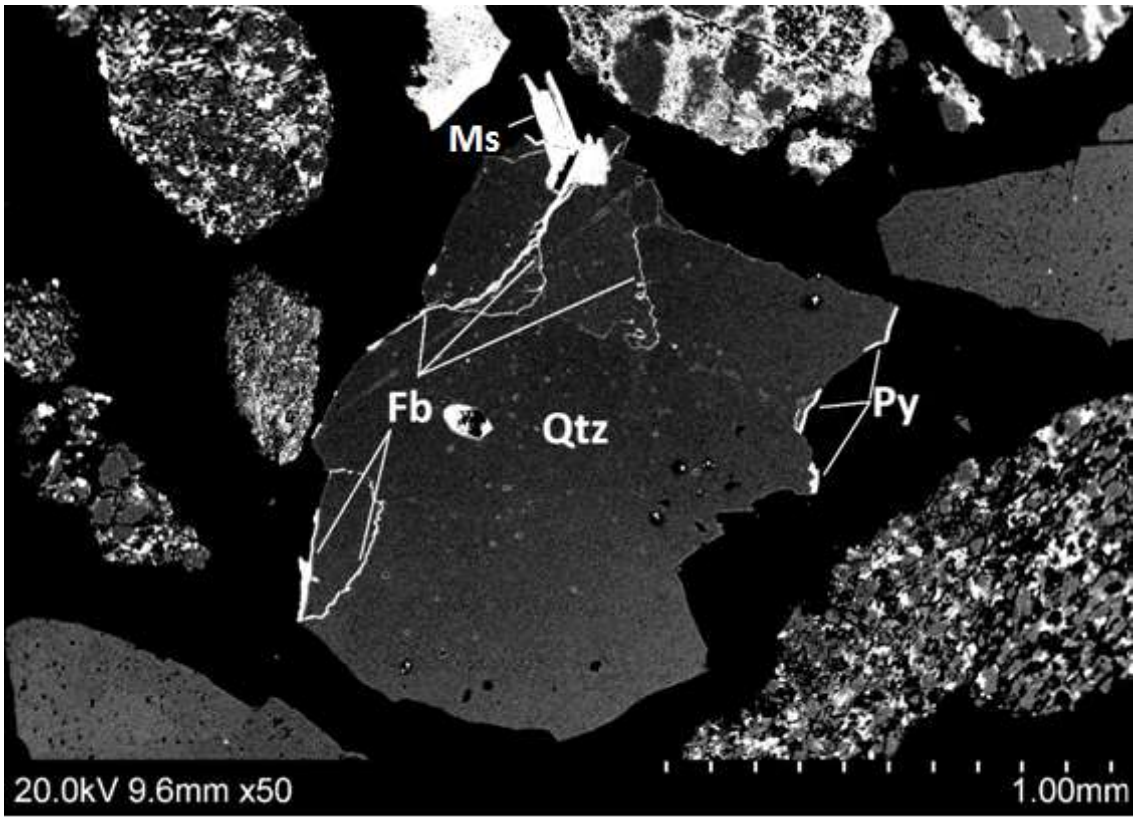

Figure 29. Half grain of Ferberite forming veins from the size fraction <1 mm, after a compression ratio of 20%, observed through SEM with mineral names.

In other cases, a material in the particle size range of 0.5-0.25 mm subjected to a compression ratio of 20%, two separate particles containing tungsten were identified. The first and most notorious can be seen in Figure 30 and 31. It is a composite particle of Ferberite together with a tin oxide (Cassiterite) and Rutile (a titanium oxide). The characteristic needle like structure of the titanium ore can be appreciated in Figure 32, where the contrast and brightness have been adjusted to see the difference in density of the minerals. The Cassiterite appears brighter than Ferberite even though its theoretical density is a little lower, the reason for it can be that traces of light elements occurred in the Ferberite. The grain of Ferberite has a considerable size in comparison with the vein shaped phases that were found in previous samples.

Here tungsten ore was found (Figures 33 and 34), forming a very similar grain than in the case described for sample LP-18 (Figures 28 and 29). Thin veins of Ferberite and Pyrite in a large matrix of Quartz form the particle. As before, some veins appear to be in the grain boundaries, meaning that cracks developed through them. In Figure 35 the contrast and brightness have been modified to appreciate the dense phases in the particle.

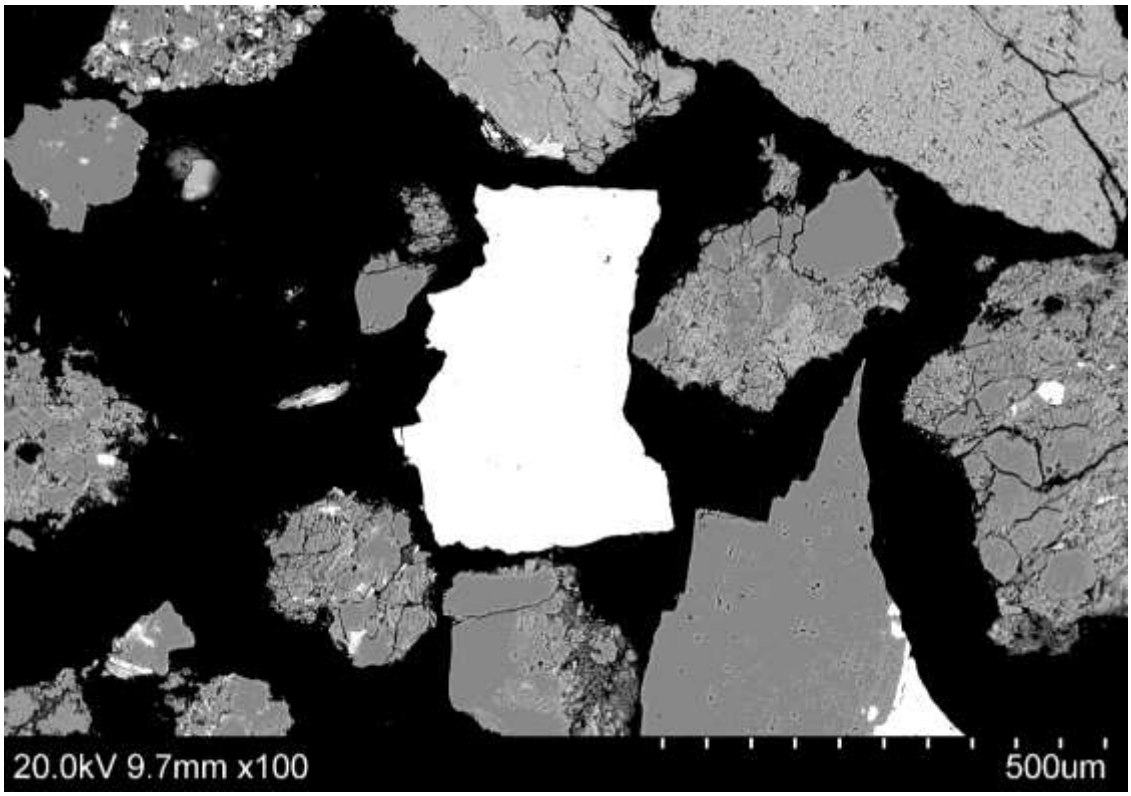

Figure 30. Particle containing Ferberite from the size fraction <0.5 mm, after a compression ratio of 20%, observed through SEM.

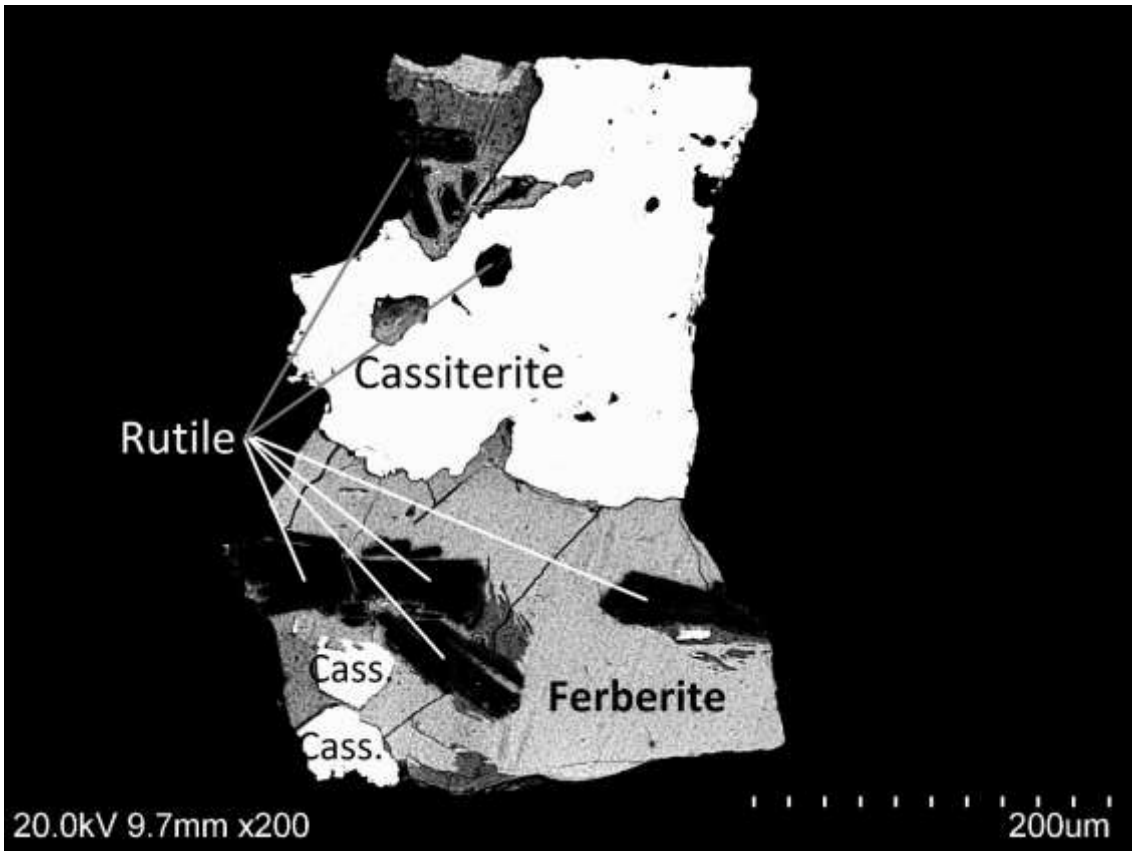

Figure 31. Half grain of Ferberite from the size fraction <0.5 mm, after a compression ratio of 20%, observed through SEM with mineral names.

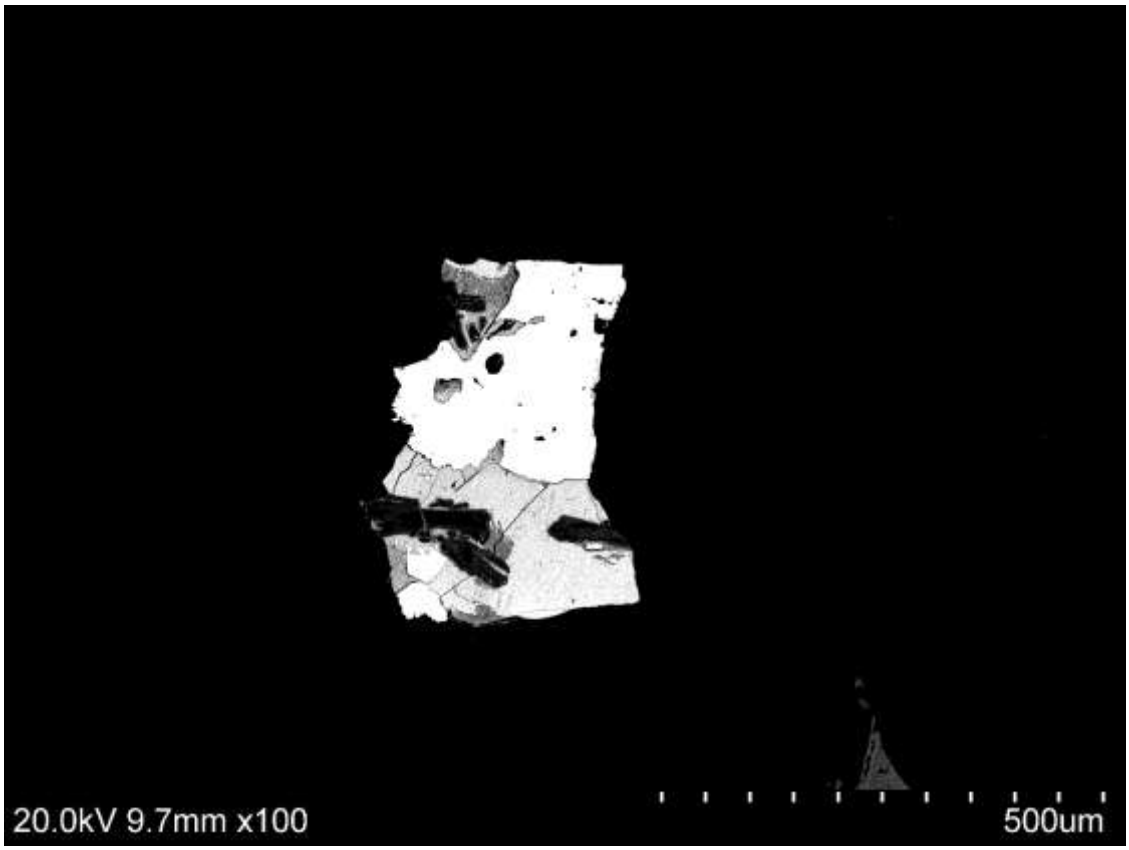

Figure 32. Half grain of Ferberite from the size fraction <0.5 mm, after a compression ratio of 20%, observed through SEM with adjusted contrast and brightness to see clearly the difference in density of the mineral phases.

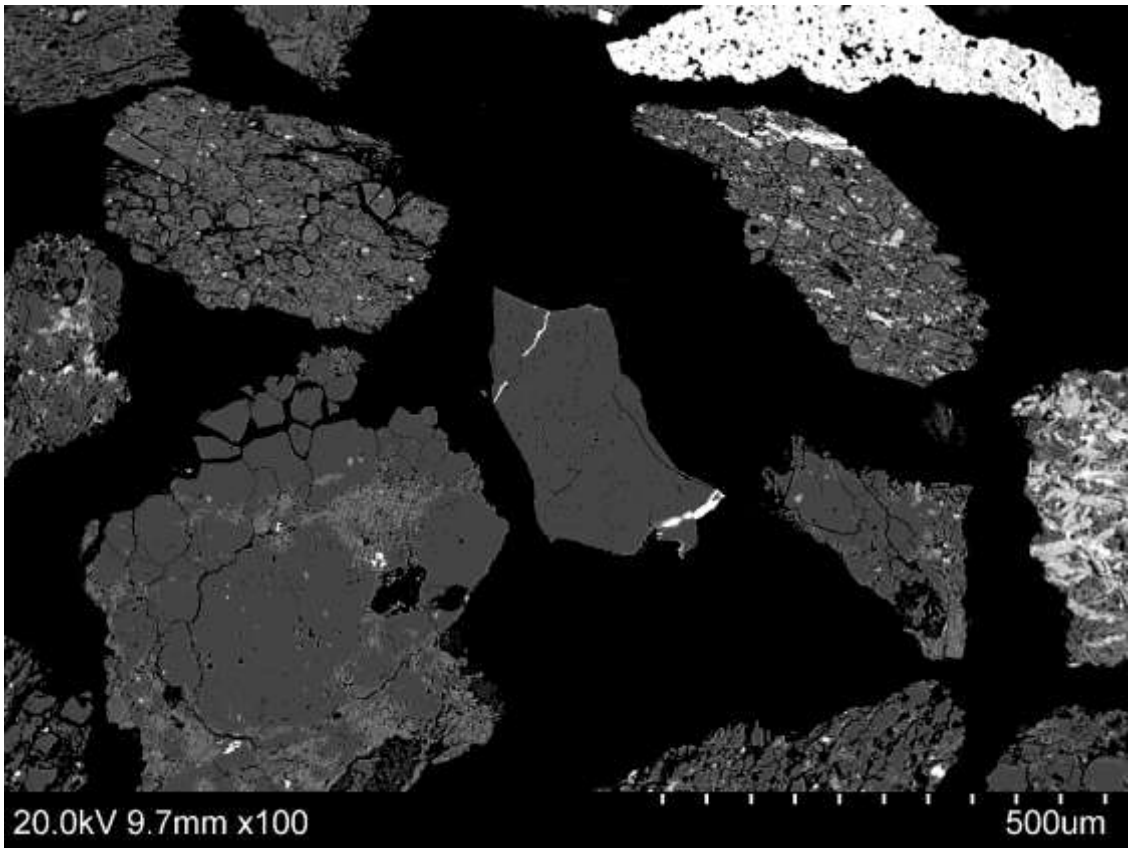

Figure 33. Half grain of Ferberite forming veins from the size fraction <0.5 mm, after a compression ratio of 20%, observed through SEM.

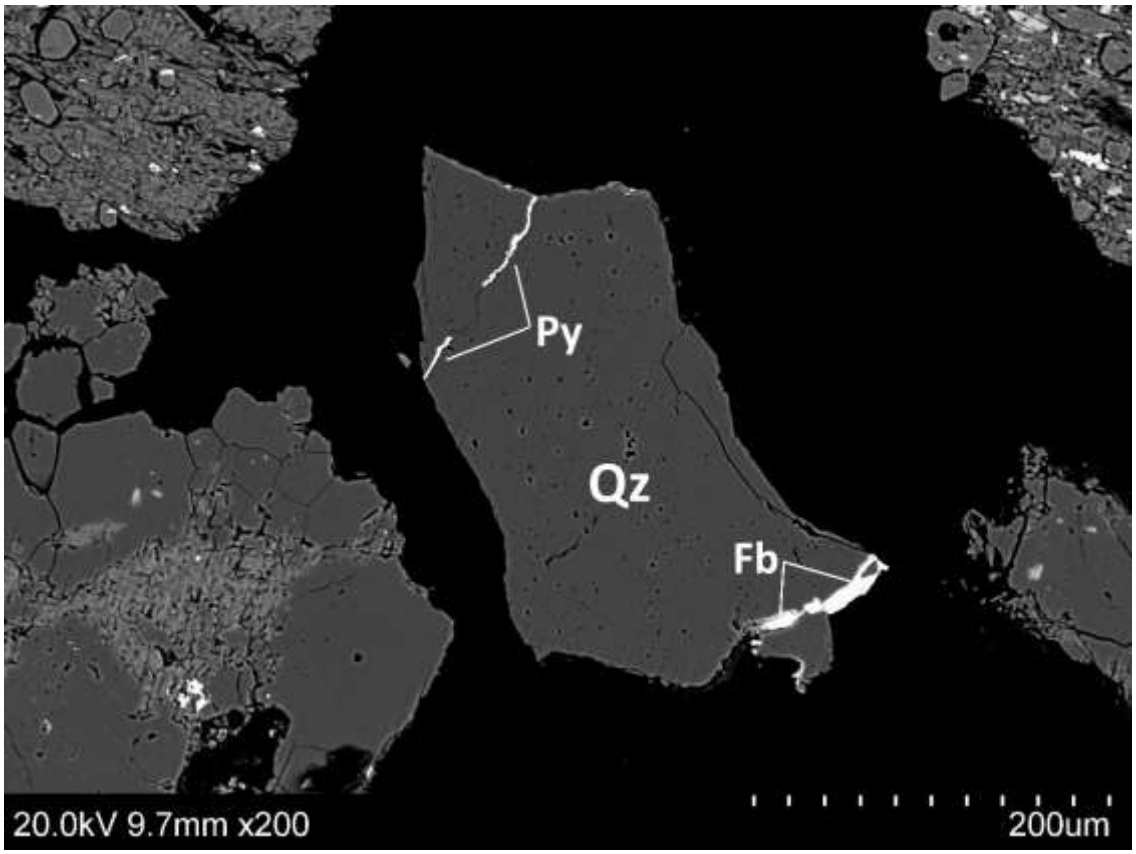

Figure 34. Half grain of Ferberite forming veins from the size fraction <0.5 mm, after a compression ratio of 20%, observed through SEM with mineral names.

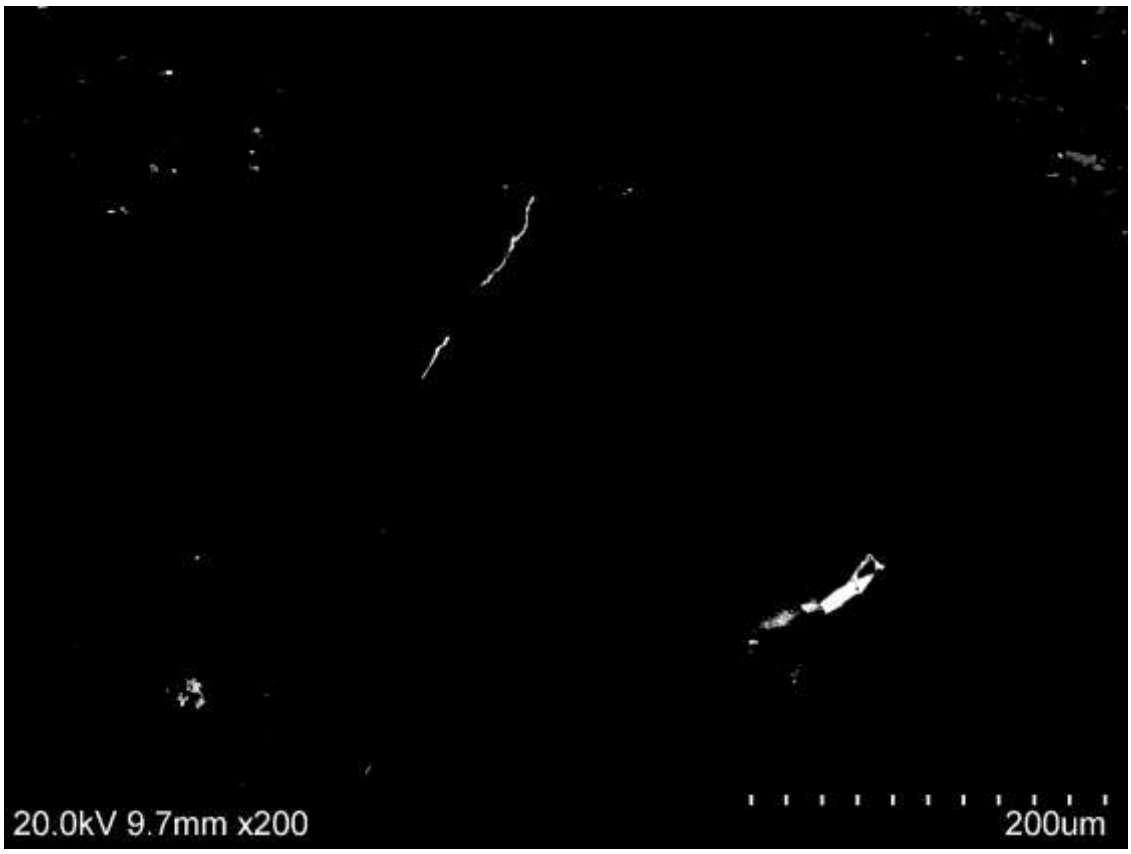

Figure 35. Half grain of Ferberite forming veins from the size fraction <0.5 mm, after a compression ratio of 20%, observed through SEM with adjusted contrast and brightness to see clearly the dense minerals.

The first completely liberated particle of tungsten ore was found in sample LP-20 (20% of compression ratio in the particle size range of 0.25-0.125 mm). It is Ferberite and can be seen in Figures 36 and 37, the latter has been modified so the differences in density in the same mineral phase could be appreciated. A darker area appears in the particle, this can be caused by traces of lighter elements in the mineral.

In the same size fraction two different half particles containing tungsten were identified. The first can be seen in Figures 38 and 39 where roughly half of the particle is Ferberite and it is in contact with Muscovite and Quartz. The reader can note that besides the main Ferberite grain of a considerable size there are two tiny grains of the same mineral inside the matrix. The whole particle is notably fractured.

At last, traces of Ferberite where found in another particle (Figures 40 and 41). The whole particle appears to have a high density, this could be understood when the chemical composition of the particle was checked. It is mostly composed by As, Fe and Al, they are the reason for the elevated density, they could be alteration mineral of Pyrite and Arsenopyrite (both of them have been also found unaltered). In Figure 41, after heightening the contrast to the maximum, the Ferberite grains could be appreciated.

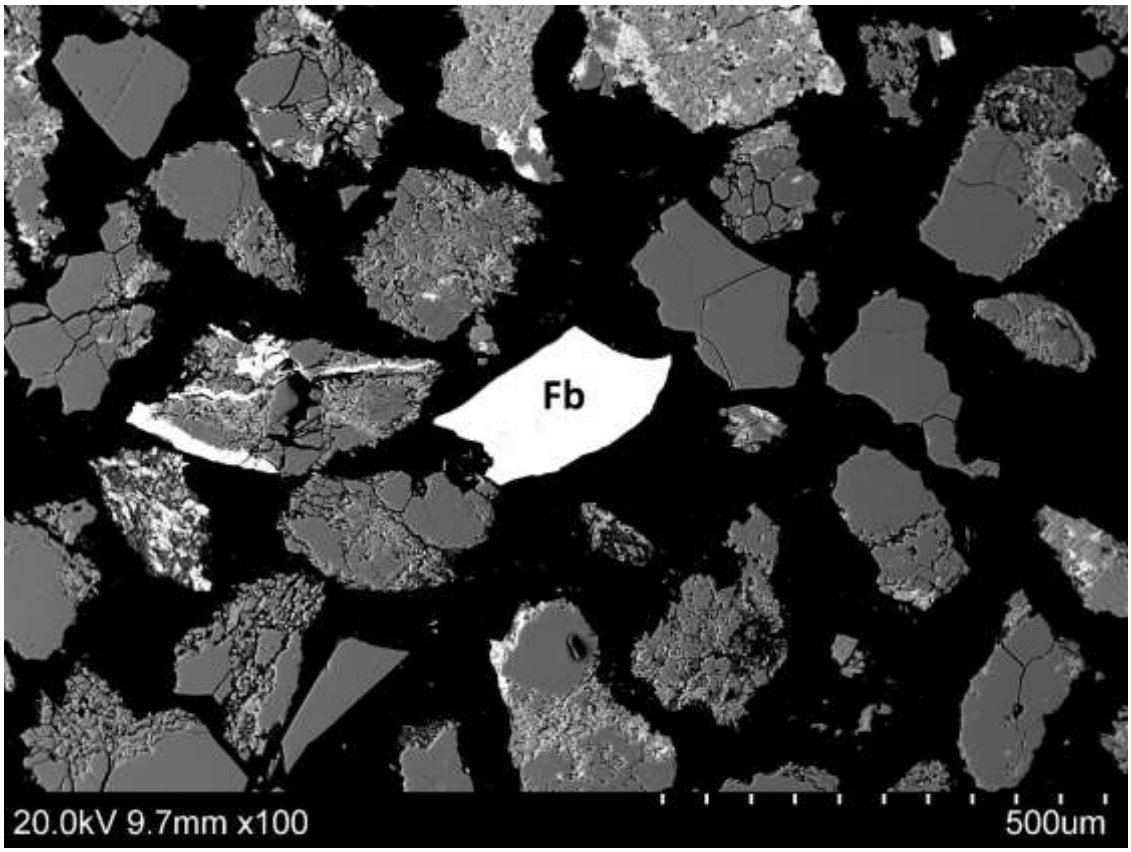

Figure 36. Liberated particle of Ferberite from the size fraction <0.25 mm, after a compression ratio of 20%, observed through SEM.

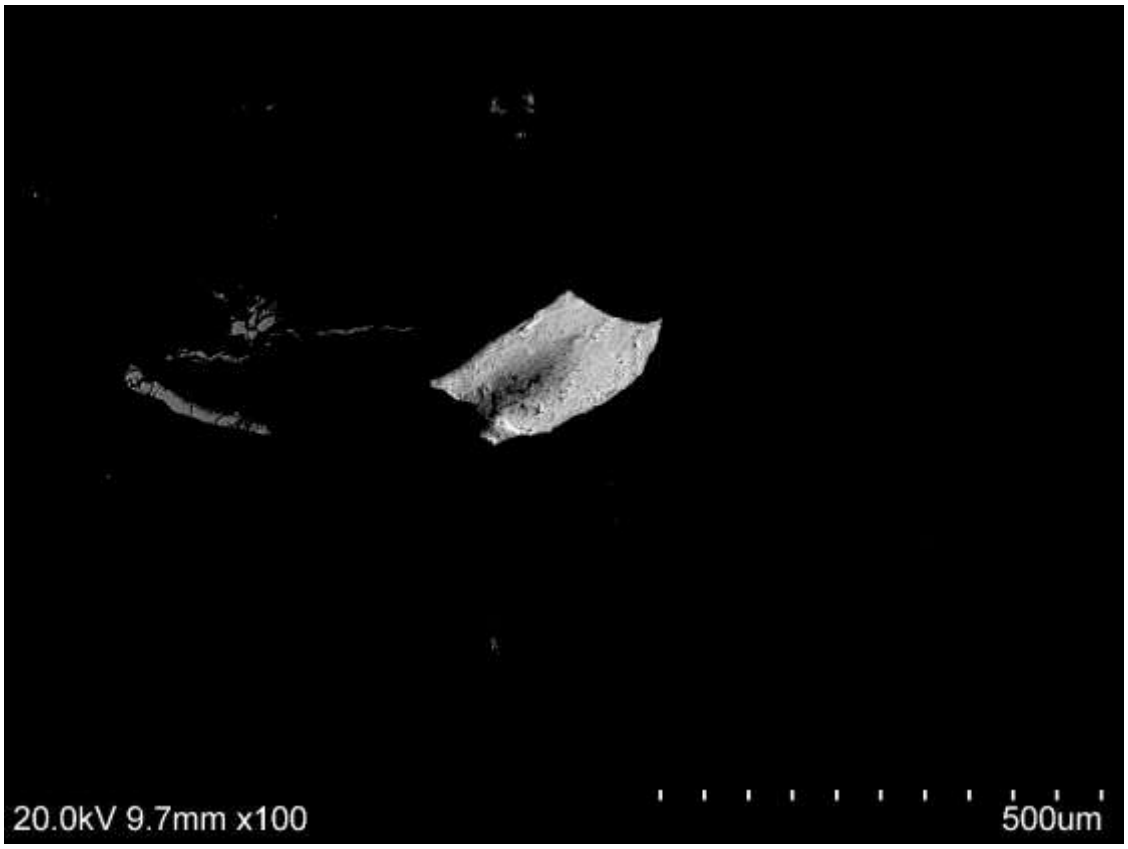

Figure 37. Liberated particle of Ferberite from the size fraction <0.25 mm, after a compression ratio of 20%, observed through SEM with adjusted contrast and brightness to see the differences in density in the same grain.

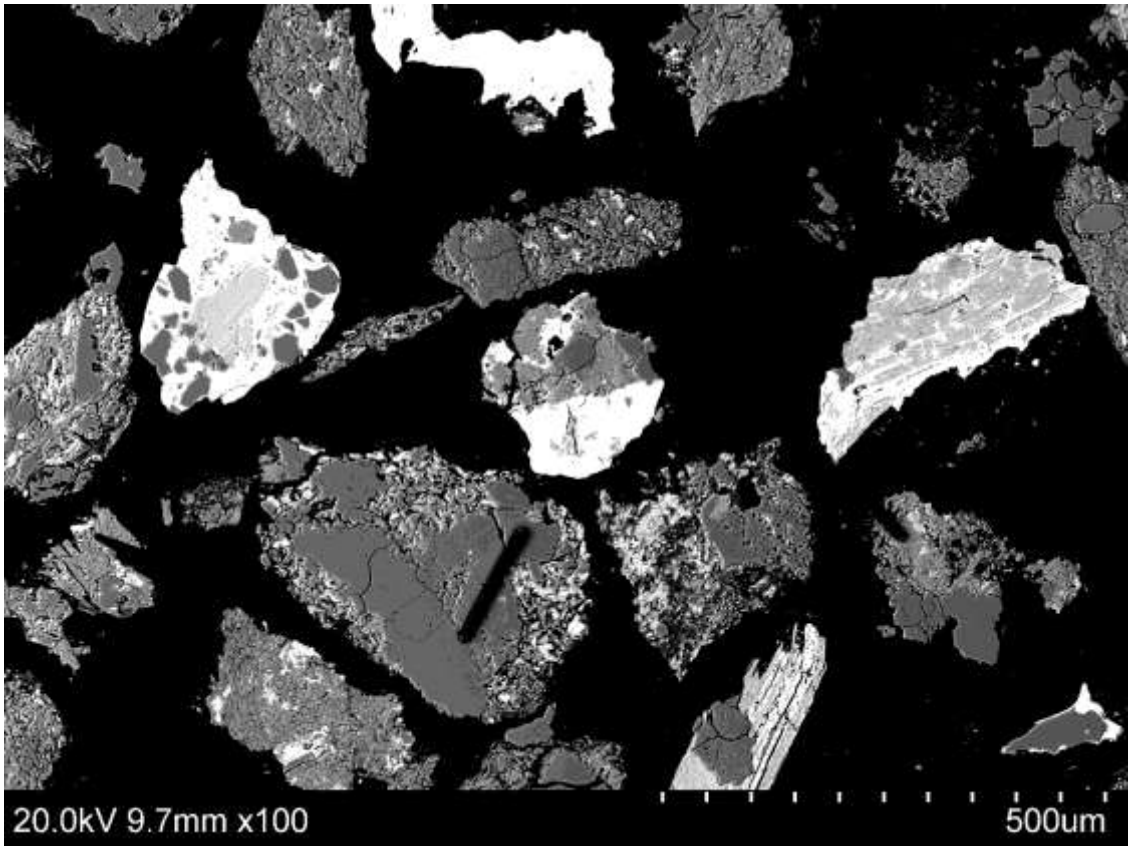

Figure 38.Particle of Ferberite from the size fraction <0.25 mm, after a compression ratio of 20%, observed through SEM.

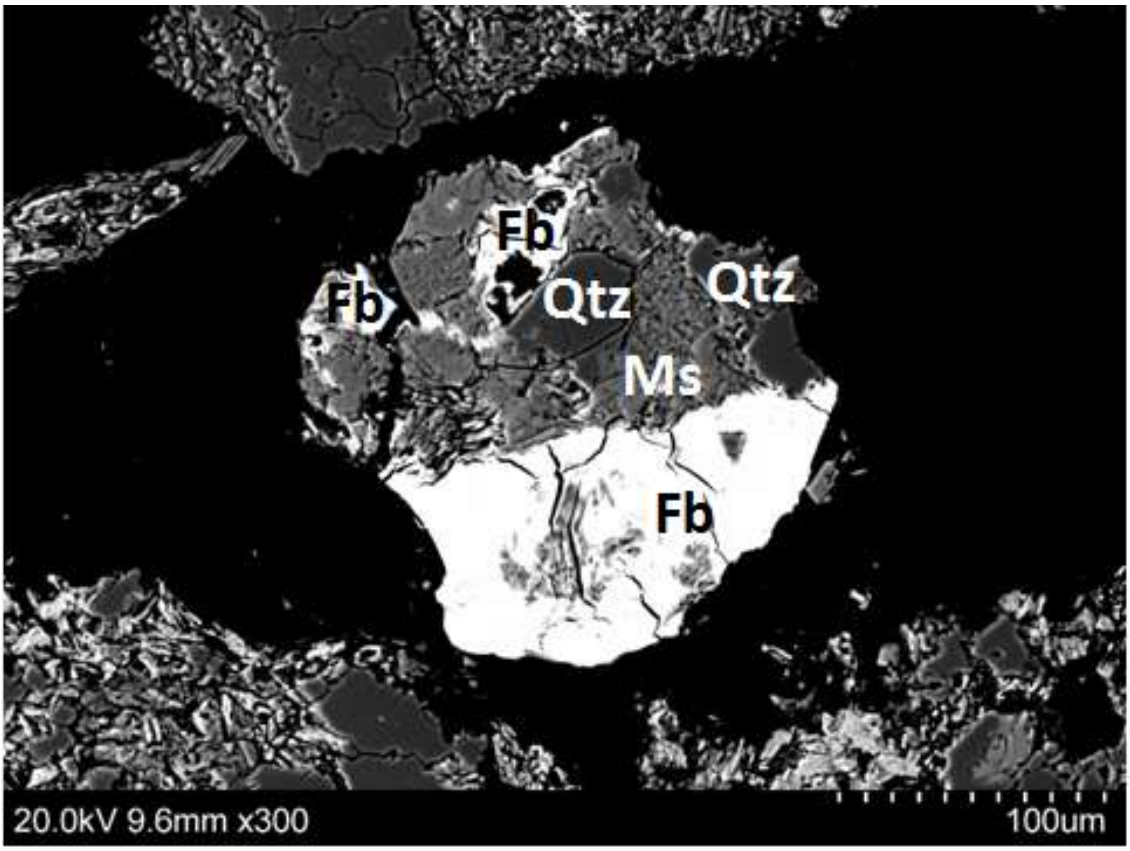

Figure 39. Half grain of Ferberite forming veins from the size fraction <0.25 mm, after a compression ratio of 20%, observed through SEM with mineral names.

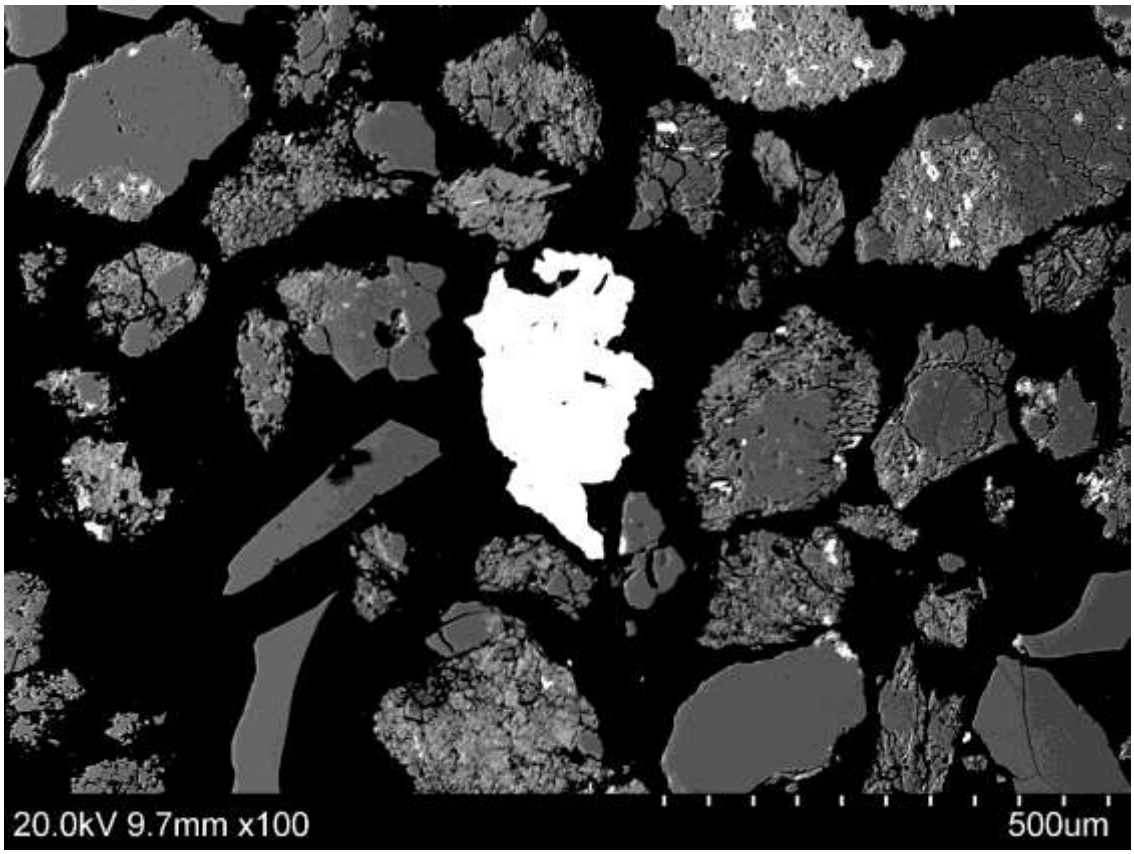

Figure 40. Particle containing Ferberite from the size fraction <0.25 mm, after a compression ratio of 20%, observed through SEM.

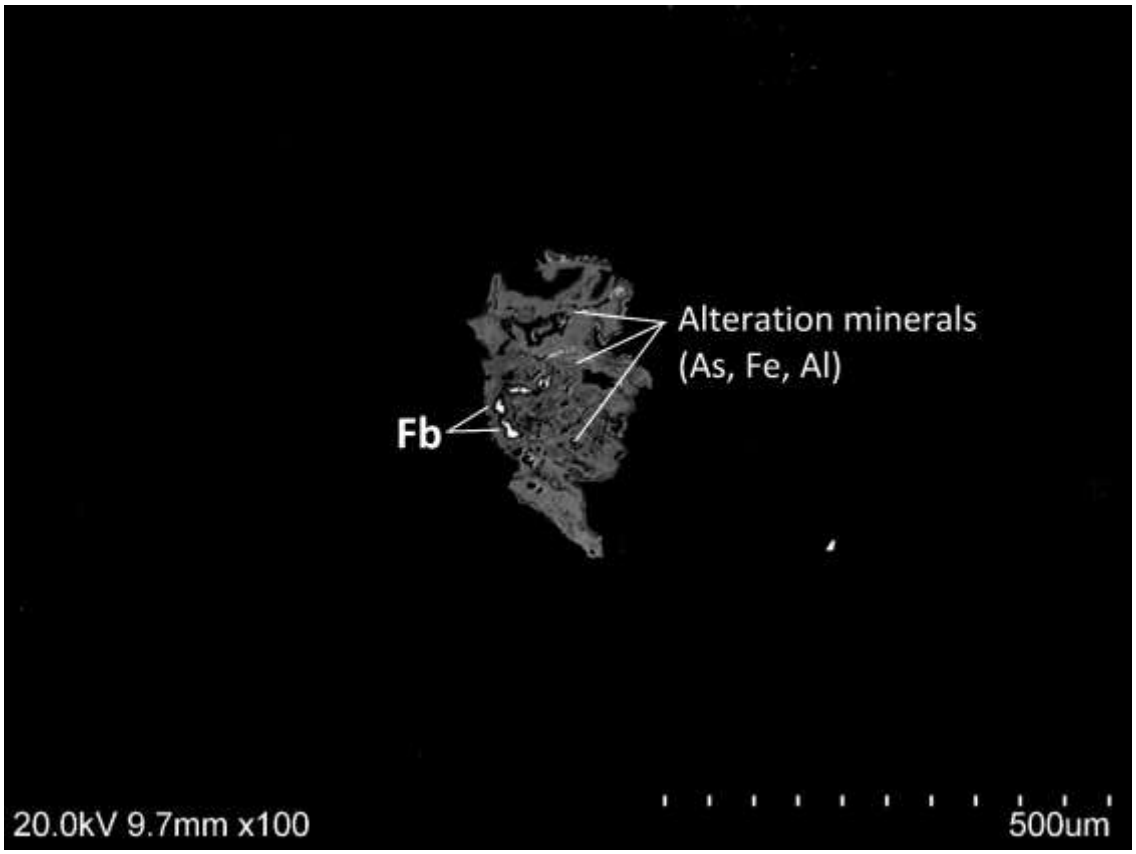

Figure 41. Particle containing traces of Ferberite from the size fraction <0.25 mm, after a compression ratio of 20%, observed through SEM with adjusted contrast and brightness to see clearly the dense minerals and mineral names.

In the sample with material subjected to a compression ratio of 20% and a particle size range from 0.125-0.063 mm is where the bigger amount of tungsten ore particles has been found. Figure 42 and 43 show a liberated Scheelite particle of a nearly circular shape, it was the first Scheelite mineral found in the samples. Figure 44 represents the same particle, but like it has been done before, contrast and brightness have been adjusted so that the differences in density in the same mineral phase could be seen. A vertical crack nearly cuts the surface of the particle in half.

Figure 45 and 46 show two liberated Ferberite minerals one next to the other. Both of them have one dimension much more developed than the other. As before, in Figure 47 shows the differences in density inside the own Ferberite mineral. For the vertical particle in the left, it can be seen that nearly the entirety of it has the same density. In the other hand, the horizontal particle has many incursions of lower density elements.

Figure 48 and 49 show a composite particle of Ferberite and Quartz, there are three grains of vein shaped Ferberite surrounding the gangue. As has been seen and explained in previous cases, the veins of Ferberite also occur in the grain boundaries. Figure 50, with adjusted in

contrast and brightness allow the reader to see how there is a denser area in the upper part of the top grain, and also it allows to observe small cracks in the ore grains.

In the same sample a similar particle than right above was found (Figure 51 and 52). A composite particle of a tungsten ore forming veins (Ferberite) together with a gangue of phosphates and sulphates. It appears to be a liberated particle, until the contrast is heightened and a different and lighter mineral phase is discovered in the middle being sandwiched by the Ferberite veins (Figure 53). As before, the tungsten minerals occur in the grain boundaries. The bright particles that appear next to the studied composite particle are Pyrites and a Zirconite.

The last particle containing tungsten in sample LP-21 is shown in Figures 54 and 55. Like in Figure 17 at first it seems to be a liberated particle. The whole particle has a high density. Only when the contrast and brightness is adjusted the Ferberite grains can be differed from the gangue. Alteration minerals containing mainly As, Fe and K and traces of P and Na and alteration minerals containing mainly As, Fe and Al and traces of K and P. Jarosite is probably one of them, it would explain the presence of Fe and K. In Figure 56 the higher density of the Ferberite grain in the left can be appreciated.

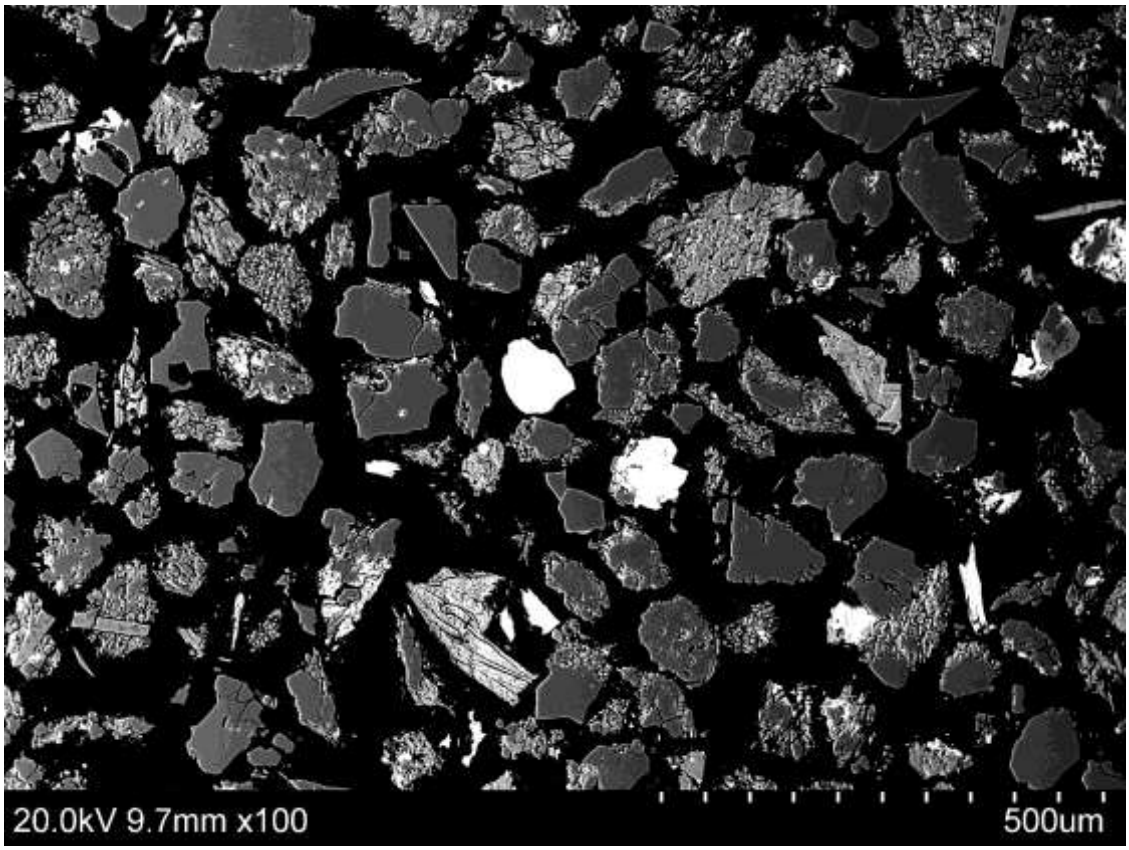

Figure 42. Liberated particle of Scheelite from the size fraction <0.125 mm, after a compression ratio of 20%, observed through SEM.

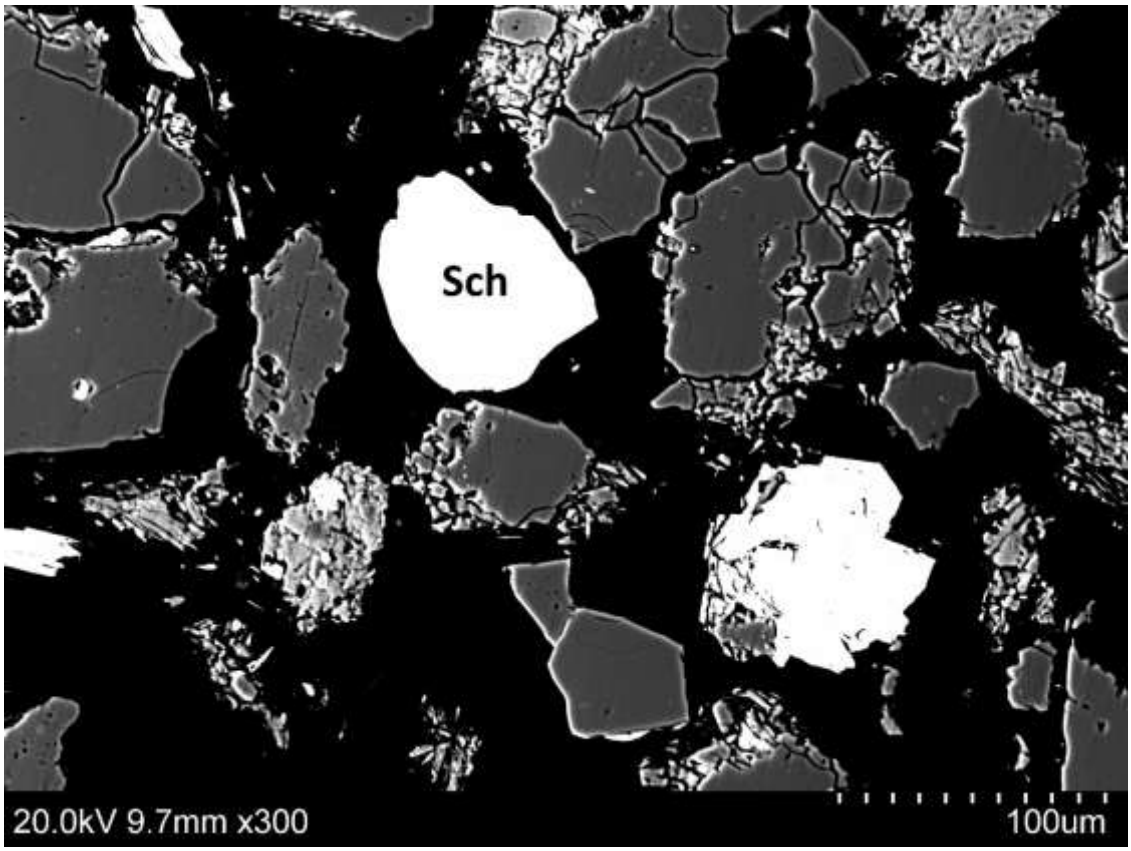

Figure 43. Liberated particle of Scheelite from the size fraction <0.125 mm, after a compression ratio of 20%, observed through SEM with mineral names.

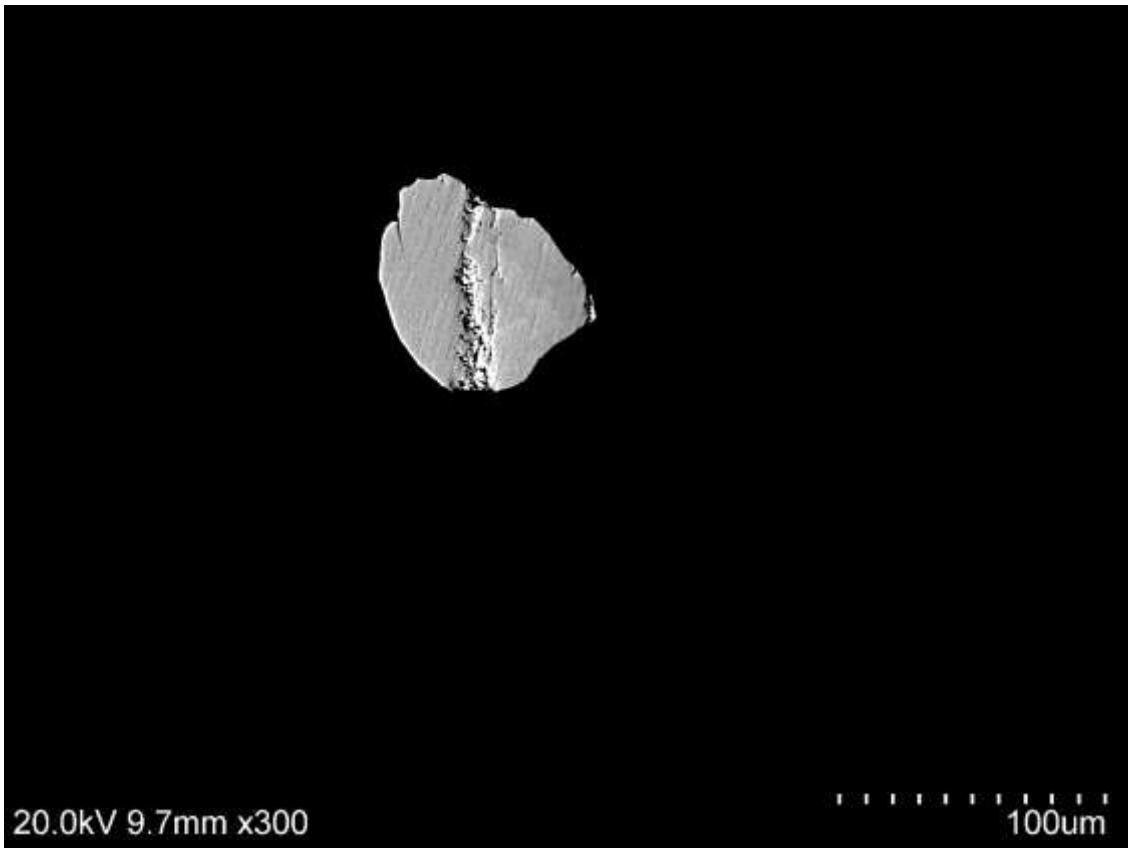

Figure 44. Liberated particle of Scheelite from the size fraction <0.125 mm, after a compression ratio of 20%, observed through SEM with adjusted contrast and brightness to see the differences in density in the same grain.

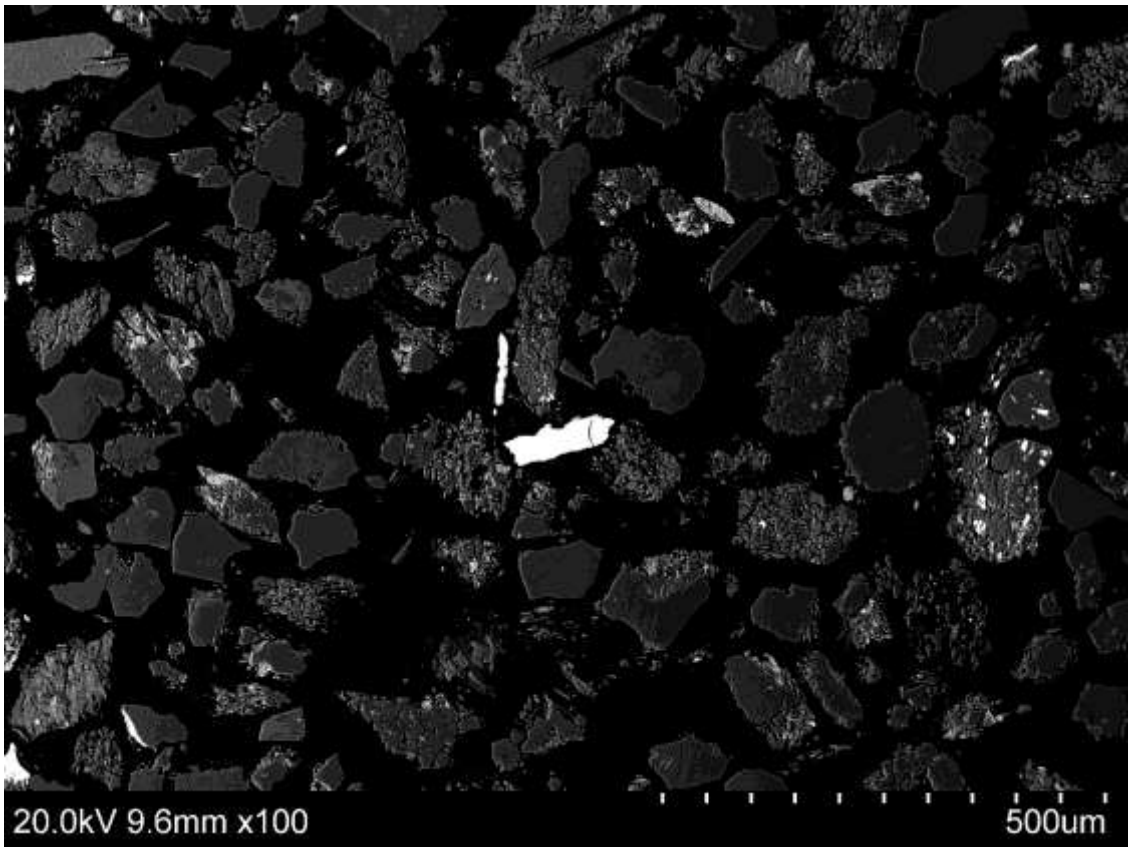

Figure 45. Liberated particles of Ferberite from the size fraction <0.125 mm, after a compression ratio of 20%, observed through SEM.

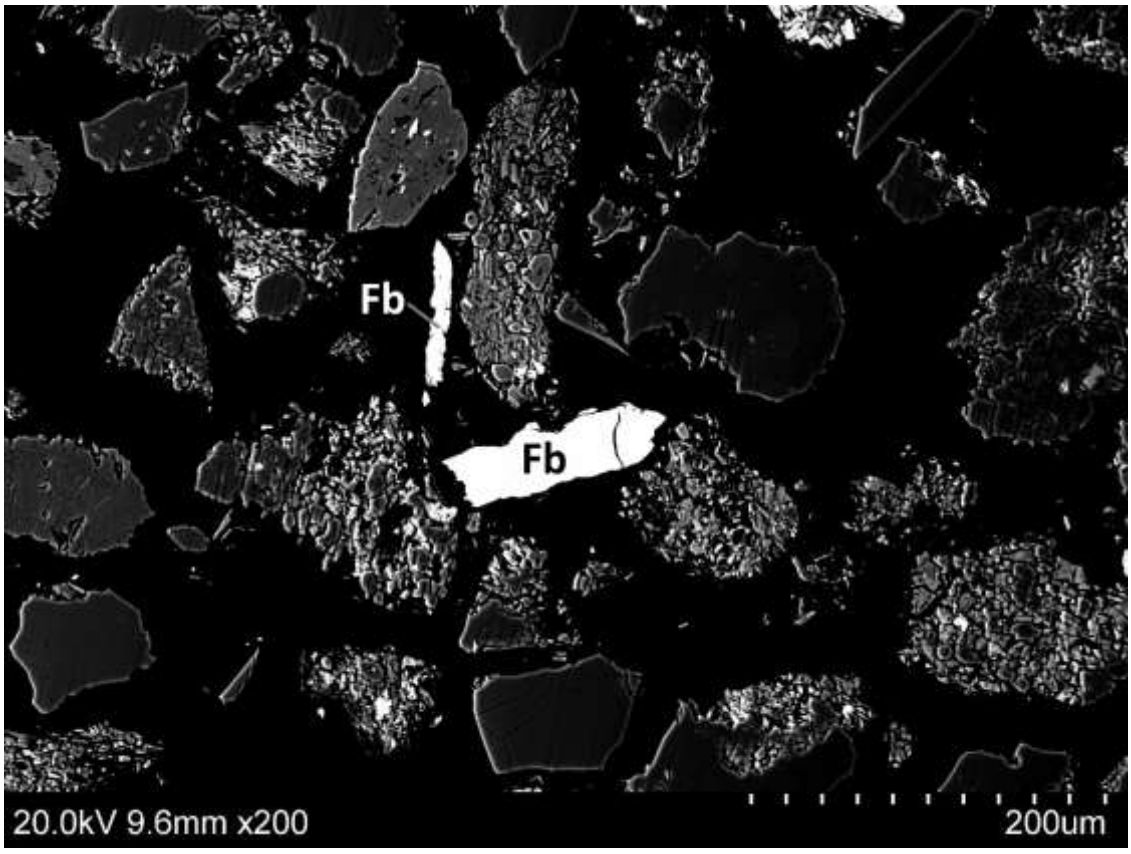

Figure 46. Liberated particles of Ferberite from the size fraction <0.125 mm, after a compression ratio of 20%, observed through SEM with mineral names.

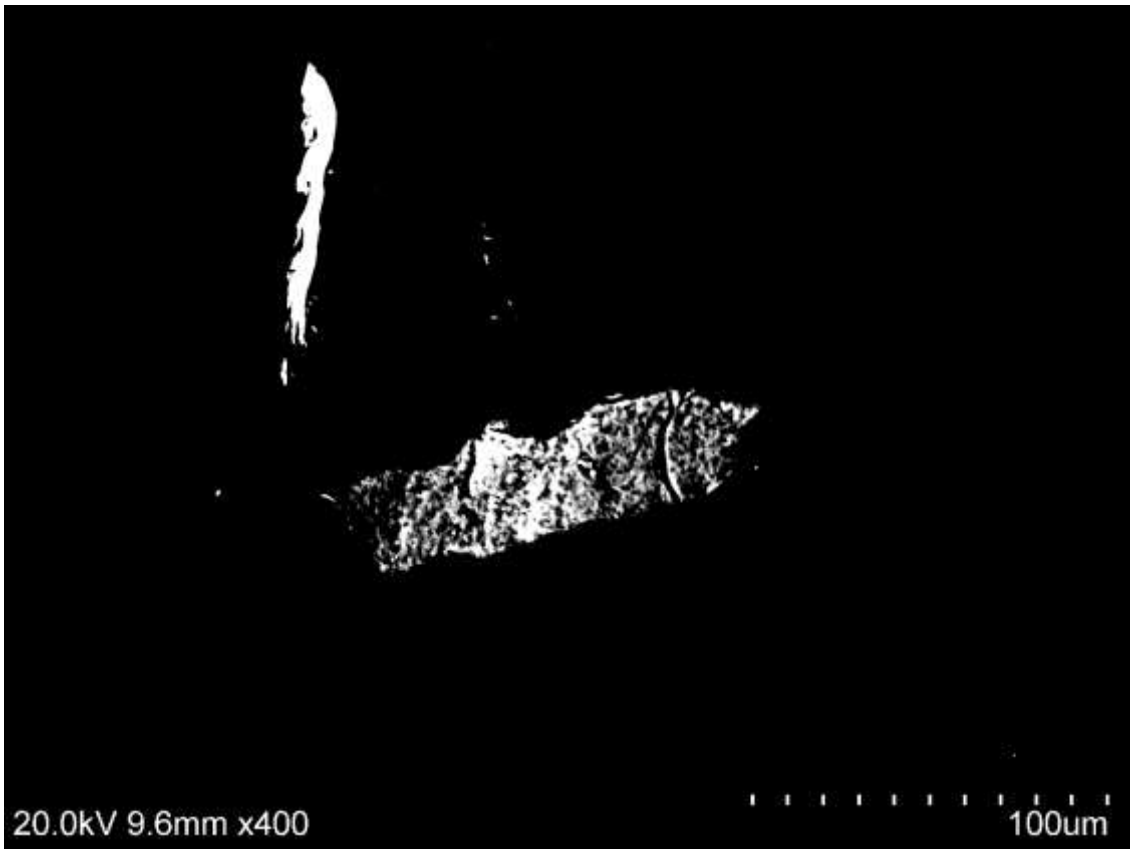

Figure 47. Liberated particles of Ferberite from the size fraction <0.125 mm, after a compression ratio of 20%, observed through SEM with adjusted contrast and brightness to see the differences in density in the same grain.

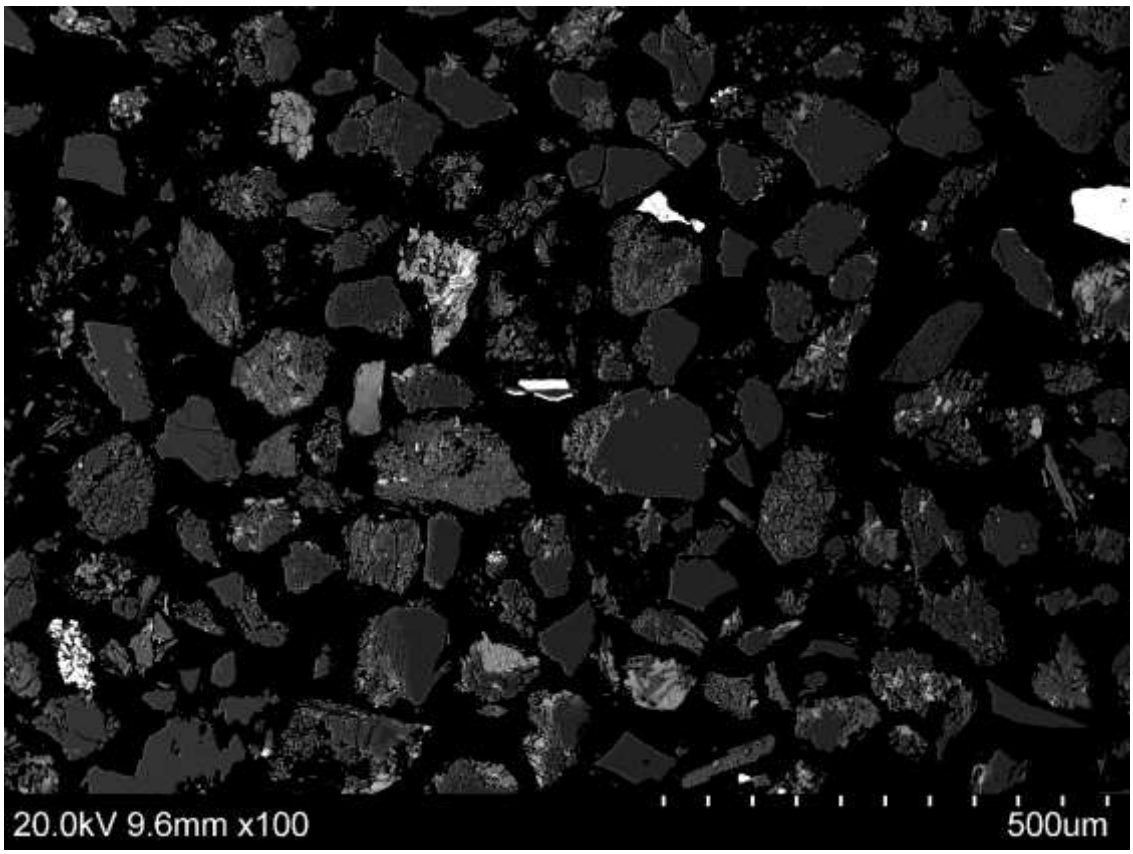

Figure 48. Half grain of Ferberite forming veins from the size fraction <0.125 mm, after a compression ratio of 20%, observed through SEM.

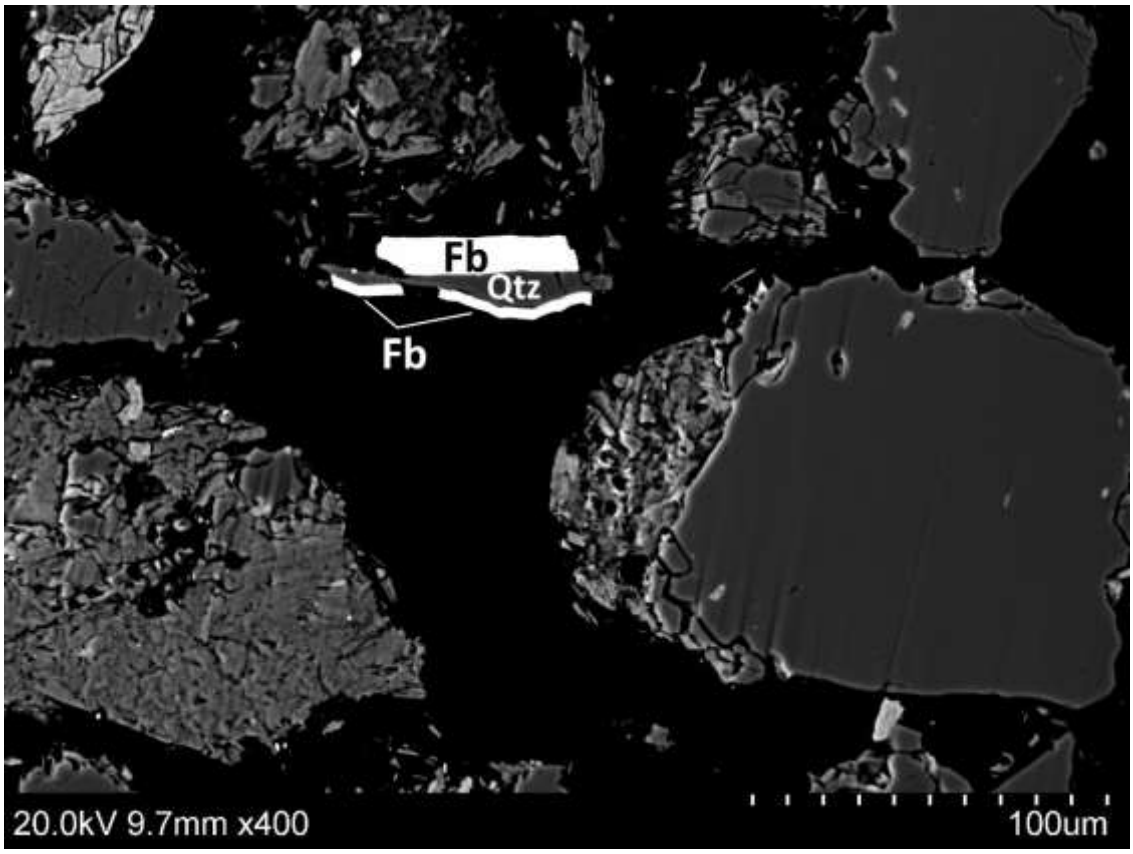

Figure 49. Half grain of Ferberite forming veins from the size fraction <0.125 mm, after a compression ratio of 20%, observed through SEM with mineral names.

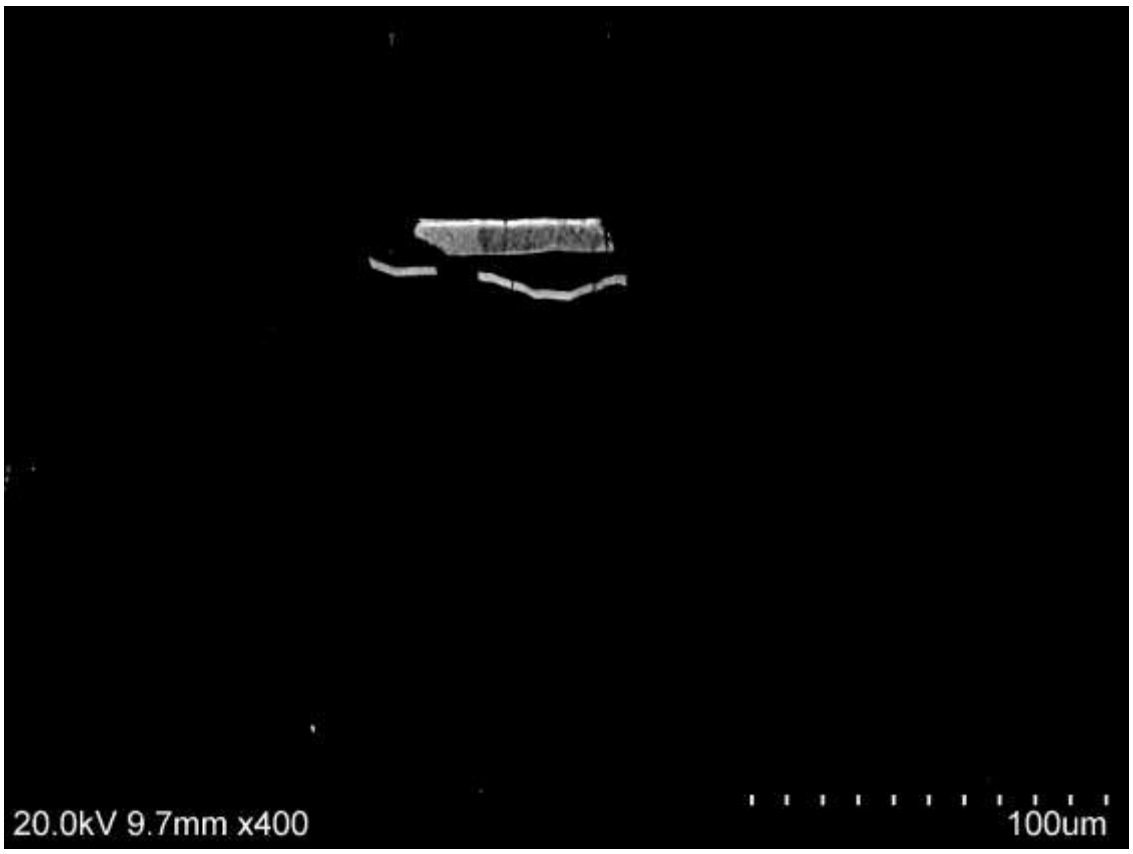

Figure 50. Half grain of Ferberite forming veins from the size fraction <0.125 mm, after a compression ratio of 20%, observed through SEM with adjusted contrast and brightness to see the differences in density in the same grain.

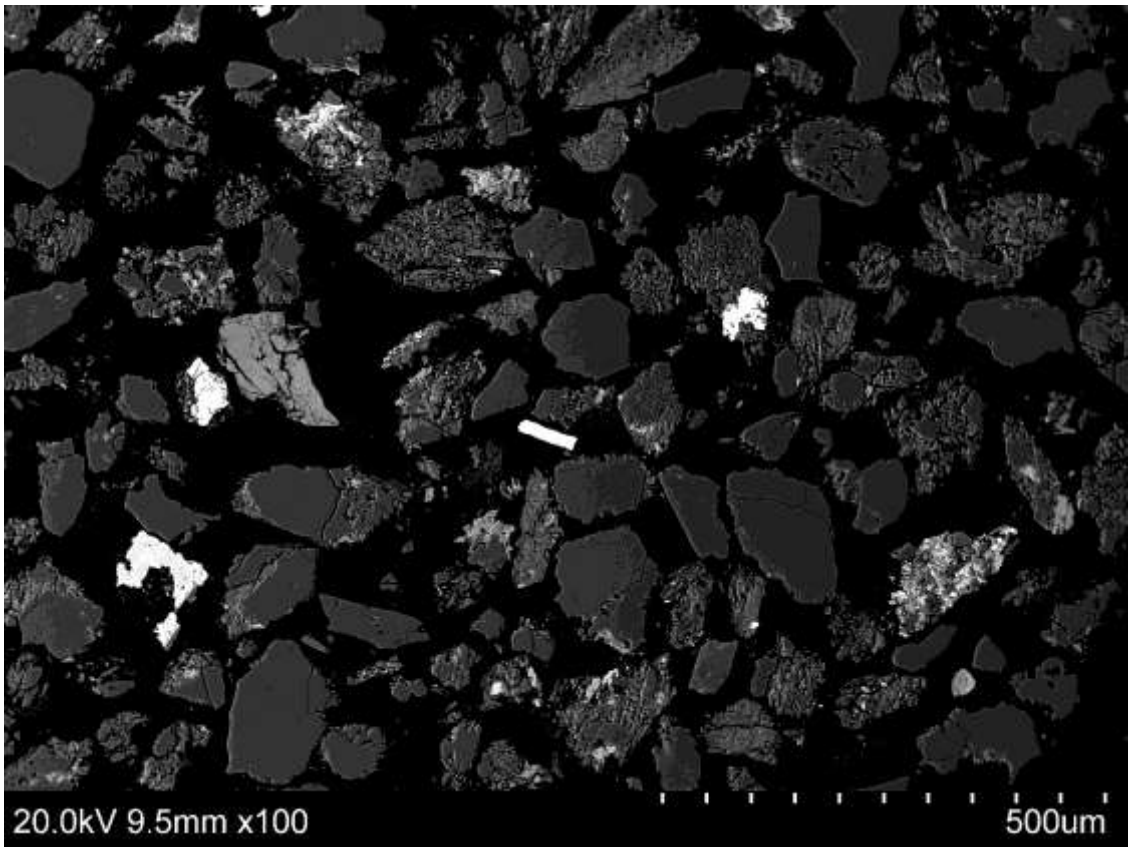

Figure 51. Particle containing Ferberite forming veins from the size fraction <0.125 mm, after a compression ratio of 20%, observed through SEM.

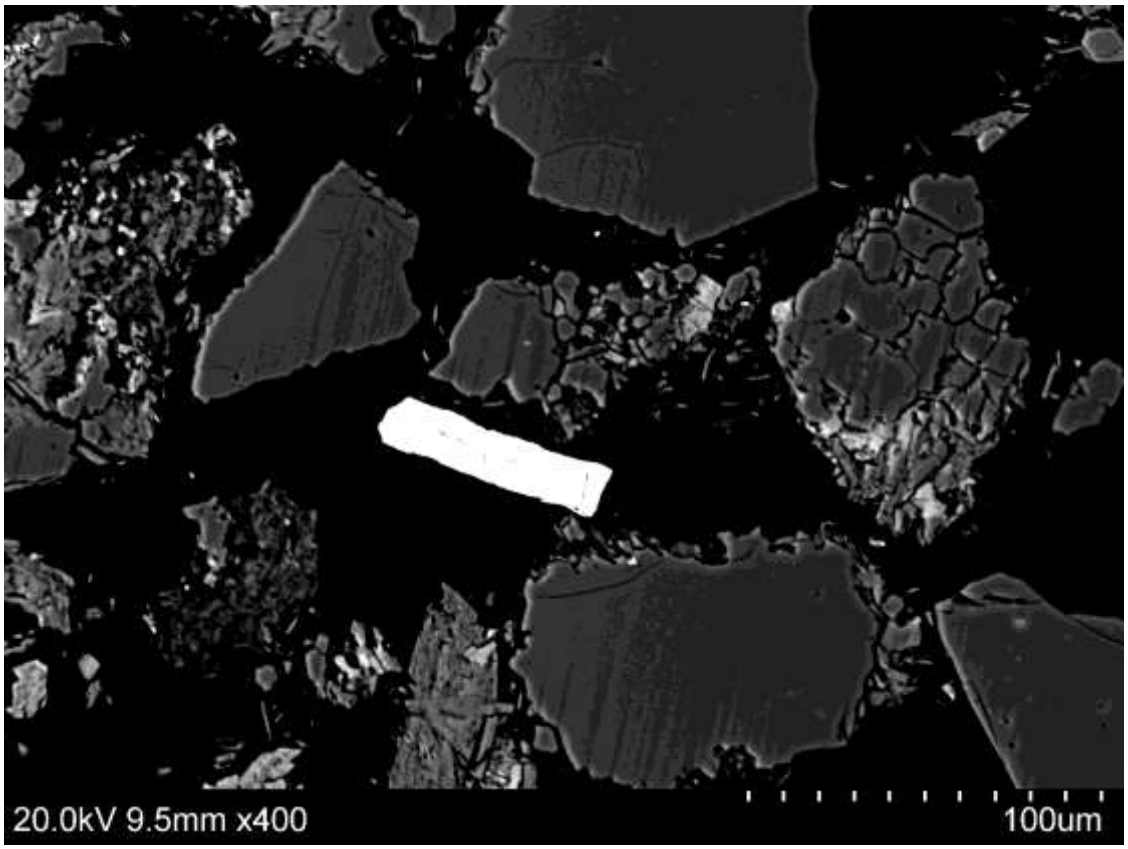

Figure 52. Particle containing Ferberite forming veins from the size fraction <0.125 mm, after a compression ratio of 20%, observed through SEM zoomed.

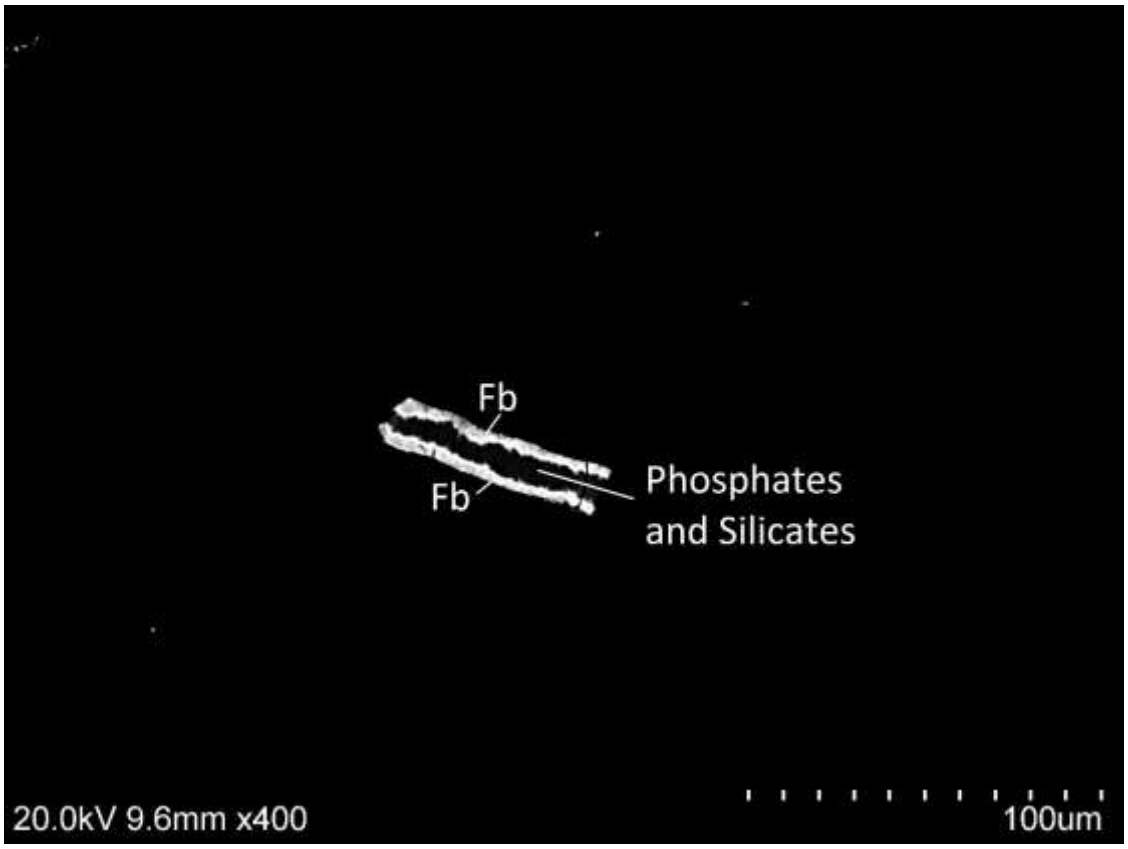

Figure 53. Half grain of Ferberite forming veins from the size fraction <0.125 mm, after a compression ratio of 20%, observed through SEM with mineral names.

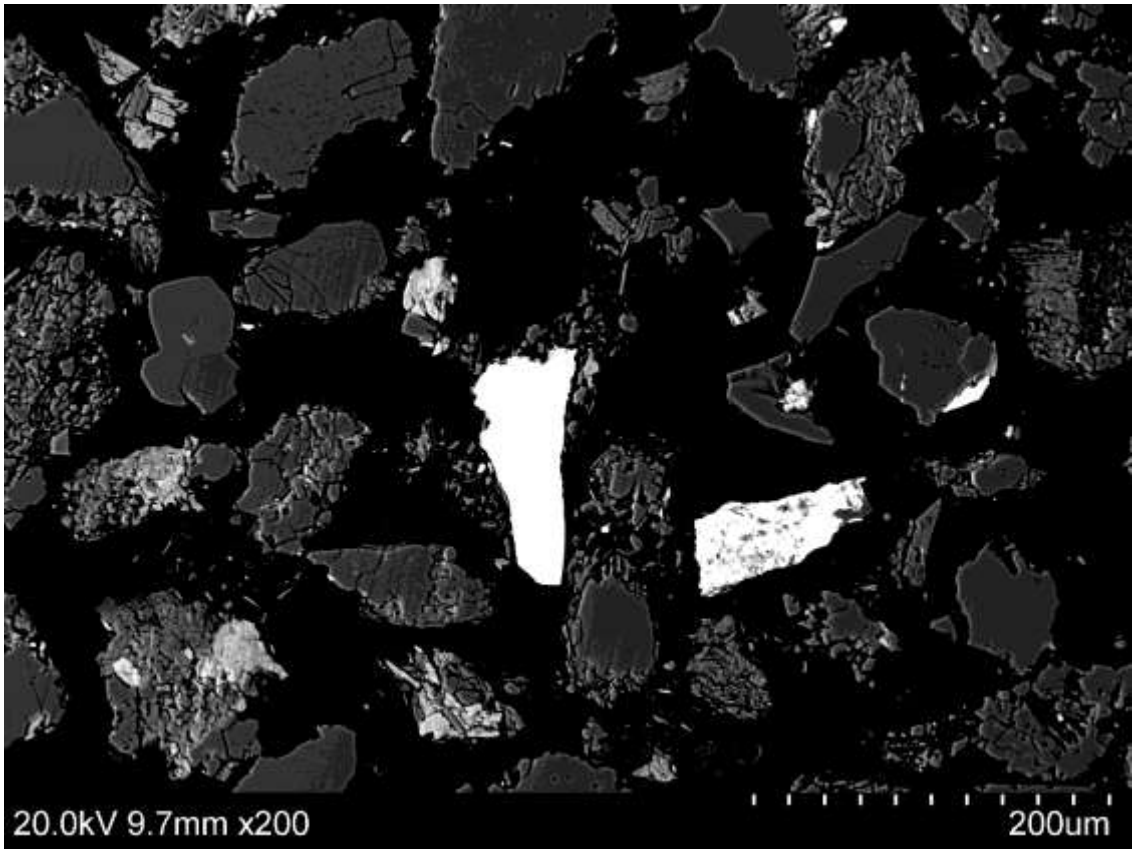

Figure 54. Half grain of Ferberite forming veins from the size fraction <0.125 mm, after a compression ratio of 20%, observed through SEM.

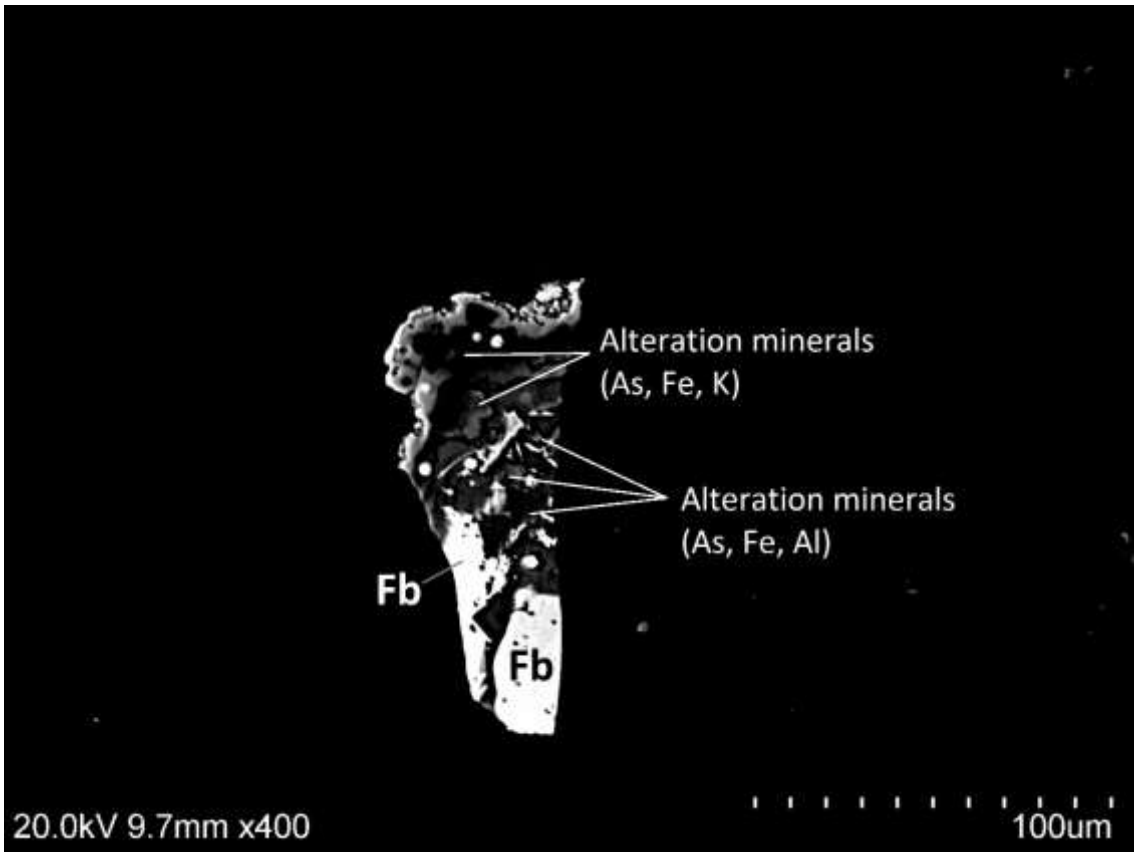

Figure 55. Half grain of Ferberite forming veins from the size fraction <0.125 mm, after a compression ratio of 20%, observed through SEM with mineral names and adjusted contrast and brightness to see clearly the dense minerals.

Figure 56. Half grain of Ferberite forming veins from the size fraction <0.5 mm, after a compression ratio of 20%, observed through SEM with adjusted contrast and brightness to see differences in density in the same grain.

In sample LP-29, where the material has been subjected to a compression ratio of 10% and has a particle size of 1-0.5 mm, there were no tungsten containing particles found.

In sample of a particle size range 0.25-0.125 and s/b of 10%., two different minerals containing the studied element were identified during the SEM. Figure 57 is a half grain of Ferberite in a circular shaped matrix of Quartz. The Ferberite phase is composed of different and separated small grains in the boundary of the particle. It is next to a particle of Muscovite where its laminar structure can be truly appreciated, the cracks are developed longitudinally along the elongated crystals.

Finally, Figures 58 and 59 show the only composite particle containing Scheelite found in this mineralogical characterisation. There are three tiny grains in a matrix of Muscovite. The gangue appear to be highly fragmented.

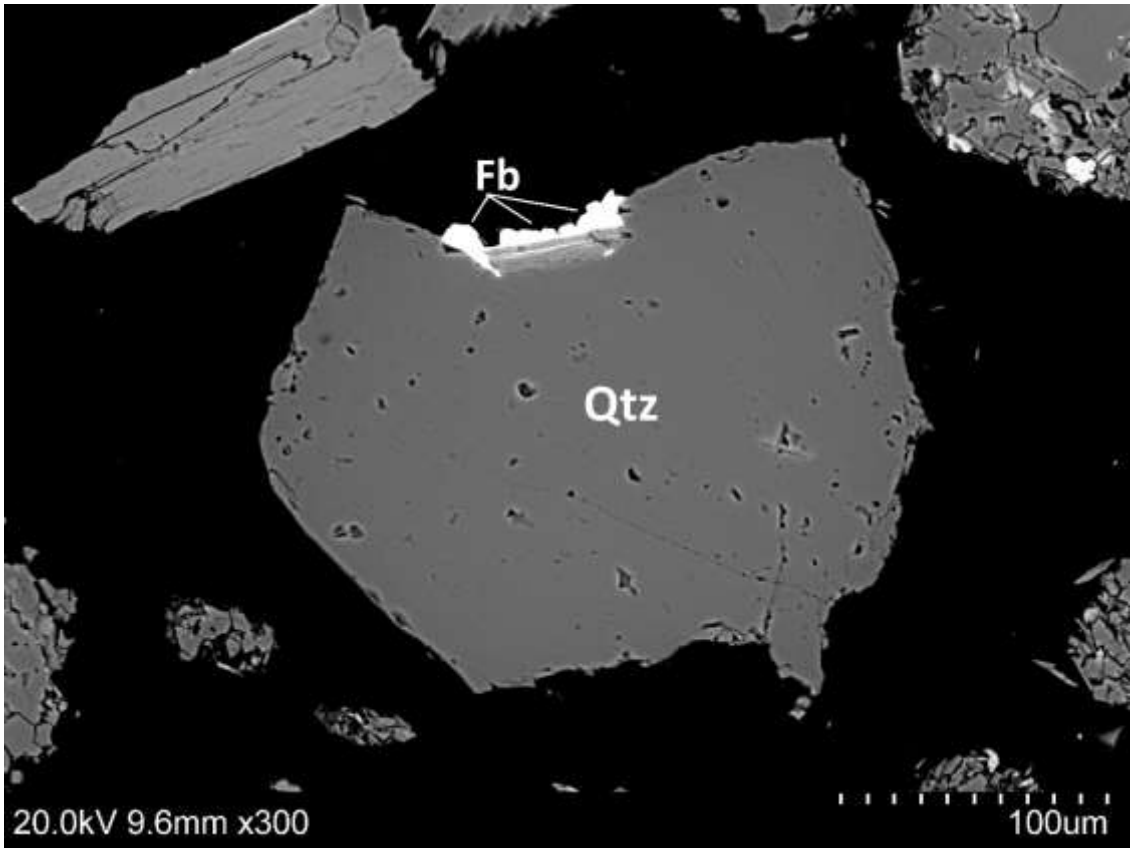

Figure 57. Half grain of Ferberite from the size fraction <0.25 mm, after a compression ratio of 10%, observed through SEM with mineral names.

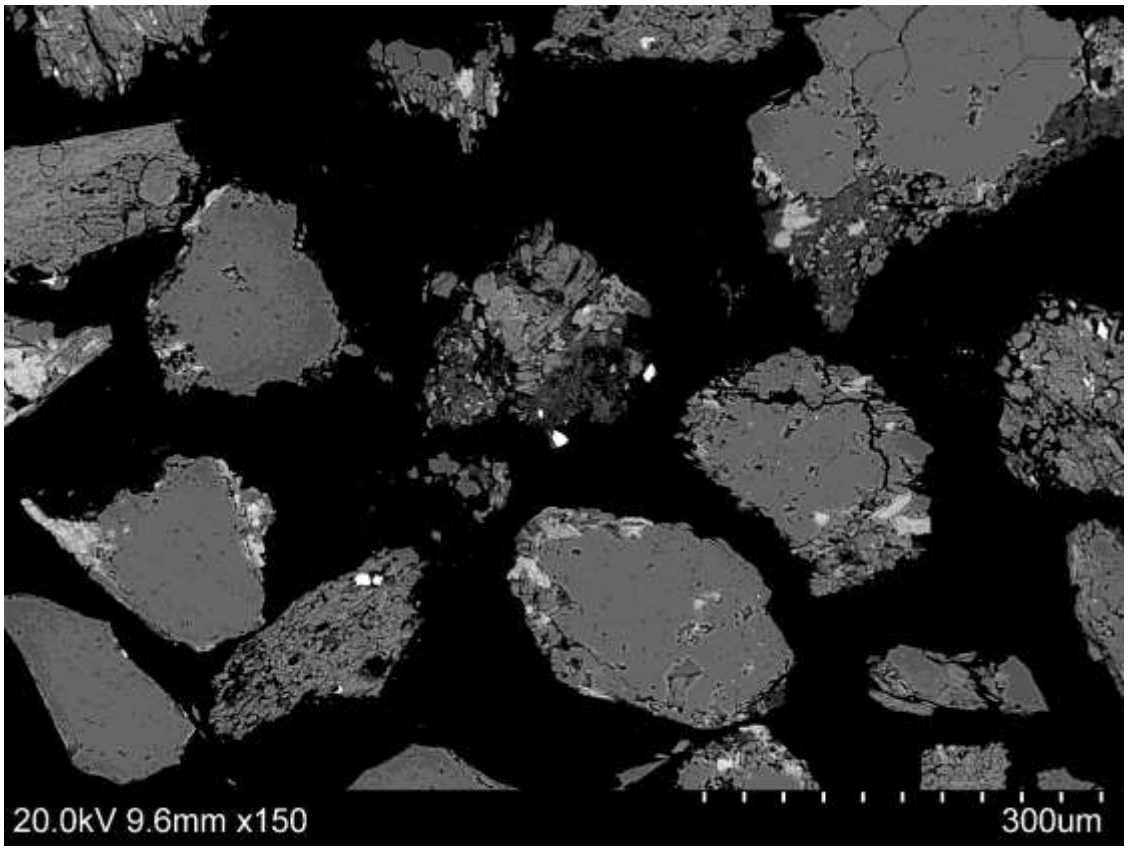

Figure 58. Half grain of Scheelite from the size fraction <0.25 mm, after a compression ratio of 10%, observed through SEM.

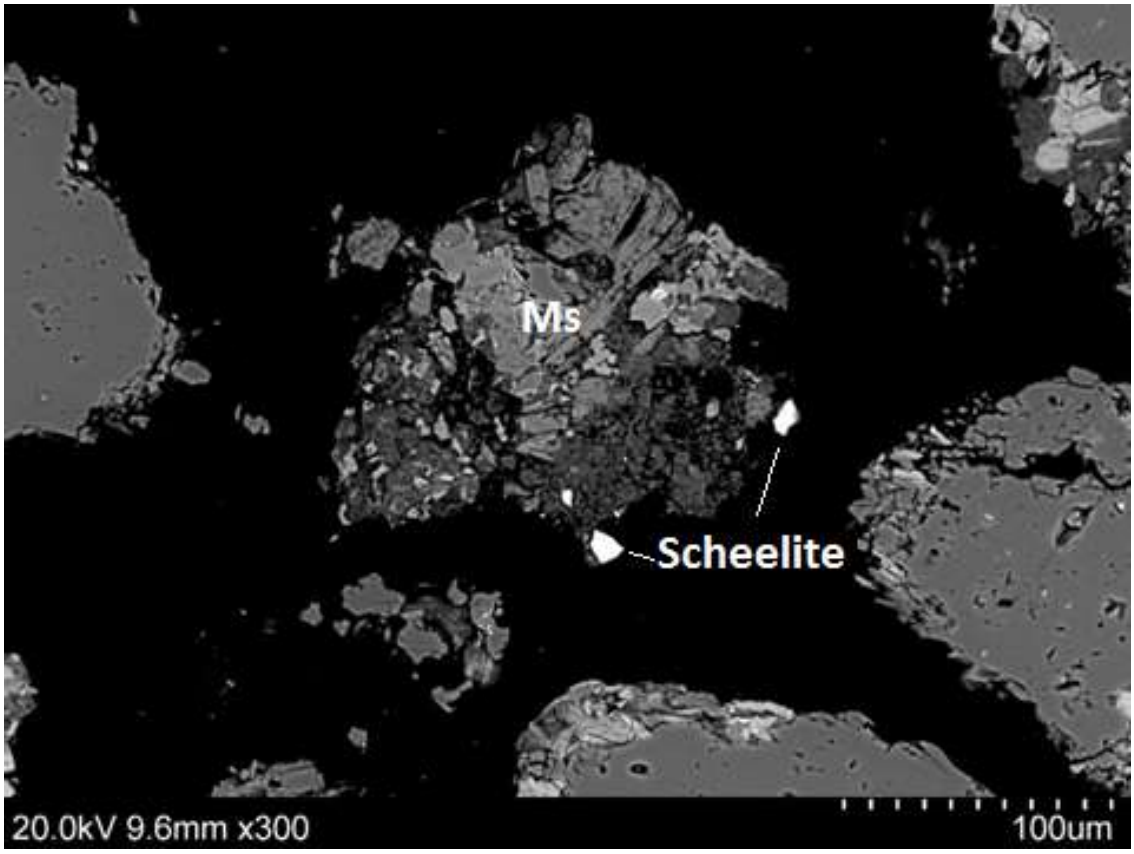

Figure 59. Half grain of Scheelite from the size fraction <0.25 mm, after a compression ratio of 10%, observed through SEM with mineral names.

Image analysis

In this section we are going to take an extended view of the representatively of the results obtained from the image analysis of the samples. In order to provide a clear and comprehensive value of the results, some examples, comparisons, figures and tables are included.

The representatively of the results presented below can be compared to the following methods of image analysis: SEM, petrographic microscope, optical microscope, and even MLA (Mineral Liberation Analysis).

Although, these methods are widely used and give clear information of the sought mineral from the samples, it is important to say that in this kind of analysis representativeness must be assessed. That is to say, in the case the concentration of the mineral is really low; there is the chance that no concentration of the mineral exists in the used sample. Performing image analysis in this sample will result in the wrong conclusion that no mineral exists at all. Furthermore, if one considers the coarse particle size range, such as 4-11.2 mm, this analysis gives a high probability that none ore particles are in the samples evaluated and, as a consequence, the result will be the same as before; no mineral is present.

In addition to the representativeness, it must be assessed that this kind of methods only analyses the surface of the sample, namely, 2D dimension. This fact makes image analysis more difficult to be representative.

Therefore, a huge amount of samples should be analysed to ensure a representative result of the reality of the mixture.

In Table 13 the concentration of tungsten for each particle size, including the whole rock, is shown. Taking the assumption that the entirety of the tungsten ore is Scheelite, the concertation of Scheelite is shown. To be capable of representing these low values, knowing the density of Scheelite (6.01g/cm^3) and Quartz (2.62g/cm^3) the volume fraction of Scheelite has been calculated. Being the sample the total volume of 100%, the maximum volume of scheelite seen in these samples with these analyses is only 0.019% whiles the minimum is 0.008% (as shown in the table below). If we refer to two dimensions now, instead of three, the proportion of Scheelite per unit area will be equivalent to the proportion per unit volume calculated below.

Table 13. Area fraction of tungsten mineral for each particle size range and the analysed W concentration, if there is only Scheelite as tungsten ore.

Compression ratio [%]	Size fraction [mm]	W concentration [ppm]	W concentration [%]	Scheelite concentration [%] (g Scheelite/g total)	Quartz concentration Scheelite [%] (g Quartz/g total)	Scheelite mixture density (g total/cm3 total)	Scheelite unit volume (cm3 Scheelite/cm3 total)	Quartz unit volume (cm3 Quartz/cm3 total)	Scheelite unit volume, over 100%	Quartz unit volume, over 100%	Scheelite + Quartz
20	11.2	113	0.0113	0.0177	99.982	2.6206	0.0077	100.0052	0.008	99.992	100.00
20	8	146	0.0146	0.0229	99.977	2.6208	0.0100	100.0067	0.010	99.990	100.00
20	5.6	164	0.0164	0.0257	99.974	2.6209	0.0112	100.0075	0.011	99.989	100.00
20	4	138	0.0138	0.0216	99.978	2.6207	0.0094	100.0063	0.009	99.991	100.00
20	2	116	0.0116	0.0182	99.982	2.6206	0.0079	100.0053	0.008	99.992	100.00
20	1	153	0.0153	0.0240	99.976	2.6208	0.0104	100.0070	0.010	99.990	100.00
20	0.5	185	0.0185	0.0290	99.971	2.6210	0.0126	100.0085	0.013	99.987	100.00
20	0.25	196	0.0196	0.0307	99.969	2.6210	0.0134	100.0090	0.013	99.987	100.00
20	0.125	185	0.0185	0.0290	99.971	2.6210	0.0126	100.0085	0.013	99.987	100.00
20	0.063	213	0.0213	0.0334	99.967	2.6211	0.0145	100.0098	0.015	99.985	100.00
20	0	277	0.0277	0.0434	99.957	2.6215	0.0189	100.0127	0.019	99.981	100.00
Uncrushed rock sample		253	0.0253	0.0396	99.960	2.6213	0.0173	100.0116	0.017	99.983	100.00

To understand the extent of the results obtained are, Figure 60 is shown. In the figure below, the surface of the sample section is represented, being considered 100% of the area, for each size fraction the area of the correspondent concentration of Scheelite (as the small blue circle in the centre). Furthermore, a patron representing particles of material with the size of each size fraction is illustrated in brown, in order to compare the area of Scheelite that theoretically should have been found in the sample section with the particle size.

The samples used in these analyses have a diameter of 2.4 cm. So, the area of these samples is 4.524 cm^2. Furthermore, if we consider the area of this sample occupied by Scheelite we can calculate the radius of a theoretical Scheelite particle. This process has been applied to all the size fractions of the table above and has been represented in Figure 60.

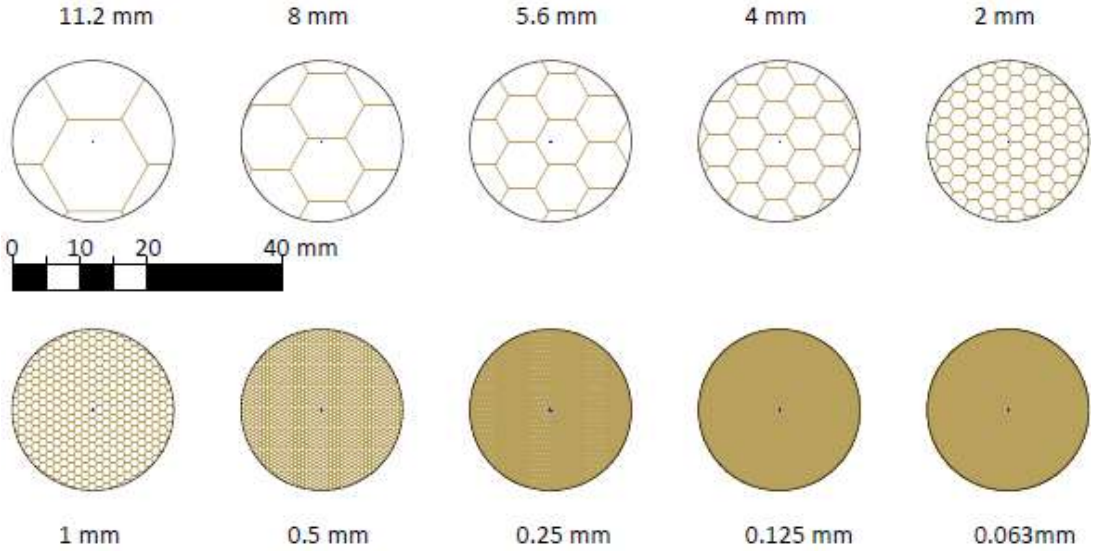

Figure 60. Comparison of the tungsten ore presence in each particle size fraction and the polished sections used in SEM.

To be more explicit about the concentration of Scheelite obtained, the question now is: if we know the value of the area from the concentration of Scheelite, we can know how many samples of 2.4 cm of diameter we will need in order to have a Scheelite particle similar in size to the particle size range for each size fraction, or an equivalent area divided in different particles (because there is low provability to find a liberated particle at coarse size). For example, for a size fraction of 0.25 mm, how many samples we need to have a particle of 0.25 mm of Scheelite, an equivalent area of Scheelite to a particle of 0.25 mm? In this case, the answer is 82 samples. For the remaining size fractions the values are shown in Table 14.

Table 14. Number of samples necessary to obtain Scheelite of the size fraction indicated.

Size fraction [mm]	Nº samples
11.2	282255
8	111455
5.6	48618
4	29479
2	8768
1	1662
0.5	344
0.25	82
0.125	22
0.063	5

As it has been done above, in the following Tables 15 and 16 it is shown the results of this calculus for the Ferberite, instead of Scheelite. In this case, Ferberite is denser than Scheelite, therefore the area fraction of it will be even lower than before. The maximum value of Ferberite concentration is 0.0458% with a 0.016% from the total volume of the sample and the value of 0.0187% is the minimum with a 0.007% from the total volume of the sample.

Table 15. Area fraction of tungsten mineral for each particle size range and the analysed W concentration, if there is only Ferberite as tungsten ore.

Compression ratio [%]	Size fraction [mm]	W concentration [ppm]	W concentration [%]	Ferberite concentration [%] (g Ferberite/g total)	Quartz concentration Ferberite [%] (g Quartz/g total)	Ferberite mixture density (g total/cm3 total)	Ferberite unit volume (cm3 Ferberite/cm3 total)	Quartz unit volume (cm3 Quartz/cm3 total)	Ferberite unit volume, over 100%	Quartz unit volume, over 100%	Ferberite + Quartz
20	11.2	113	0.0113	0.0187	99.9813	2.6209	0.0066	100.0157	0.007	99.993	100.00
20	8	146	0.0146	0.0241	99.9759	2.6212	0.0085	100.0203	0.008	99.992	100.00
20	5.6	164	0.0164	0.0271	99.9729	2.6213	0.0095	100.0228	0.010	99.990	100.00
20	4	138	0.0138	0.0228	99.9772	2.6211	0.0080	100.0192	0.008	99.992	100.00
20	2	116	0.0116	0.0192	99.9808	2.6209	0.0067	100.0162	0.007	99.993	100.00
20	1	153	0.0153	0.0253	99.9747	2.6212	0.0089	100.0213	0.009	99.991	100.00
20	0.5	185	0.0185	0.0306	99.9694	2.6215	0.0108	100.0258	0.011	99.989	100.00
20	0.25	196	0.0196	0.0324	99.9676	2.6216	0.0114	100.0273	0.011	99.989	100.00
20	0.125	185	0.0185	0.0306	99.9694	2.6215	0.0108	100.0258	0.011	99.989	100.00
20	0.063	213	0.0213	0.0352	99.9648	2.6217	0.0124	100.0297	0.012	99.988	100.00
20	0	277	0.0277	0.0458	99.9542	2.6222	0.0161	100.0386	0.016	99.984	100.00
Uncrushed rock sample		253	0.0253	0.0418	99.9582	2.6220	0.0147	100.0352	0.015	99.985	100.00

The figures presented for the case of Scheelite are not shown in this case because it would be redundant. However, the calculus of how many samples we will need in order to have a particle of Ferberite as big as the size fraction, or equivalent, is shown, in order to get some the order of magnitude of the values of the concentration obtained from the chemical analyses.

Table 16. Number of samples necessary to obtain Ferberite of the size fraction indicated.

Size fraction [mm]	Nº samples
11.2	331719
8	130986
5.6	57138
4	34645
2	10304
1	1953
0.5	404
0.25	95
0.125	25
0.063	6

Until this point the results from the mineral characterisation have been presented and commented, the presentation of results ends with this chapter. From this point forth, the author will analyse the results and try to draw conclusions.

6. Discussion of Results

6.1. IPB test. Particle Size Reduction

In Figures 14 and 15, can be clearly seen that when increasing the compression ratio the amount of breakage in each event increases. Hence, the size distribution from the 35% compression ratio will be finer than the 10% compression ratio after one event.

For each test series the sample material is subjected to a number of compression breakage 2-5 times. This is the reason that the final size distribution from the 35% compression ratio series is finer than the 25% compression ratio series. In the 35% of s/b series the material has been compressed 2 times, while in the 25% there were 4 repetitions. This can be seen in Figures 12 and 13. In each compression the sample will be further crushed, therefore, the PSD will be finer for each breakage event.

The size reduction in compressive crushing depend only on the compression ratio; however, the energy required to achieve this particle size reduction will vary depending on the strength of the rock. BENGTSSON, ET AL. (2015) made a comparison between a more competent sample and a reference sample, both of them were crushed with the same compression ratio, and the product had the same particle size distribution, whereas the energy needed for the same size reduction was more than the double for the competent rock.

As pointed out before, it can be noted that there are three accumulations of particles in the size ranges 0-0.063 mm, 1-4 mm and 5.6-11.2 mm by studying the frequency diagrams of particle size distribution, i.e. Figure 13, 16 and 18. The accumulation in these size ranges are present for all tests from 10 to 35% compression ratio, however for low compression ratio (10 and 15%) is much less prominent.

At low compression ratios a heterogeneous particle size distribution are generated; with a big fraction of coarse particles and low amount of fines. Right in the other hand, at medium and high compression ratio a semi-homogeneous particle size distribution is generated; where the peak in the coarse particles has disappeared, or is much less distinguished, and the mass has been distributed over the other fractions, specially generating accumulations in the size range 1-4 mm and smaller than 0.063mm.

When a particle breaks due to compressive crushing its products fall mainly into two size ranges:

- Coarse particles, as a consequence of a tensile stress breaking a particle into two or three big daughter particles of roughly half of the size than the former.

- Fines resulting from the breakage near the loading points.

The accumulations of particles mentioned above correspond to the predisposition of particles broken on account of compressive forces. The accumulation in the size range <0.063 mm is formed by the fines created in the contact area where load is applied. The accumulation in the size range 5.6-11.2 mm is composed by unbroken particles of particles that have been broken for the first time. Finally, the fact that for each compression series the samples are subjected to multiple compression events (from 2 to 5), cause that some particles that have been broken, and therefore reduced to a size of roughly half, may be broken again in posterior compression events, corresponding to the accumulation in the size range 1-4 mm.

It is interesting to point out how the force-pressure response behaves in a relatively stable manner of the series at low compression ratio (Figure 19). When there are still air pockets in the particle bed it allows point to point contact between larger particles. Whereas a sample that is reduced to size fine enough where it creates a packed bed with a certain elevated level of packing density, the force-pressure response will have a smooth exponential increase. This can be clearly observed in the force-displacement plot for the 25% compression ratio shown in Figure 61.

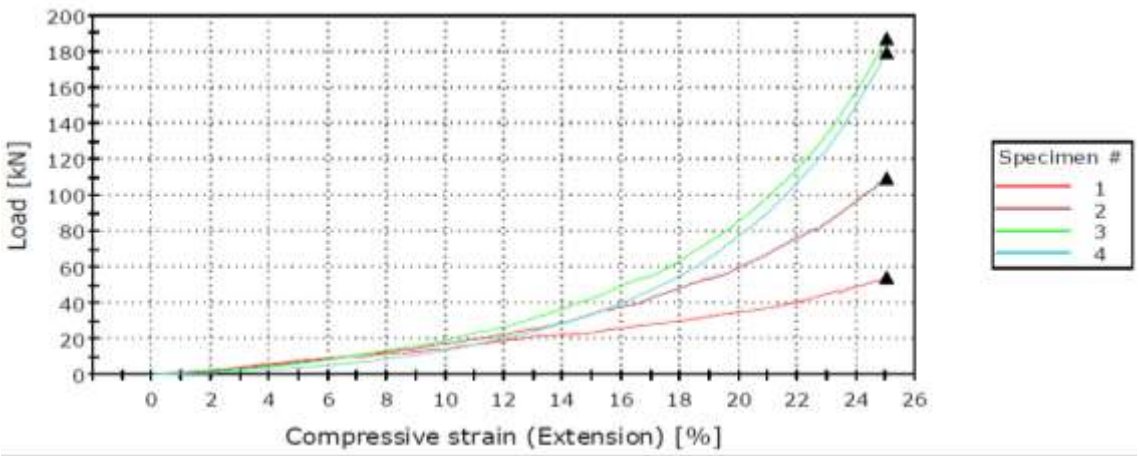

Figure 61. Force-displacement plot for the four compression tests of 25% compression ratio IPB.

The bigger the fraction of fines, the higher the packing density will be, hence the force-pressure exponential increase will be steeper. This fact can be noted when comparting Figures XXX, 61 and 62.

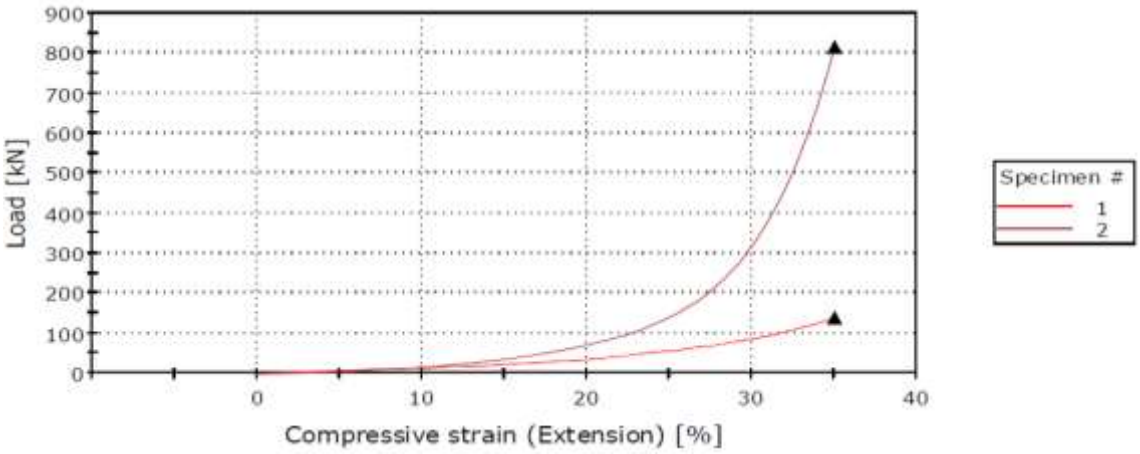

Figure 62. Force-displacement plot for the two compression tests of 35% compression ratio IPB.

At the point when a large quantity of fines have been produced in previous compressions of the same series, the particles that haven't been destroyed will be surrounded by fine particles. This will cause that a nearly isostatic pressure will be transmitted to each one of these coarse particle.

When the material sample was removed from the die in the last compression of the large compression ratio (25, 30 and 35), it was so compact it looked like a cylindrical brick, and there was difficulty in removing it. When subjecting such a compacted sample further at even high pressures it is possible to achieve micro-fracturing along grain boundaries (BENGTSSON, ET AL., 2015). It has been proved that such high pressure levels may increase mineral liberation.

Figure 63 proves that the energy utilised for the particle size reduction increases when the compression ratio also increases. However, as can be seen in Figure 63 the energy remains close to constant for each compression event for low compression ratios (10 and 15%), in contrast for medium and high compression ratios the energy does increase with the repetitive compression events, to the point than for 35% it has an exponential shape. The constant energy consumption for low compression ratios is explained by the remaining air pockets in the particle bed that help that the compression of the bed does not get increasingly difficult. The offset between the 10 and 15% of compression ratios can be explained because the 15% test has a longer duration, due to the constant loading rate of the hydraulic compression. An equivalent behaviour describes the compressive stress applied by the machine (Figure 64).

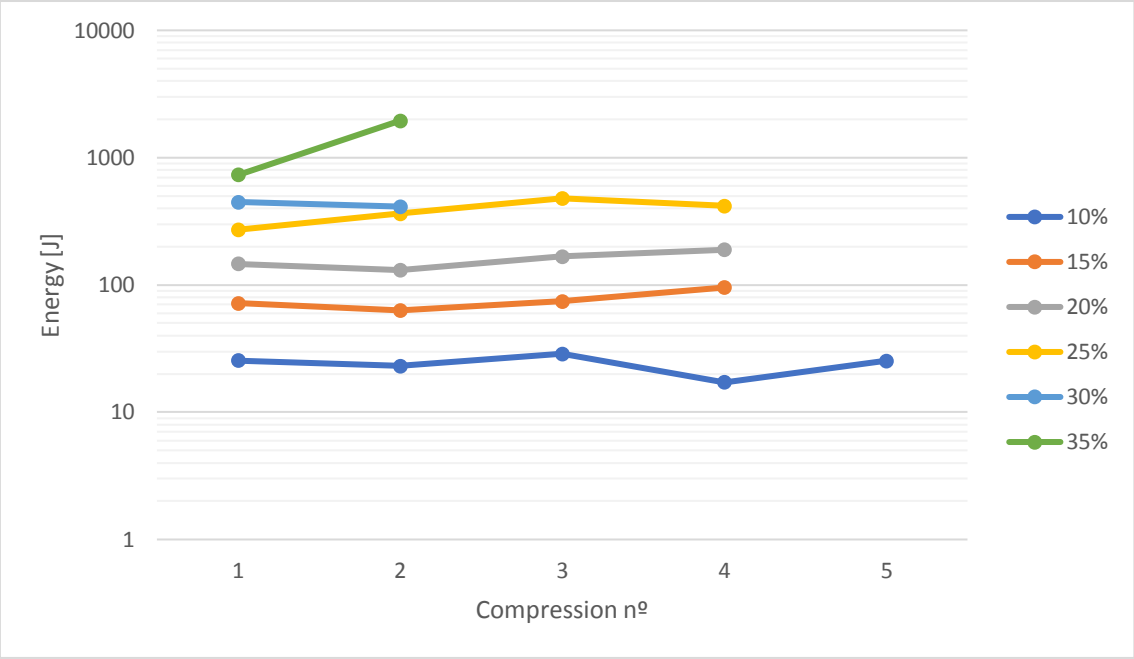

Figure 63. Energy utilized in each compression event for the different compression ratios tested.

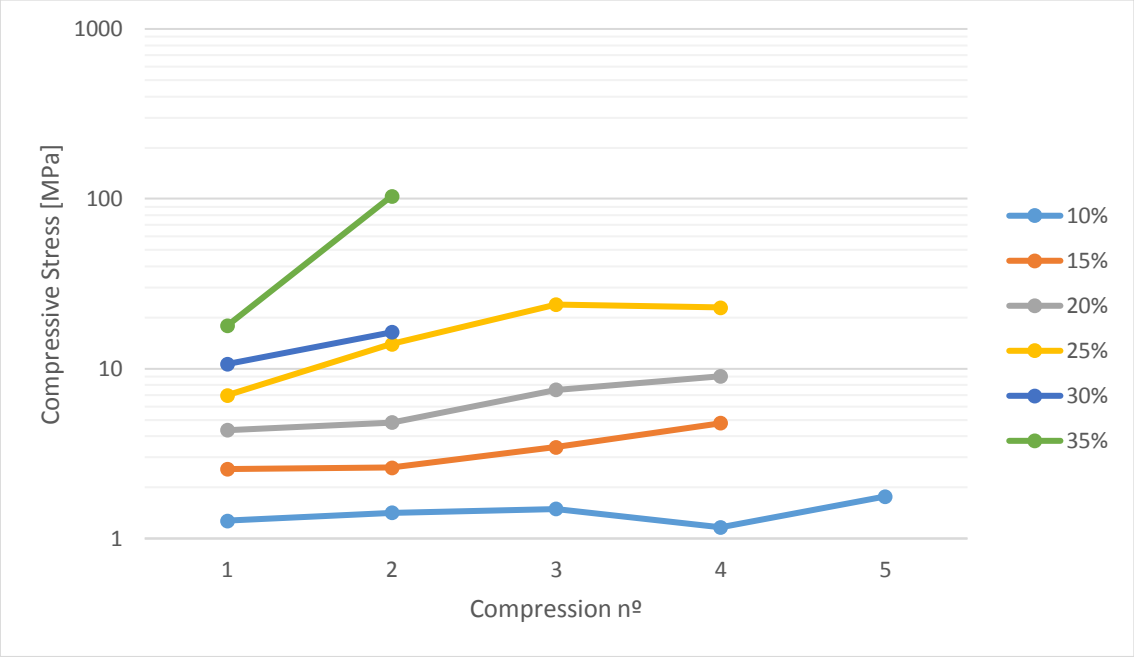

Figure 64. Compressive stress applied in each compression event for the different compression ratios tested.

The specific energy can easily be calculated knowing that each compression test is performed with 500 grams of material. It is shown in Figure 65.

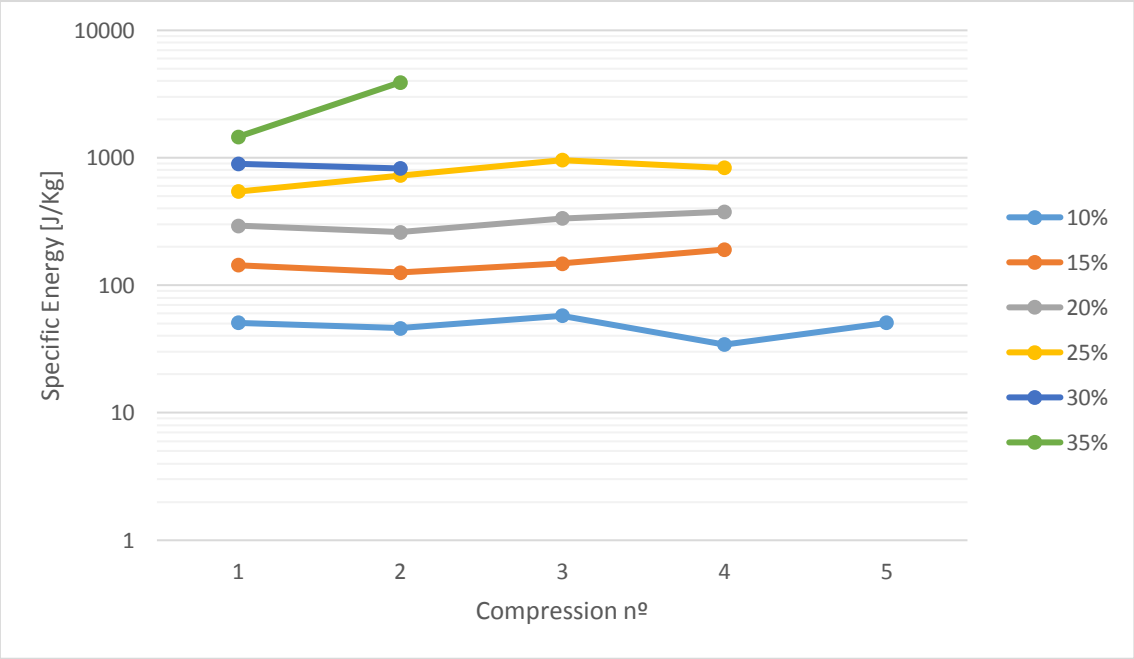

Figure 65. Specific energy for the breakage of the material in each compression event for the different s/b tested.

The specific energy for each size reduction event and the compressive stress are represented in Figure 66 for the first compression in each compression ratio series. It is noteworthy the mention of the extremely perfect exponential trend curve that both parameters follow. The higher the compression ratio is, the higher the specific energy and the compressive stress will be; it is not strange that the same trend curve works for both, since they are two related parameters.

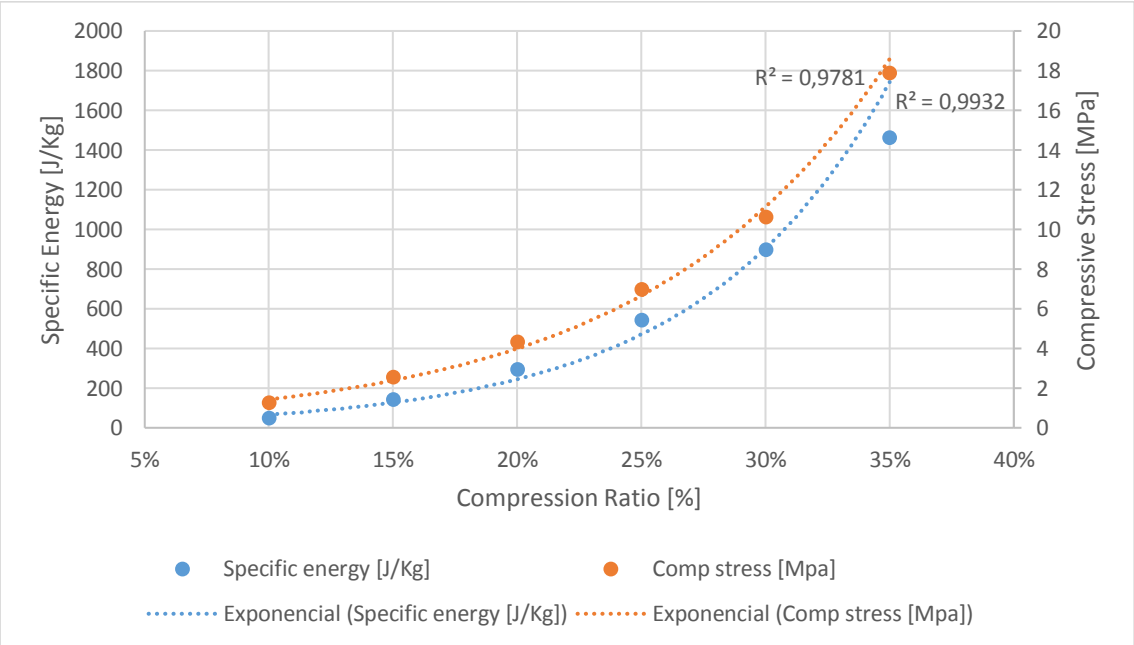

Figure 66. First compression of each compression rate series with the specific energy used and the compressive stress.

6.2. Bond Work Index and utilised energy

This method of backcalculating W_i from the measured energy, instead of doing it the other way around by calculating the energy used from the measured W_i has not been found in the literature, however, science sometimes is try and failure, since the data is available it is worth the effort of trying.

Note that the real energy used in the breakage is used for the calculous, not the energy consumption of the compressive crushed.

Results for the Bond Work Index were calculated using the energy utilized in the compressive crushing, that was previously measured automatically by the software operation the hydraulic compression. They are shown in Table 8.

Theoretically, these results should be equal. In the practice it is expected that they have some differences for the different size reductions, however, always remaining in a constant range. For the studied case, results for Bond Work Index go from 11.1 up to 51.0 kWh/t, they are not even close to being constant or have little differences. Although maybe there is an existing correlation with other parameters of the equation that explains this big variations. For this reason in Figures 24-27 it is represented graphically the relation of W_i with any other parameter used in the calculation.

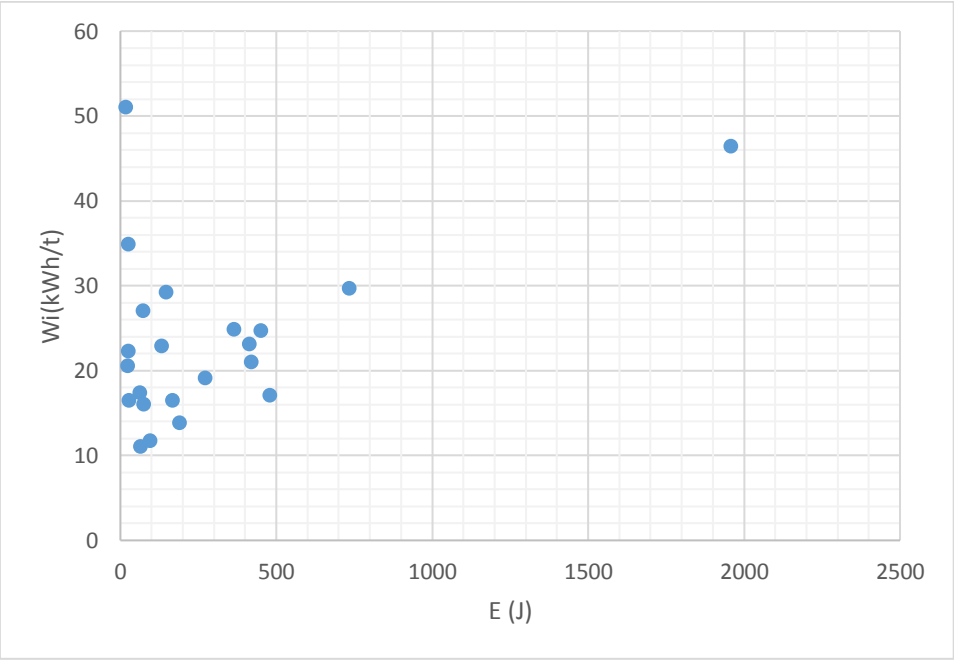

Figure 67. Bond Work Index represented against energy utilised for the particle size reduction.

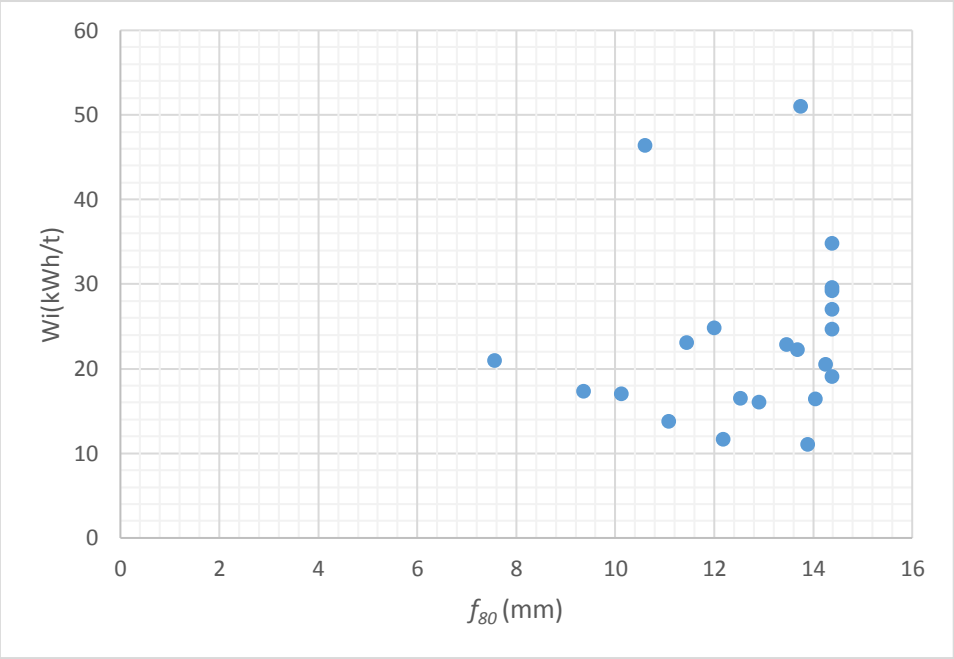

Figure 68. Bond Work Index represented against the feed size.

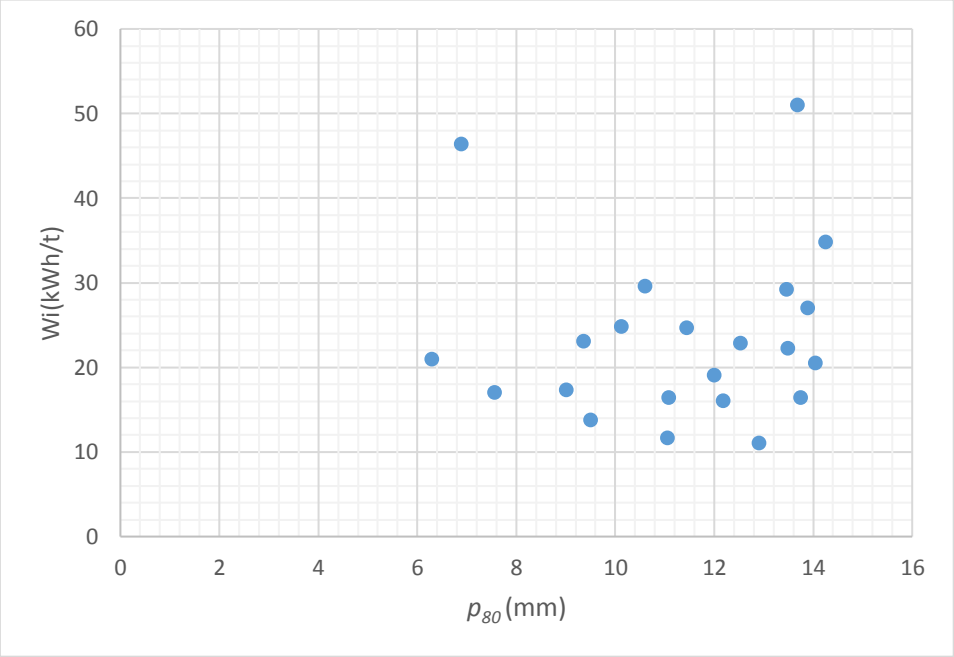

Figure 69. Bond Work Index represented against the product size.

W_i has been tried to be linked to energy utilised, to the product size, to the feed size or even to the relation of size reduction that occurred for each compressive breakage test (Figures 67-70). As can be seen above, all of these graphs just look like a cloud of points. Denying that anything relates Bond Work Index with any other parameter.

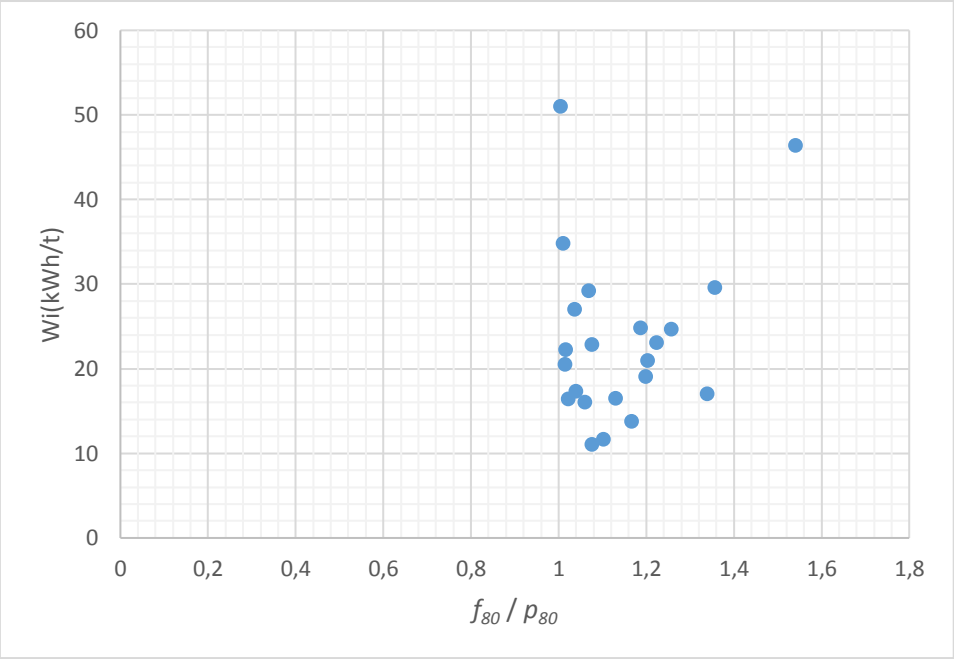

Figure 70. Bond Work Index represented against the relation of reduction of the particles.

The main reason that this trial did not work it that when Bond Work Index is measured, the procedure followed for it is standardised, either by Bond Rod Mill Test or Bond Ball Mill Test or by Bond Impact Pendulum Test. All of them follow a step by step system where energy utilised, energy losses and any other influential factor are controlled, and most important they are always carried out under the same circumstances.

The piston and die apply a certain measured force but the energy losses due to friction or heat loss, also the compacting density of the material is not the same in all cases. All these, are factors that distance the experimental work carried out with the standardized tests for the calculation of Bond Work Index. Since an infinite number of different particle size distributions pass the single points of f_{80} and p_{80}, neither of the parameters can characterise an entire size distribution, it lacks of precision in describing the shape of a PSD (EVERTSSON, 1995).

Besides, the standardised Bond Tests are for abrasive crushing for rod and ball mill and for impact crushing for Bond's pendulum, no test for the determination of Bond Work Index for compressive crushing has been developed.

Conclusively, this manner of calculating the energy index in reverse, starting from the utilised energy, than it is done with Bond tests does not work. It would have been truly interesting that similar number would have been obtained, or that they would show any kind of tendency. Sadly it has not been like this, but as it is said: sometimes science is try and failure.

6.3. Size Distribution Modelling

Taking into account the results obtained from the compressive breakage tests, and considering that the breakage behaviour of the material only depends on the compression ratio (s/b), it is feasible to calibrate the breakage function.

The predicted PSD for the IPB test results is represented in Figure 22, where it is compared to the real particle size distribution obtained, from the tests, as a function of the compression ratio. The red plot represents the simulated particle size distribution results and the blue plot represents the results obtained from the test data.

Observing the high accuracy of the simulation compared to the real results it can be stated that the calibrated breakage behaviour model, initially developed by EVERTSSON (1997, 1999 and 2000), can be used in further simulations of repeated size reductions in a compressive crusher machine.

IPB test procedure is used to describe the breakage behaviour of one of the two modes that happen in a compressive crusher. Then the results are represented by a mathematical description of how the particle breaks, and it is introduced to a machine model. By combining breakage with a flow model a model that describes a crusher is obtained, it can be any crusher that uses the described breakage mode. From this point the research would be focused on finding the better functioning of the crusher for the studied material.

HPGRs, even though that sometimes is classified in the grinding group in reality is a crusher, does only one interparticle breakage to a fixed compression ratio. It is one of the simplest crusher to model using this methodology. Could also a cone crusher be modelled, which is a rotational symmetry crusher that compresses several times using different compression ratios, for example.

LEE (2012) developed a model that, using the breakage behaviour model of a certain material as an input, gave as an output the optimal number of compressions and the compression ratio of each of those events that would optimise the breakage of the studied material from a specific feed size range to a wanted product size range. The same author developed another model where using the same inputs described above gives the optimal number of compressions and the compression ratio of each of those events that would optimise the energy consumption for the breakage of the material as a result. The design of a compression crusher for a certain studied material can be done using the data obtained from these models. It is a different approach to optimization, optimizing at the source.

6.4. W grade according to the PSD

In Figure 23 the concentration of tungsten is represented graphically. As it has been commented before, a slight correlation can be seen between W concentration and particle size. However, this correlation is not strong, as can be seen in Figure 71, the best fitting regression curve is an exponential. The coefficient of determination that determines the proportion of the variance in the dependent variable that is predictable from the independent variable, determines how good the correlation is. For this case it is only of 0.50 meaning the correlation merely fits.

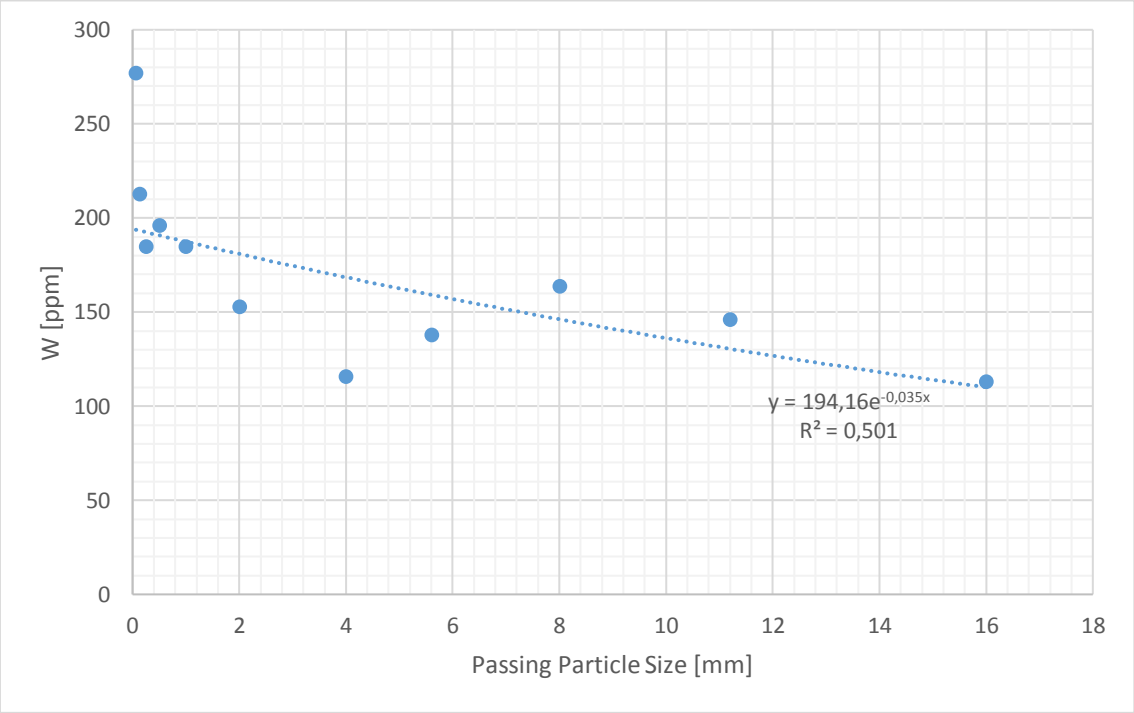

Figure 71. Tungsten concentration in ppm in each size fraction of 20% of s/b with a linear trend line.

Bigger particles are considered to be unpredictable, for coarser particle than 4mm the concentration of tungsten does not follow a visible pattern. A relatively accurate correlation fits the remaining data (Figures 72 and 73), creating a proportionally inverse trend that relates particle size and tungsten fraction for small particle size.

In Figure 72 a linear trend line has been represented using all the data from Table 10 with a particle size smaller than 4 mm. The coefficient of determination for this trend line is R^2= 0.70, this is an acceptable value. However, in Figure 73 a better regression curve was calculated, an exponential curve with an R^2 value of 0.86. We can say that this trend line correlates the obtained data well. So that an inversely proportional exponential correlation links the concentration of tungsten in the small particle size range (from 4 mm).

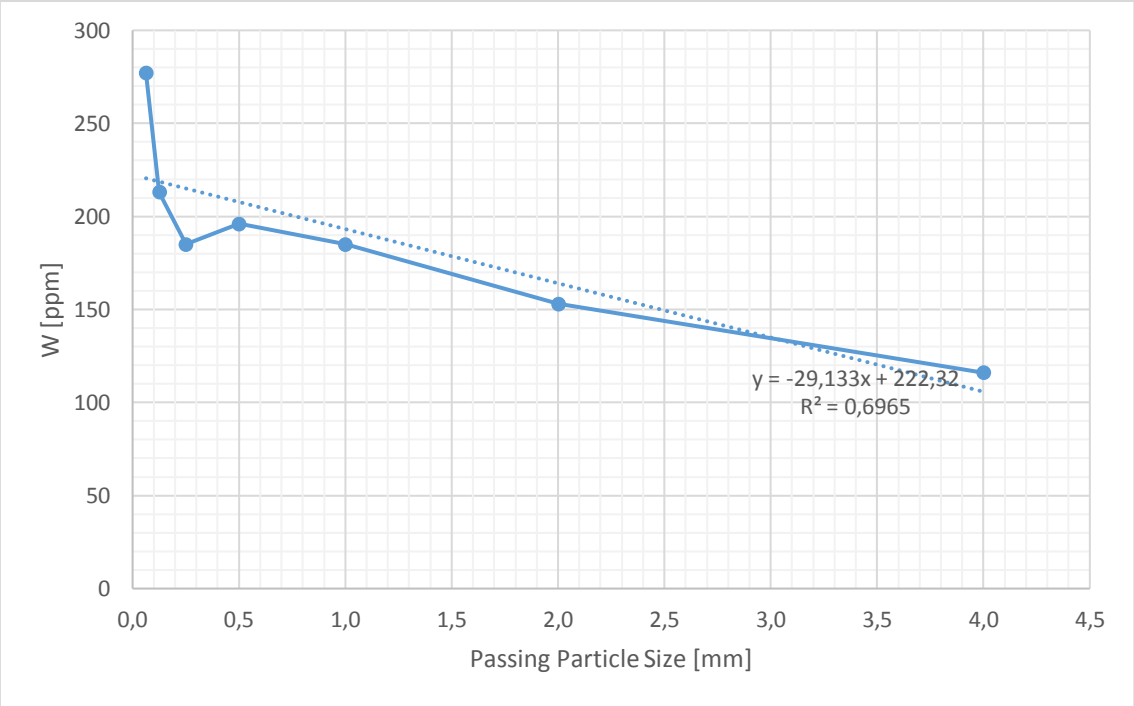

Figure 72. Tungsten concentration in ppm for size fraction smaller than 4 mm and 20% of s/b with a linear trend line.

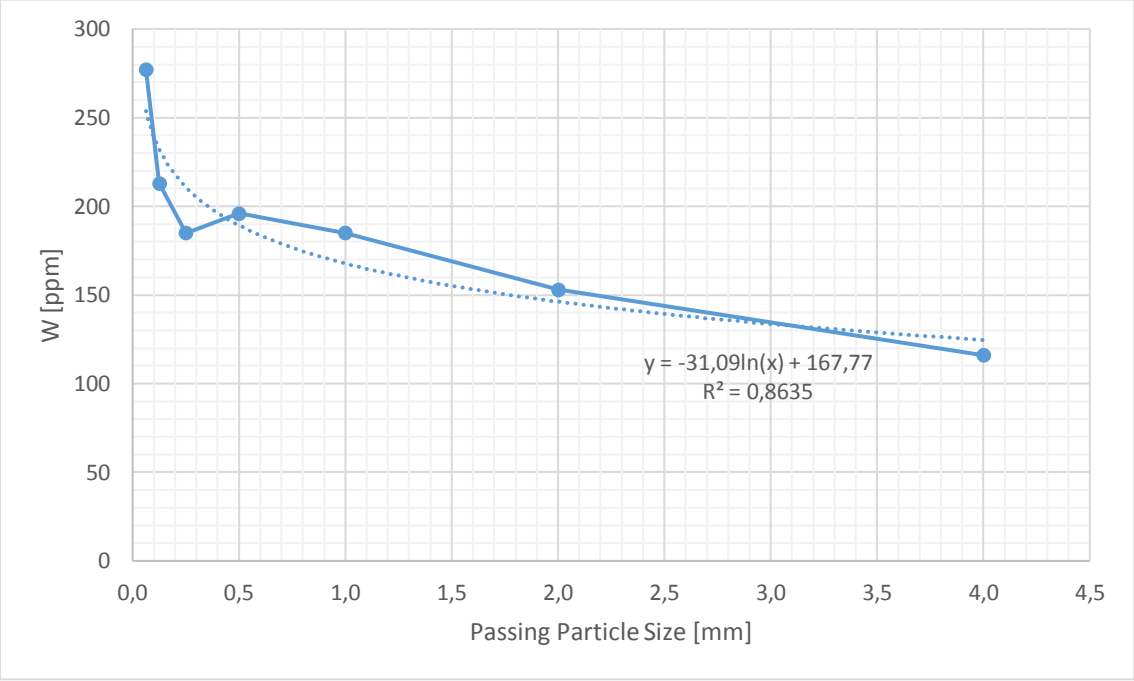

Figure 73. Tungsten concentration in ppm for size fraction smaller than 4 mm and 20% of s/b with an exponential trend curve.

As it has been explained in Chapter 5.5. in the material used in this research contains two different tungsten ores: Scheelite and Ferberite. Scheelite contains calcium as well as tungsten in its chemical structure. In Table 9 the concentration of calcium oxide (CaO) is shown, from this the concentration on calcium can be easily deduced using the atomic weight of calcium and oxygen. From the X-Ray Diffraction analysis no other mineral with a relatively high concentration of calcium (>1%) in its structure has been detected.

Taking the hypothesis that all the calcium in the material is forming Scheelite and knowing the concentration of calcium in the whole rock and that the chemical formula of Scheelite is $CaWO_4$, the maximum possible amount of Scheelite (given the amount of Ca) in the sample can be calculated, called maximum Scheelite due to Ca.

Then using the concentration of tungsten and assuming the hypothesis that all the tungsten in the sample is forming Scheelite (Table 10), the maximum possible amount of Scheelite (given the amount of W) in the material can be calculated, called maximum Scheelite due to W.

If maximum Scheelite due to W is bigger than maximum Scheelite due to Ca, the maximum amount of Scheelite can be know and hence the minimum amount of Ferberite. This would be useful to have a rough idea of the representation of each on these two tungsten minerals in the ore.

Unfortunately, in this case, even though the concentration of calcium is really low, it is too large for the existing amount of tungsten, making it impossible to reach said approximation. This means that there must be some low concentration mineral containing calcium in its chemical formula. Therefore, the fraction of Scheelite and Ferberite over the total remains unknown.

6.5. Evolution of mineralogy with the PSD

In Chapter 5.5. the mineralogical composition, measured with the XRD semi-quantitative method, of the material in question is shown for the whole particle size range of 20% of compression ratio and for three separate size fractions of 10 and 30% of s/b. In this chapter those results will be discussed, together with the results obtained from the SEM-EDS qualitative method of the observed samples.

In Table 12, the concentration of each mineral present in the sample (with a concentration higher than 1%) is shown. Table 17 represents the data from Table 12 for the compression ratio of 20%, in order to see if any relation links the concentration of the main minerals depending on the size fraction for the same s/b. It helps have a general understanding of how the mineralogy varies through the different compression ratios.

Table 17.Mineralogical composition of all the size fractions for a 20% of s/b

Sample	Passing size	s/b	Quartz	Muscovite	Dravite	Cassiterite	Kaolinite	Petalite
LP-12	16	20%	59%	38%	2%	1%	0%	0%
LP-13	11,2	20%	54%	38%	7%	0%	0%	1%
LP-14	8	20%	56%	41%	3%	0%	0%	0%
LP-15	5,6	20%	57%	40%	3%	0%	0%	0%
LP-16	4	20%	65%	31%	4%	0%	0%	0%
LP-17	2	20%	60%	36%	3%	1%	0%	0%
LP-18	1	20%	52%	45%	3%	0%	0%	0%
LP-19	0,5	20%	55%	42%	3%	0%	0%	0%
LP-20	0,25	20%	52%	44%	2%	0%	2%	0%
LP-21	0,125	20%	58%	39%	3%	0%	0%	0%
LP-22	0,063	20%	48%	47%	5%	0%	0%	0%

At a glance, no correlation is appreciated with none of the two main minerals in the material. However, what is easy to recognise is that when Quartz content increases, Muscovite content decreases and vice versa. This is normal due to the fact that, besides of these two minerals, the remaining minerals are almost insignificant in concentration, Dravite is also considered below.

To see if there is any proper correlation Figures 75, 76 and 77 represent the concentration of Quartz, Muscovite and Dravite, respectively, in a linear scale. Seeing Figures 75, 76 and 77, we can say that the only word that appears to describe the concentration distributions of these three minerals along the different particle size ranges is random. The results obtained from the X-Ray Diffraction of crystal dust show that there is no apparent correlation between the particle size and the concentration in the rock material of Quartz, Muscovite and Dravite, or in fact any other mineral phase existent in the rock.

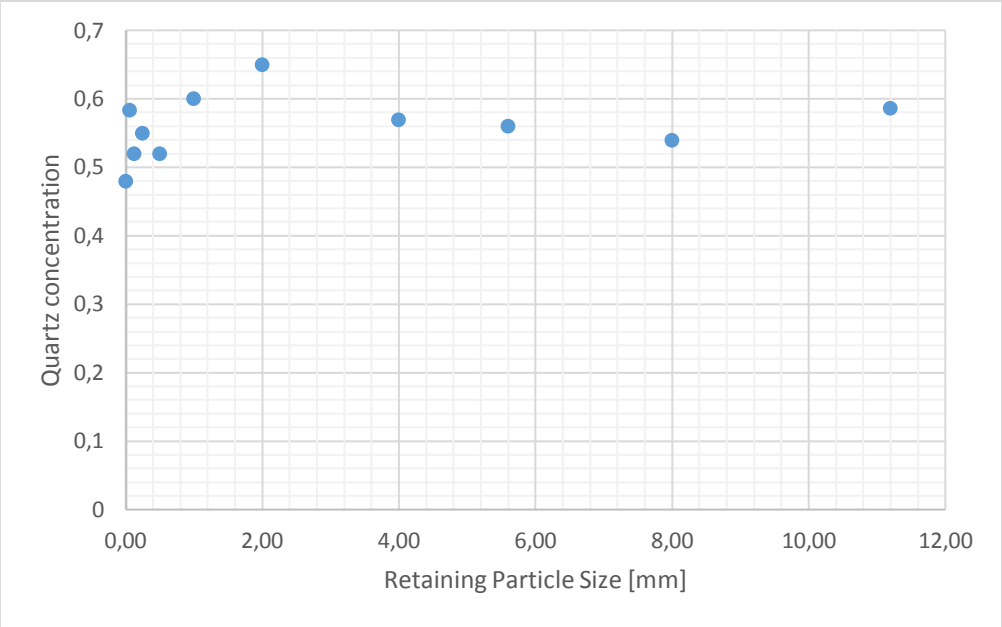

Figure 74. Quartz concentration in each size fraction for a 20% of s/b

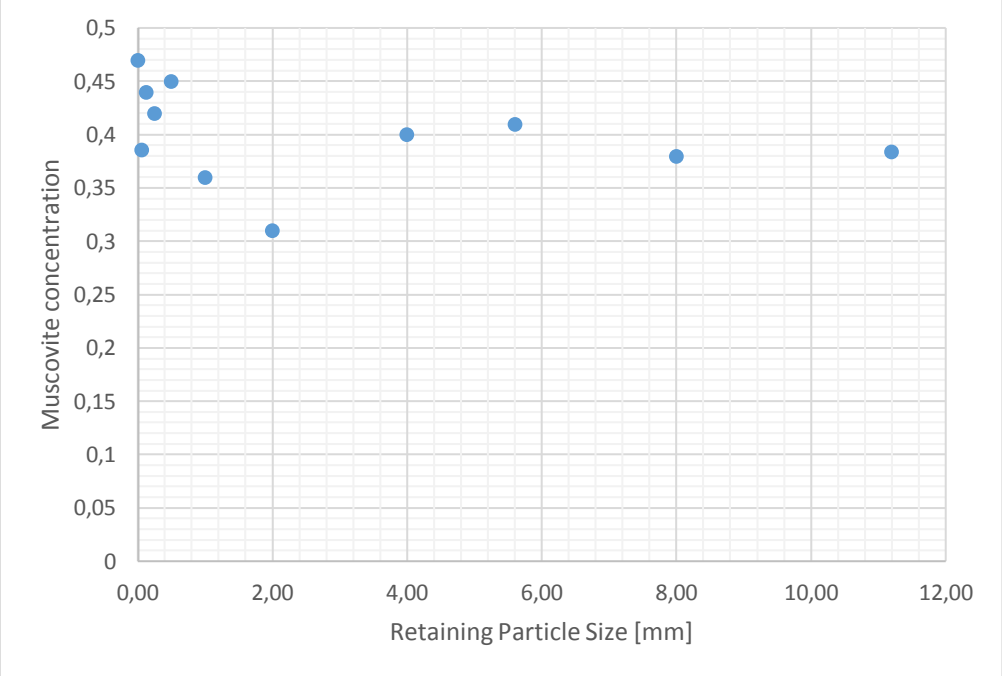

Figure 75. Muscovite concentration in each size fraction for a 20% of s/b

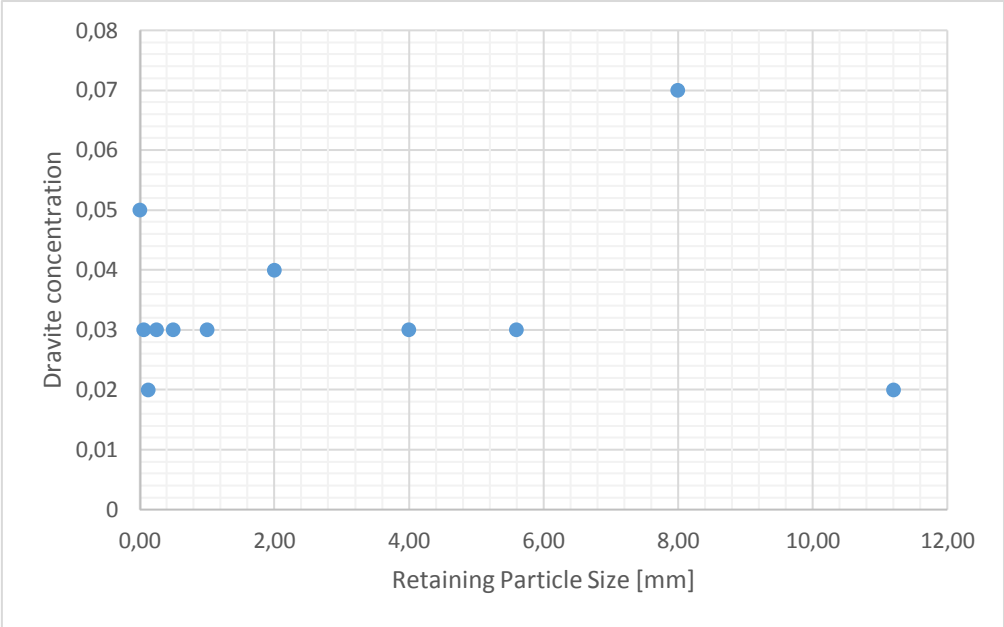

Figure 76. Dravite concentration in each size fraction for a 20% of s/b

Relations between different particle sizes and mineral concentrations using the compression ratios of 10 and 30% were also investigated and the result is the same as before, no apparent correlation exists.

The other option is if the mineralogical composition changes depending on the compression ratio, but not on the particle size. Figures 78, 79 and 80 are aimed to the evaluation of such relation.

In Figure 78 the mineralogical concentration of Quartz, Muscovite and Dravite in the particle size in the range of 16-11.2 mm is represented depending on the compression ratio for the values of 10, 20 and 30%. The fraction of Quartz is high for 10%, decreases for 20 and increases again for 30%. Muscovite has the opposite behaviour as Quartz, is low for 10, increases for 20 and decreases for 30%. Dravite has a similar behaviour than Quartz.

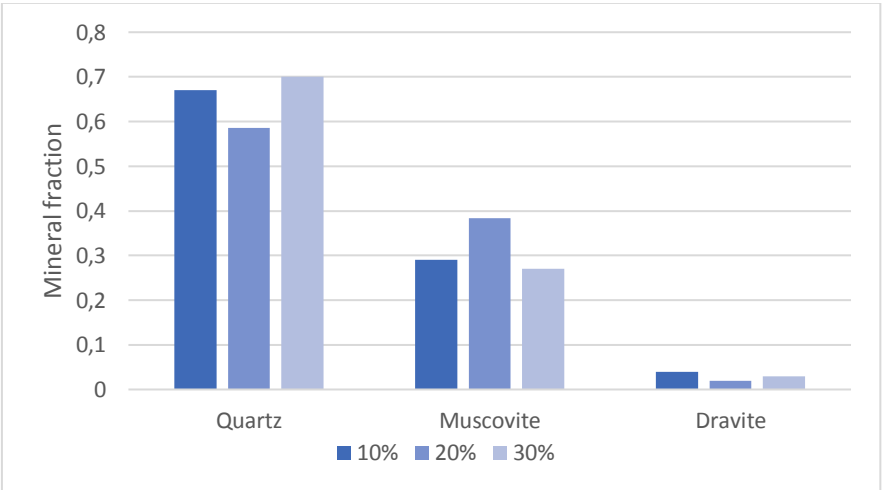

Figure 77. Mineralogical composition for a particle size range of 16-11.2 mm and different compression ratios

In Figure 79 the mineralogical concentration of the same three minerals as before in the particle size in the range of 1-0.5 mm is represented depending on the compression ratio for the values of 10, 20 and 30%. In this case, Quartz and Muscovite behave in the same way as in Figure 78, however Dravite decreases with the increasing compression ratio.

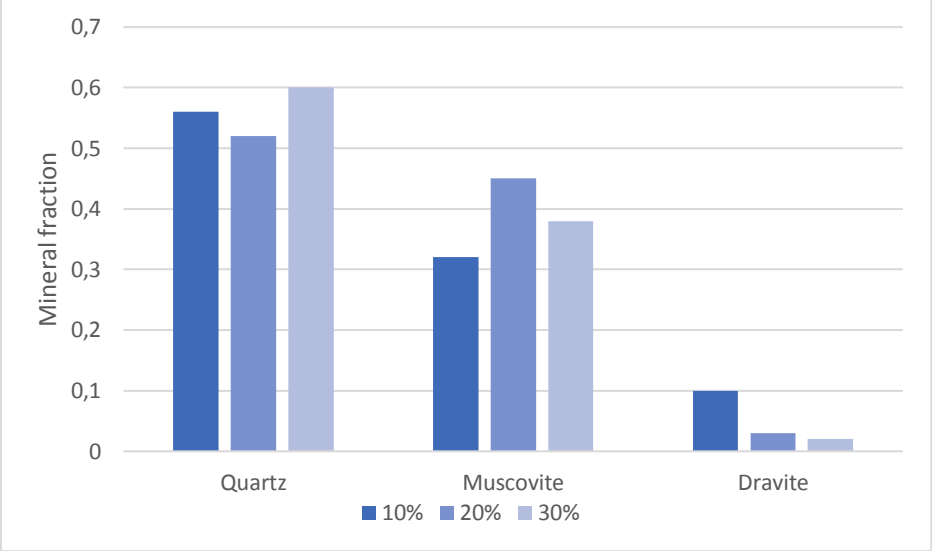

Figure 78. Mineralogical composition for a particle size range of 1-0.5 mm and different compression ratios

In Figure 80 the mineralogical concentration of the same three minerals again in the particle size in the range of 0.25-0.125 mm is represented depending on the compression ratio for the same three values. For this situation, Quartz and Muscovite function equally to both of the previous cases and Dravite's concentration increases for the increasing compression ratio.

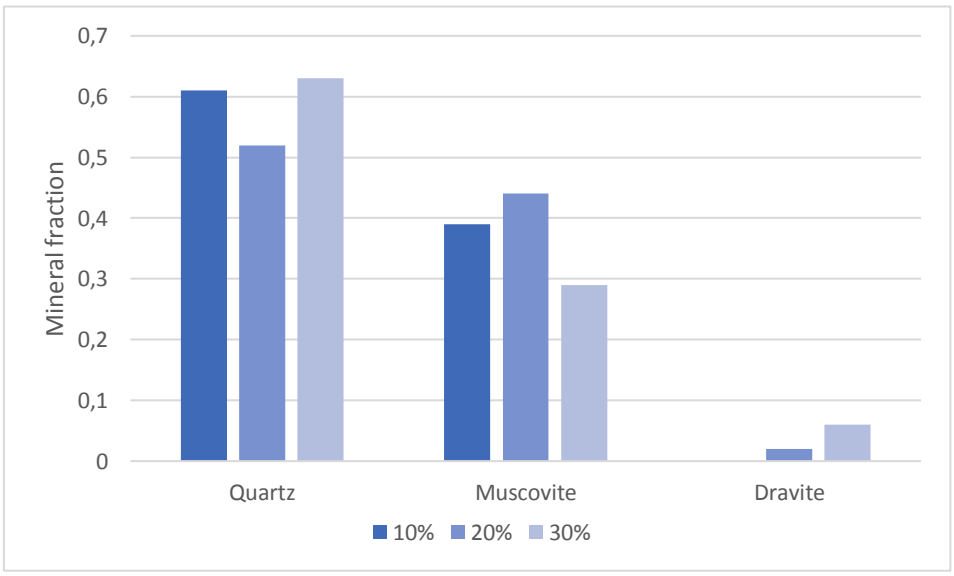

Figure 79. Mineralogical composition for a particle size range of 0.25-0.125 mm and different compression ratios

After analysis the results represented previously, there seems to be no correlation for the Dravite phase. The Quartz content is lower at the intermediate compression ratios and higher at the extremes. The opposite situation explains the behaviour of the Muscovite concentration, it is lower at the extremes and higher for intermediate compression ratios. These are behaviours difficult to comprehend and the author could not think of any logical explanation for it, yet it is what the numbers show repeatedly in up to three occasions. This is the relation for the concentration of Quartz and Muscovite and the compression ratio, regardless of the particle size.

The sample is a granitic rock dominated by Quartz *(SiO_2)* and Muscovite *($KAl_2(Si_3Al)O_{10}(OH,F)_2$)* minerals and with a noteworthy fraction of Dravite *($NaMg_3Al_6(BO_3)_3Si_6O_{18}(OH)_4$)* and a small proportion of Kaolinite *($Al_2Si_2O_5(OH)_4$)*, Cassiterite *(SnO_2)* and Petalite *($LiAlSi_4O_{10}$)*. The main metal ores are Scheelite *($CaWO_4$)* and Ferberite *($Fe^{2+}WO_4$)*. The high content in silicon that contains the sample, according to the chemical composition quantitative methods is confirmed by the diffraction analysis, five out of the six minerals with a higher concentration are of the silicates group, and therefore they contain large amounts of the element.

Not many grains containing tungsten were found during the SEM analysis, the main reason for this is the low concentration of said metal in the samples. When analysing the polished sections with the SEM, for case of the coarse particle sizes (>1 mm) no tungsten was found and the lower the particle size range of the polished slab, the higher amount of tungsten grains were identified. This matches with the results of Chapter 5.4. where the concentration of tungsten in each particle size for 20 of s/b is shown.

The larger number of ore grains were found in the size range of 0.125-0.063 mm, followed by the size range of 0.25-0.125 mm and so on. A notable number of liberated particles were identified at a size smaller than 0.25 mm, for particles bigger than this size all the ore grains form composite particles with gangue minerals. The biggest liberated particle has a rough area of 15000 μm^2.

Ferberite is basically found forming two different patterns. The most common is a vein-like type. Ore veins are mostly found at grain boundaries, meaning that when the material has been subjected to compressive forces cracks have created and developed through them until the particle was broken. The most common mineral associated with Ferberite when there is vein-like pattern is Quartz, the veins are in a large matrix of Quartz and in occasions with Pyrite veins in the proximity. In some occasions the Quarts is accompanied by Muscovite in the contact with

the tungsten ore. Sometimes Ferberite is in contact with alteration mineral containing As, Fe and K, which come from the alteration of Pyrite and Arsenopyrite.

The second most common pattern is simple intergrowth or mottled intergrowth. It is usually accompanied Quartz and in a lesser probability by Muscovite, in an occasion it a Ferberite grain of simple intergrowth was found with Cassiterite.

Summarizing, Ferberite can be found forming a vein-like pattern, and forming a simple intergrowth or a mottled intergrowth. The most common mineral in contact with Ferberite is Quartz, in either of both patterns, sometimes Muscovite is present in the contact zone too, and in a few occasions there is Pyrite, Arsenopyrite or alteration minerals of these two sulphides in contact or close to the Ferberite grains.

One can intuit that the Ferberite has been formed later than the sulphides surrounding it from a hot fluid that when it has been in touch with the sulphides it has altered them giving birth to alteration minerals such as Jarosite and Alunite.

The other tungsten ore is Scheelite, only two particles containing it were identified, one as a liberated particle and the other as a mottled intergrowth in a matrix of Muscovite. No conclusions can be drawn out of this amount of information, it would not be representative. However what can be stated is that liberation of Scheelite occurs in early stages of the process. We can also say that given the amounts of both minerals that have been found, it appears that Ferberite is more common than Scheelite in the material sample, although this in not ensured.

Different densities of the same tungsten mineral phase have been observed, this is due to inclusions and traces of light elements in the ore grain.

The amount of Pyrites and Arsenopyrites is notably high. Their alteration could generate environmental issues due to the creation of acid mine drainage. Sulphides are stable in a reducing environment but when they enter in contact with oxidising agents in the environment, such as oxygen in the air and water, they are oxidised. All sulphides are oxidised, however Pyrite suffers this reaction in a shorter time.

When sulphides are oxidised they form sulphates and the Fe in solution as Fe^{+2}. Then if oxygen is abundant Fe^{+2} reacts with it and forms Fe^{+3}, it is the ion that gives a reddish colour to the waters. Fe^{+3} does not give acidity to the water, what creates acid waters is the release of protons from the hydrolysis reaction in the same water.

What altered Pyrite does is to acidify the waters, nothing else. Acid water alone is not very bad, people drinks Coca Cola, and lemon juice, and many other acid drinks. The problem with acid water is that it can transport a large quantity ions in solution, while neutral water cannot. It is problematic for the vegetation because when acid water goes through the soil it washes away all the nutrients. For the same principle when a water reservoir is polluted with acid waters, and people drink from it there is the possibility that it contain heavy metals in solution.

Arsenopyrite also reacts and is altered like the Pyrite, with the added problem that it contains arsenic, a poisonous substance.

Pyrite in a botryoidal-like shape has been distinguished, the botryoidal configuration is formed by an enormous number of crystallites in a whole mass. This makes it easier for its alteration, due to the fact that there is a larger surface exposed to the elements, hence the oxidation reaction is accelerated.

7. Conclusions

The crushing stages of a processing plant can be set with very little knowledge of comminution and the processed material, and it will work anyway. Because coarse comminution looks simple at a first contact with it and the big particle size makes it easy to comprehend. Unlike the milling stages where the changes applied to the material can barely be seen with a naked eye, or flotation where chemical reactions take place and if one has not a broad knowledge in the matter will not comprehend a thing.

However, the coarse comminution stages can be optimised to a great extent. For doing it many hour of experimental work are needed, and even more time spent in modelling and simulations. The level of optimisation to be achieved with a bachelor thesis only can scratch the surface of real optimization. Yet in this research, the maximum amount of useful information has been collected and evaluated for a proper posterior modelling, that would take months only in programing, together with some suggestions and warnings that would be a first step into the deep optimization needed to achieve the standards set for the OptimOre Project.

Adding that, after this thesis it is expected that further research will be carried out with La Parrilla material, even so it can be stated that the characterization of the material has been completed for the greatest part, only lacking the mechanical characterization of the single particle breakage behaviour.

A notorious amount of liberated Scheelite and Ferberite particles were identified after a series of compressions for particles smaller than 0.25 mm, so that from early stages of the process, it is possible to achieve ore liberation. Due to the heavy density of tungsten mineral a pre-concentration by gravity separation could may be an interesting option for particles in the size range 0.25-0.063 mm.

The obtained selection and breakage functions were applied to each compression series test using a particle size distribution prediction model, and the simulated results match with high accuracy the tests results. Meaning that the calibration of the model has been performed correctly and that the characterized breakage behaviour can be used in simulations of repeated size reductions in any industrial compressive crusher model.

The content of tungsten in large particles is very low and with the results obtained is considered to be unpredictable. On the other hand, for smaller particles than 4 mm there is an inversely proportional exponential correlation linking tungsten concentration and particle size. Tungsten has been mainly identified in association with Quartz, and in occasions with Muscovite and iron sulphides. From the mineralogical results obtained, no apparent relation between mineral content and particle size has been appreciated.

The majority of the product obtained from the compressive crushing stages has an equidimensional grain morphology, some appear to have acquired an elongated shape and very little grains were identified with a needle-like morphology. Veins of Ferberite occur in the grain boundaries, this fact is due to the creation and propagation of cracks through the ore during the compressive forces. Using abrasive comminution techniques would make it easier to separate the ore without reducing the whole particle to the same size.

High amounts of Pyrite and Arsenopyrite occur in the material, sometimes they appear as altered minerals, therefore, the acid mine drainage is an important issue to have in mind when thinking of a low environmental impact mining exploitation. Worth mentioning amounts of other high-density minerals were found in the sample, such as Monazite, Zirconite, Ilmenite and Rutile and scarce amount of Galena. When designing a gravity concentration, it is necessary to take into consideration that these mineral phases will be difficult to separate.

References

Anawar, H., Garcia-Sanchez A., et al., 2006. *Exposure and bioavailability of arsenic in contaminated soils from the La Parrilla mine, Spain*. Environ. Geol. 50, 170-179.

Barnard,W. J. and Bull, F. A., 1979. *Primary Breakage of Brittle Particles*. Fourth Tewksbury Symposium, Melbourne, Australia.

Bengtsson, M., 2009. *Quality-Driven Production of Aggregates in Crushing Plants*. Dept. of Product and production Development. PhD Thesis, Chalmers University of Technology.

Bengtsson, M., et al., 2006. *Characterization of Compressive Breakage Behaviour*. XXIII International Mineral Processing Congress. 2006. Turkey. Promed. Advertising Agency.

Bengtsson, M., Quist J., et al., 2015. *Mineral mechanical characterization for crushers*. OptimOre Deliverable 3.2.

Bish, D.L., Post, J.E. (eds.) 1989. *Modern Powder Diffraction*, MSA Reviews in Mineralogy 20: Washington, Mineralogical Association of America, 384.

Bond, F. C., 1952. *The third theory of comminution*. Trans AIME, 193:484

Broadbent, S. R. and Callcott, T. G., 1956. *Coal Breakage Processes, I. A New Analysis of Coal Breakage Processes*. J. Inst. Fuel, 524-528.

Broadbent, S. R. and Callcott, T. G., 1956. *Coal Breakage Processes, II. A New Analysis of Coal Breakage Processes*. J. Inst. Fuel, 528-539.

Cullity, B.D., Stock, S.R., 2001. *Elements of X - Ray Diffraction*. Reading, Massachusetts, Addison-Wesley, 664.

De la Fuente, F., 2016. *30 años después: la nueva Parrilla*. W Resources.

Esteve, V. (ed.) 2006. *El método Rietveld*. Publicacions de la Universitat Jaume I, Colección “Ciències experimentals”, 9, 192.

Evertsson, C. M., 1995. *Prediction of Size Distributions from Compressing Crusher Machines*. Proceedings EXPLO 95 Conference, Brisbane, Australia, 173-180.

Evertsson, C. M., 1999. *Size Reduction in Cone Crushers*. Minerals Engineering Conference '99, Falmouth, England.

Evertsson, C. M., 1999. *Modelling of Flow in Cone Crushers*. Minerals Engineering, Vol. 12, 1479-1499.

Evertsson, C. M., 2000. *Cone crusher performance*. Dept. of Machine and Vehicle Design. PhD Thesis, Chalmers University of Technology.

Guldris, L., et al., 2016. *Mineralogical characterization, reduction and liberation analysis of tungsten ore*. Emerging Trends in Mineral Engineering Conference, London, UK.

Guldris, L., et al., 2016. *Reduction and fracture analysis of a tungsten ore and its use for fundamental liberation modelling*. XII International Mineral Processing Conference. Procemin 2016.

Gumiel, P., 1984. *Tipología de los yacimientos de estaño y wolframio del Macizo Ibérico*. I Congreso Español de Geología, 183-216.

Gumiel, P., Campor, R., Sanderson, D.J., Roberts, S., 1995. *Geometría y fractalidad de los sistemas filonianos de la mina de La Parrilla (Cáceres): conectividad y percolación*. Bol. Geol. Min. España, 106(4), 316-337.

Gumiel, P., Pineda, A., 1981. *Estudio del Yacimiento de scheelita de La Parrilla (Cáceres-Badajoz)*. Revista española de geología y minería, Dec–Jan, year 7, nº 39, 16–38.

Gupta, A., 2016. *Mineral Processing Design and Operations*. Elsevier.

Hukki, R. T., 1961. *Proposal for a Solomonic settlement between the theories of Von Rittinger, Kick and Bond*. Trans AIME (Mining), 403-410.

Hulthén, E., et al., 2006. *Theoretical optimal crushing*. XXIII International Minerals Processing Congress. Turkey, Promed Advertising Agency.

Inglis, C. E., 1913. *Stresses in a plate due to the presence of cracks and sharp corners*. Proc. Inst. Nav. Arch., LV: 219-230.

Junta de Extremadura, 2010. *Patrimonio geológico de Extremadura*. Consejería de Industria y Energía, Dirección General de Industria, Energía y Minas.

Kick, F., 1885. *Des Gesetz der Proportionalem wider-stand und Seine Anwendung (Principle of Proportional Resistance and Its Application)*. Felix: Leipzig.

Klimpel, R. R. and Austin, L. G., 1965. *The Statistical Theory of Primary Breakage Distribution for Brittle Materials*. Trans. SME/AIME, 232, 88-94.

Klug, H.P., Alexander, L.E., 1954. *X-Ray Diffraction Procedures for polycrystalline and amorphous materials*. New York, John Wiley and Sons, 716.

Lee, E., 2012. *Optimization of compressive crushing*. Chalmers University of Technology.

Lindqvist, M., 2008. *Energy considerations in compressive and impact crushing of rock.* Minerals Engineering. 21: 631-641.

Liu, J. and Schönert, K., 1994. *Modelling of Interparticle Breakage*. Preprints of 8th European Symposium on Comminution, Stockholm, Sweden, 102-115.

Liu, J. and Schönert, K., 1996. *Modelling of interparticle breakage.* International Journal of Mineral Processing. 44–45, 101-115.

Lynch, A., 2015. *Comminution handbook*. AusIMM The minerals institute.

Melgarejo, J. C., Proenza, J., et al., 2010. *Técnicas de caracterización mineral y su aplicación en exploración y explotación minera*. Bol. de la Sociedad Geológica Mexicana, vol. 62, nº 1, 1-23

Morrell, S., 2004. *An alternative energy–size relationship to that proposed by Bond for the design and optimisation of grinding circuits.* International Journal of Mineral Processing. 74(1–4): 133-141.

Partridge, A. C. 1978. *Principles of comminution*. Mine and Quarry, nº 7, Jul-Aug, 70.

Prasher, C., L., 1987. *Crushing and Grinding Process Handbook*. John Wiley and Sons Ltd.

Quist, J., 2017. *DEM Modelling and Simulation of Cone Crushers and High Pressure Grinding Rolls*. Chalmers University of Technology.

Rosin, P. and Rammler, E., 1933. *The Laws Governing the Fineness of Powdered Coal*. J. Inst. Fuel, Vol. 7, 29-36.

Schönert, K. and Müller, F., 1990. *Representation of Breakage Fraction and Breakage Function of Inter-Particle Stressing.* Aufbereitungs-technik. 31(5): 248-256.

Schönert, K., 1979. *Aspects of the Physics of Breakage Relevant to Comminution*. Proc 4th Tewksbury Symposium, Melbourne, Australia.

Schönert, K., Vogel, L., and Peukert, W., 2002. *Separation of the Influences of Material and Machine in Impact Comminution - Modelling with Population Balances.* Aufbereitungs Technik. 43(8): 19-30.

Vogel, L. and Peukert, W., 2003. *Breakage behaviour of different materials—construction of a mastercurve for the breakage probability.* Powder Technology. 129(1–3): 101-110.

Vogel, L. and Peukert, W., 2004. *Determination of material properties relevant to grinding by practicable labscale milling tests.* International Journal of Mineral Processing. 74: 329-338.

Von Rittinger, P. R., 1867. *Lehrbuch der Aufbereitungs Kunde*. Ernst and Korn: Berlin.

8. Appendix

Appendix A. Product particle size distribution of IPB test

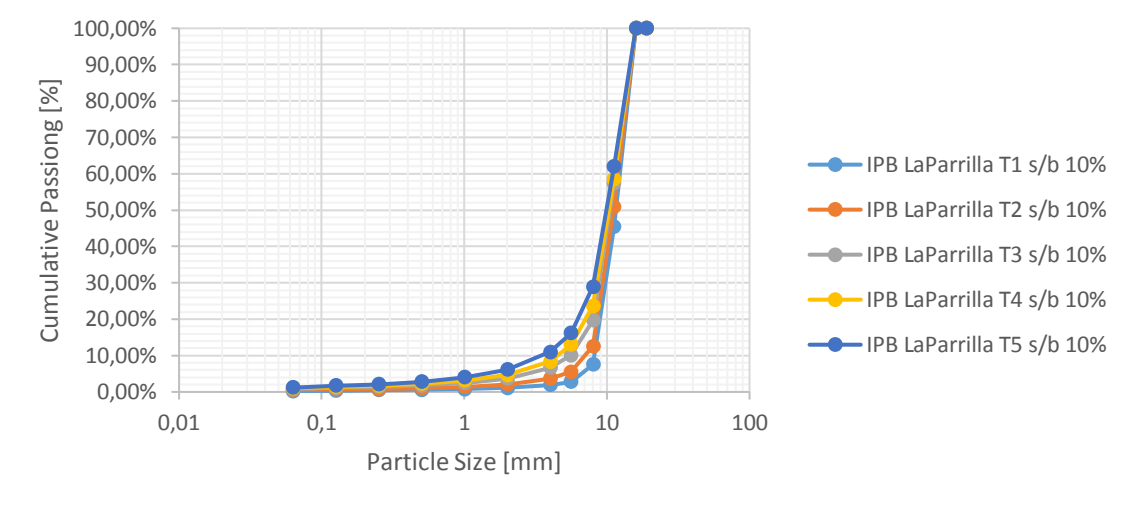

Figure A 19. Cumulative PSD of 10% of s/b series

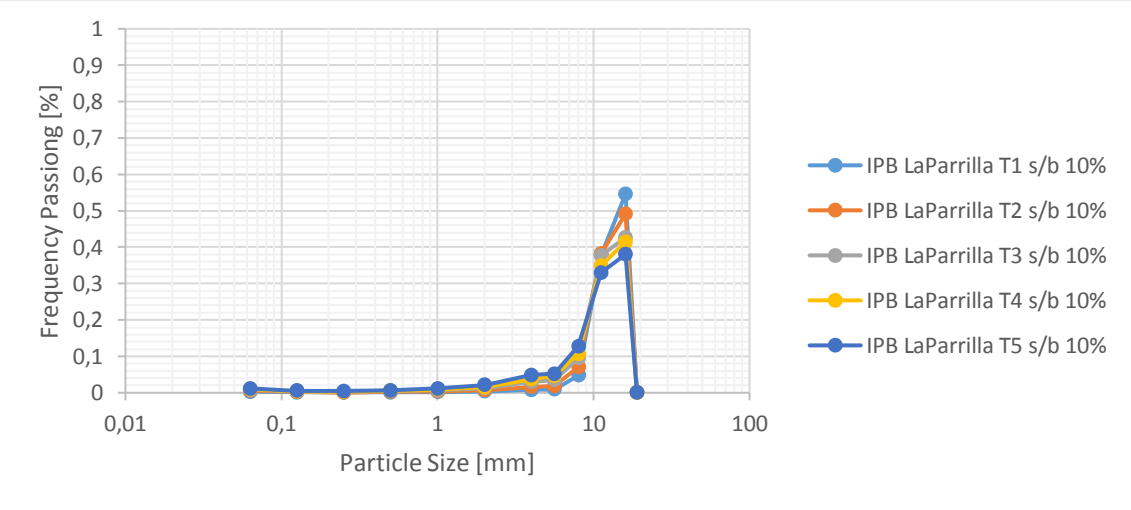

Figure A 20. Frequency PSD of 10% of s/b series

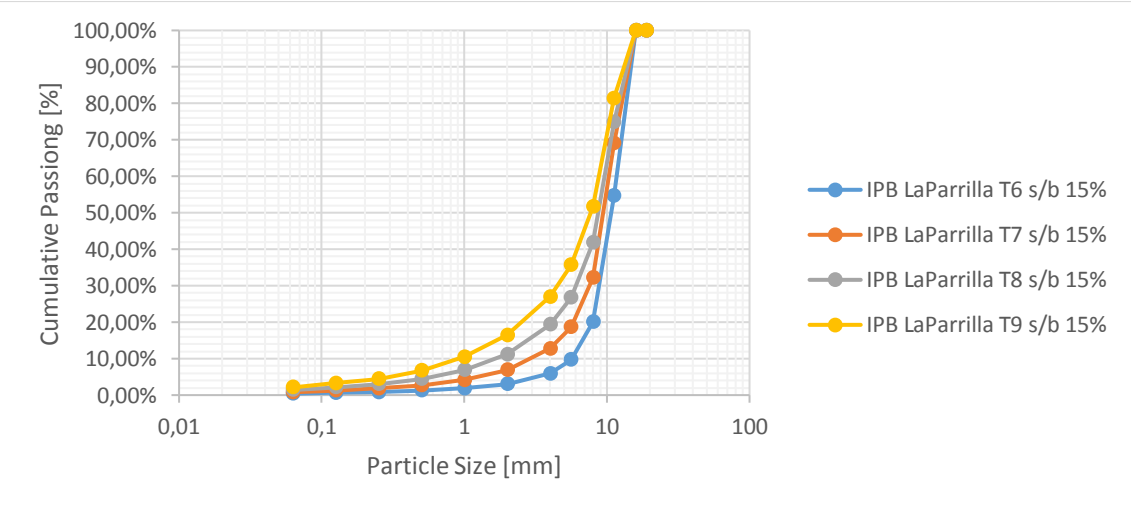

Figure A 21. Cumulative PSD of 15% of s/b series

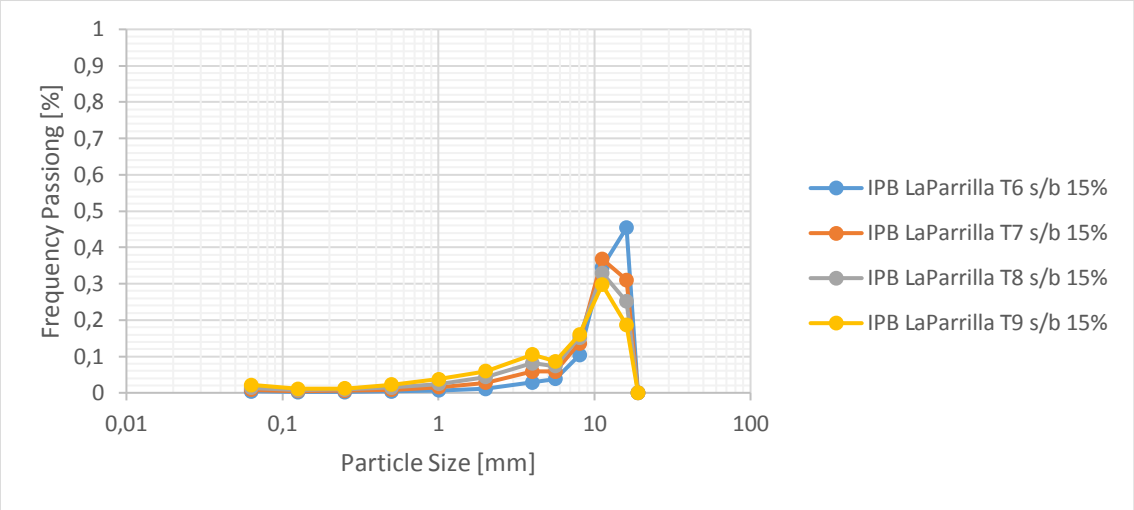

Figure A 22. Frequency PSD of 15% of s/b series

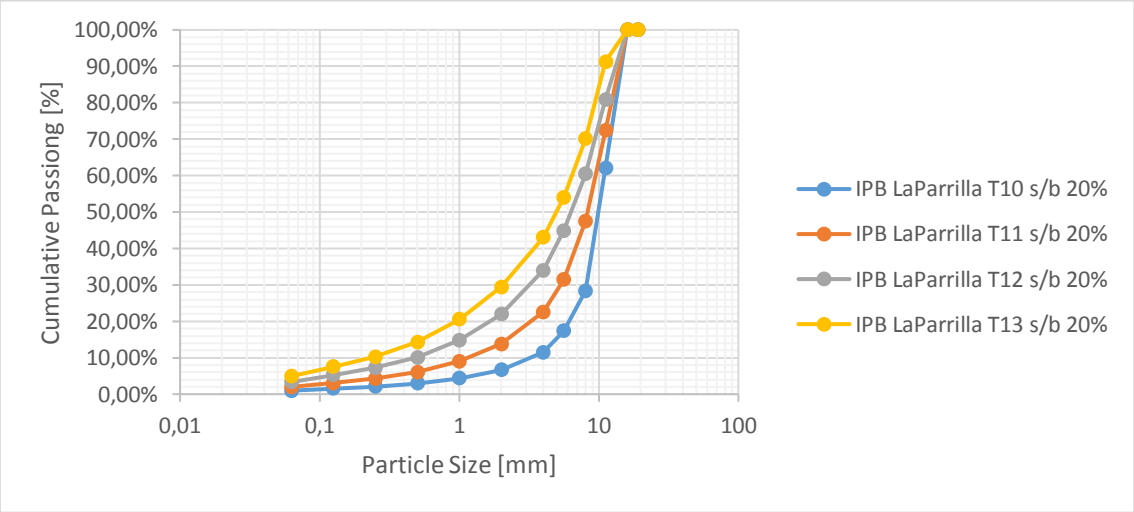

Figure A 23. Cumulative PSD of 20% of s/b series

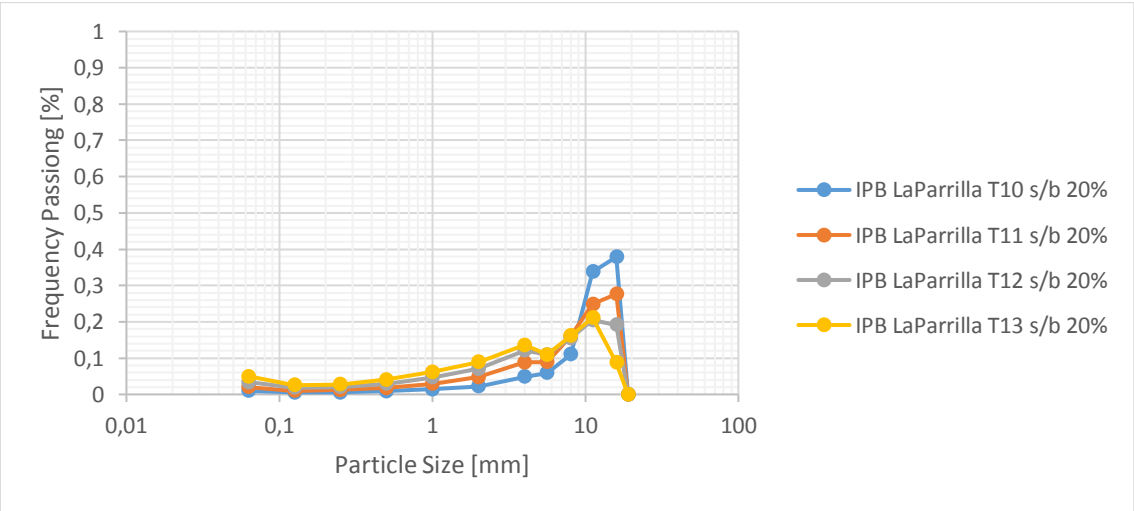

Figure A 24. Frequency PSD of 20% of s/b series

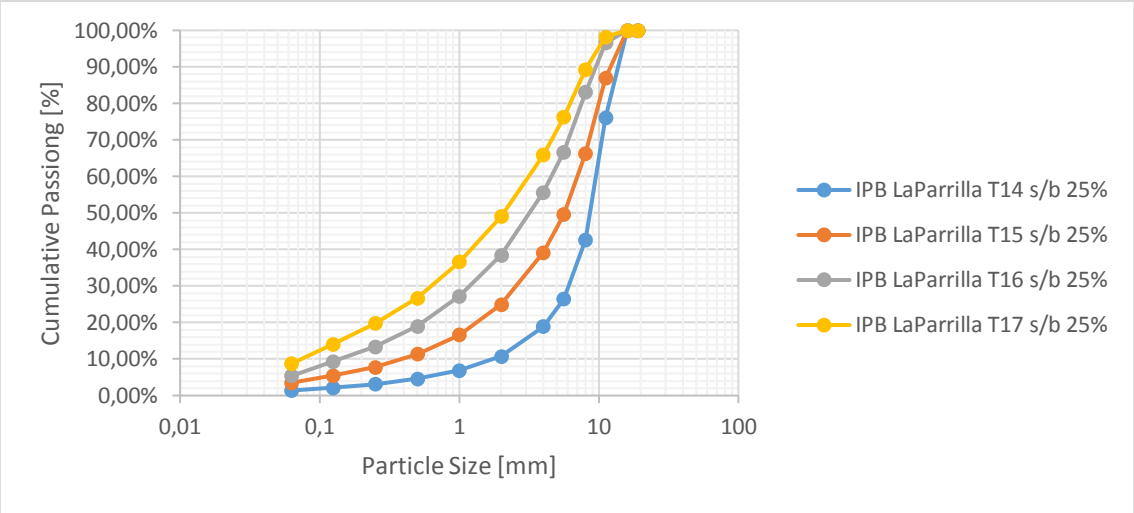

Figure A 25. Cumulative PSD of 25% of s/b series

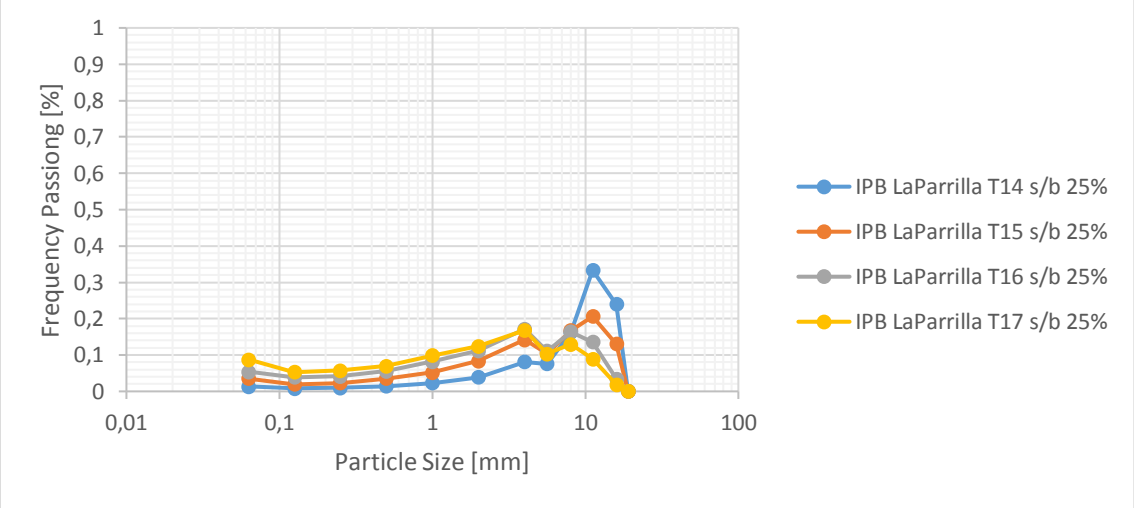

Figure A 26. Frequency PSD of 25% of s/b series

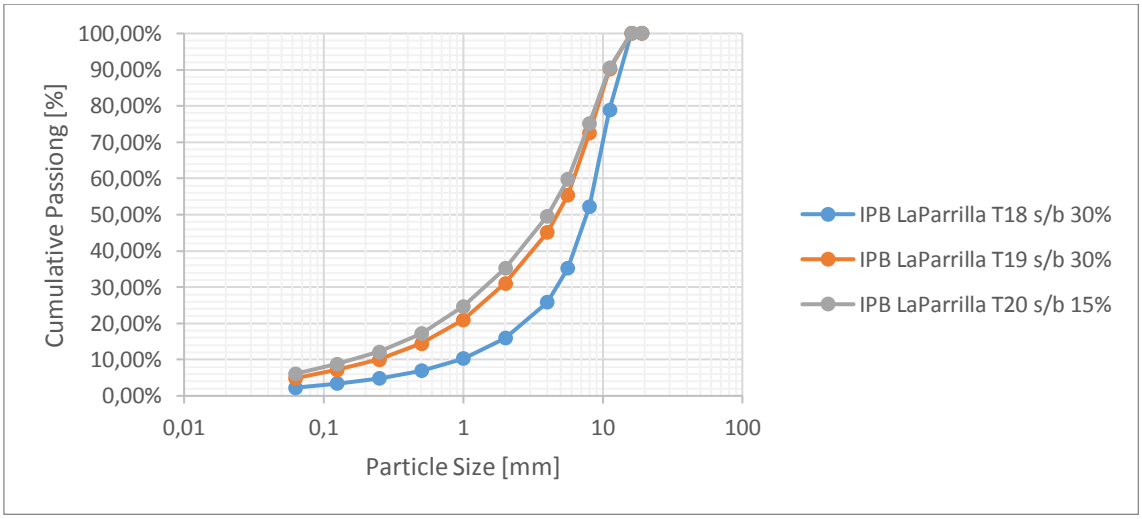

Figure A 27. Cumulative PSD of 30% of s/b series

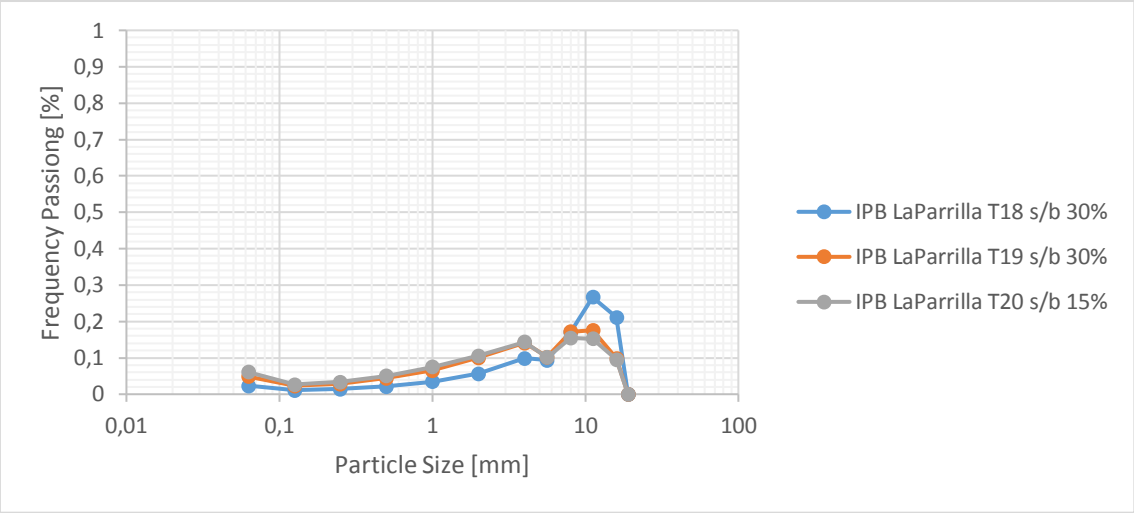

Figure A 28. Frequency PSD of 30% of s/b series

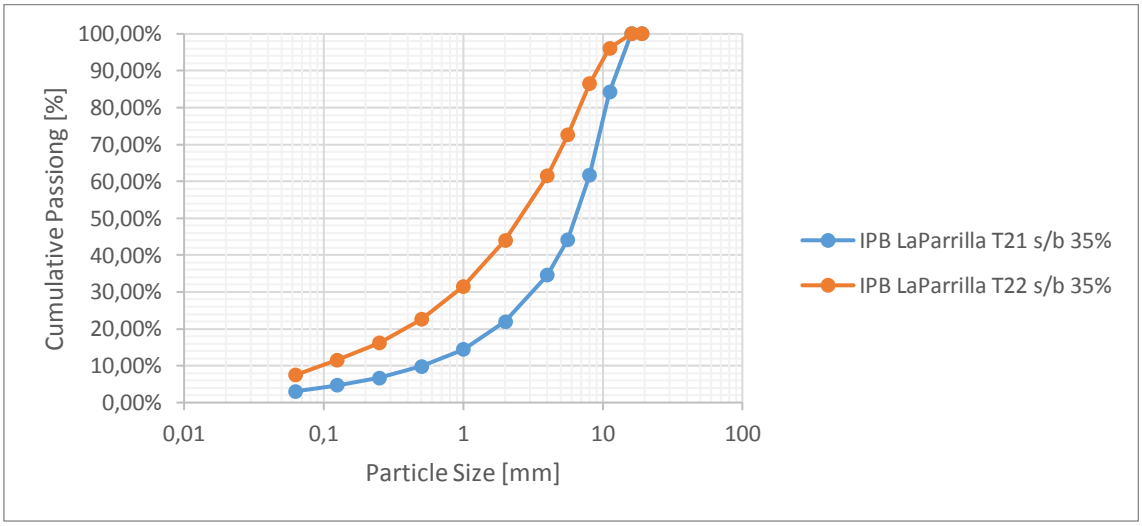

Figure A 29. Cumulative PSD of 35% of s/b series

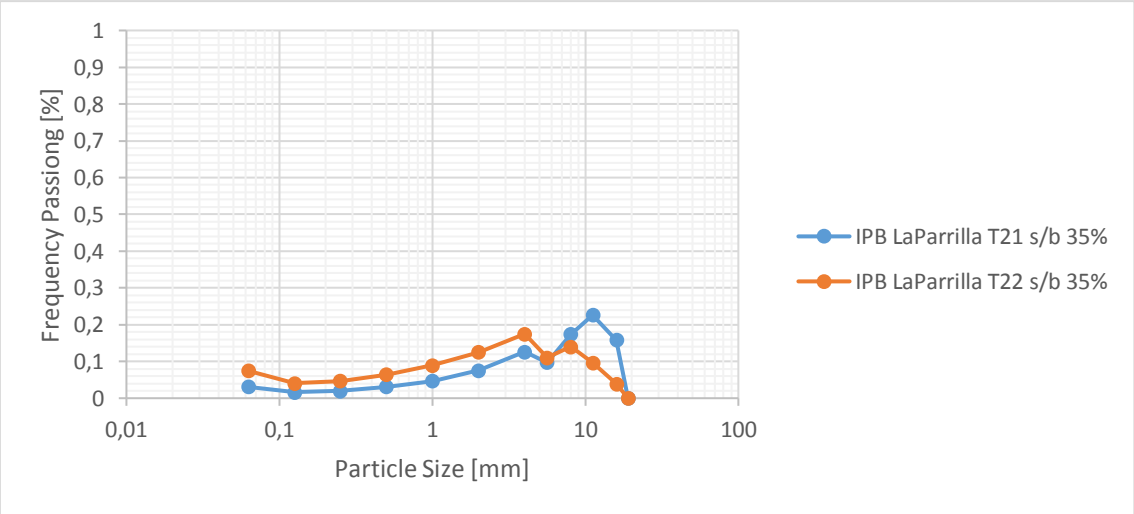

Figure A 30. Frequency PSD of 35% of s/b series

Appendix B. Force-displacement plots for IPB test series

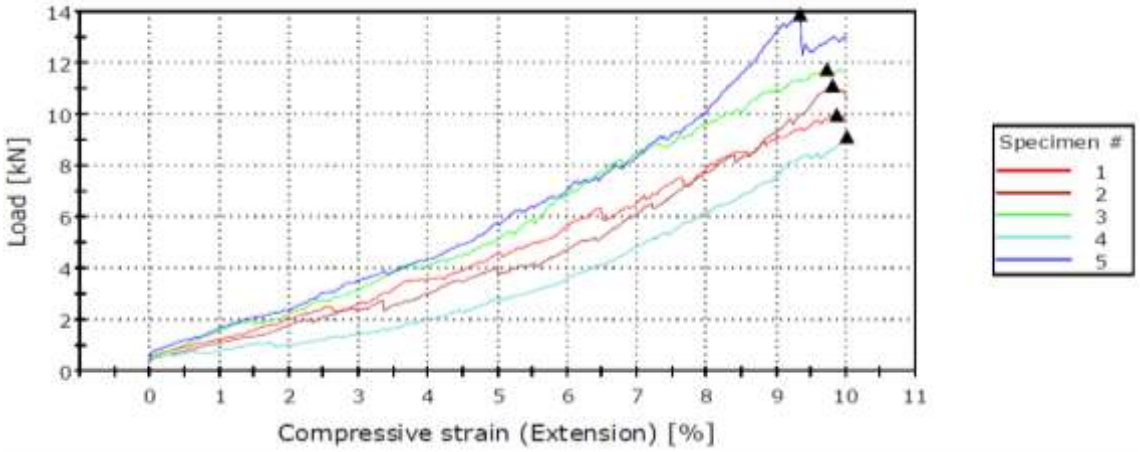

Figure A 31. Force-displacement plot for the 10% compression ratio IPB test series

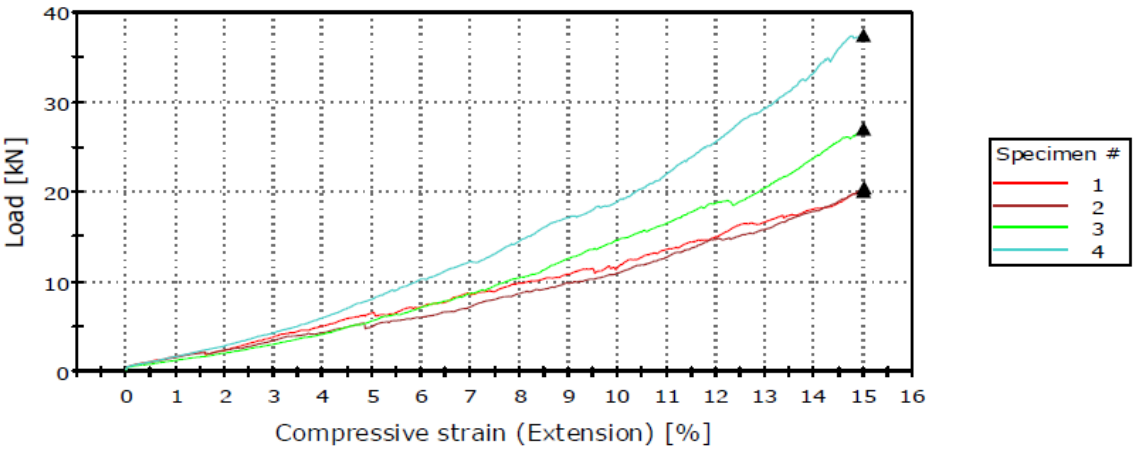

Figure A 32. Force-displacement plot for the 15% compression ratio IPB test series

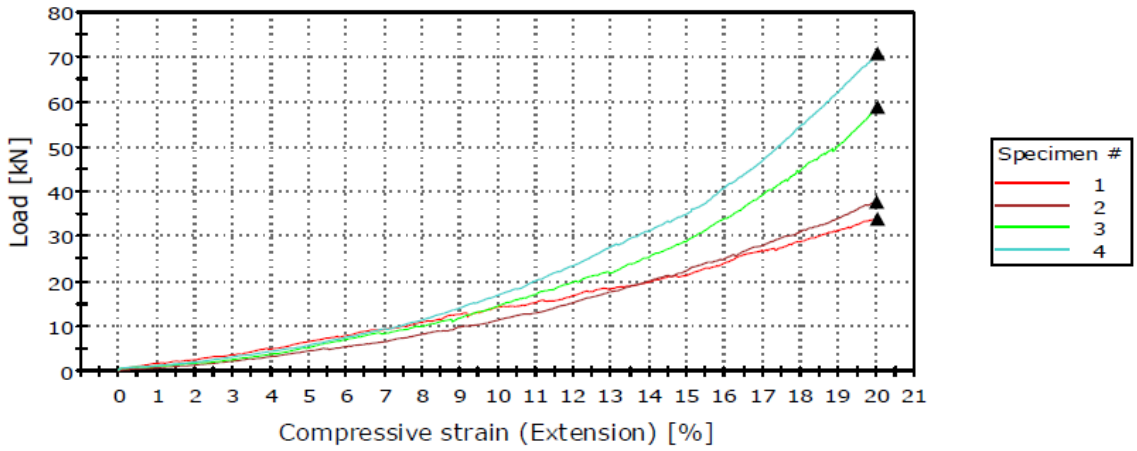

Figure A 33. Force-displacement plot for the 20% compression ratio IPB test series

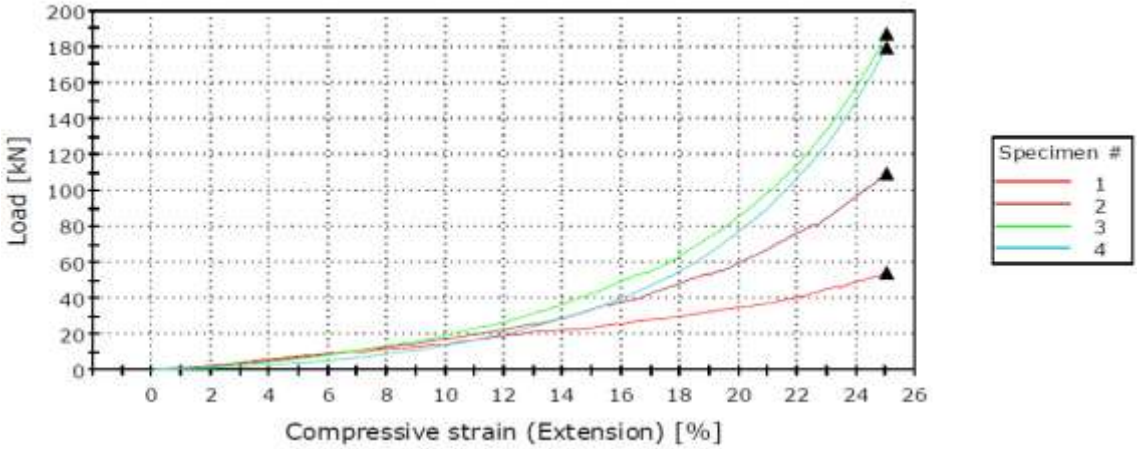

Figure A 34. Force-displacement plot for the 25% compression ration IPB test series

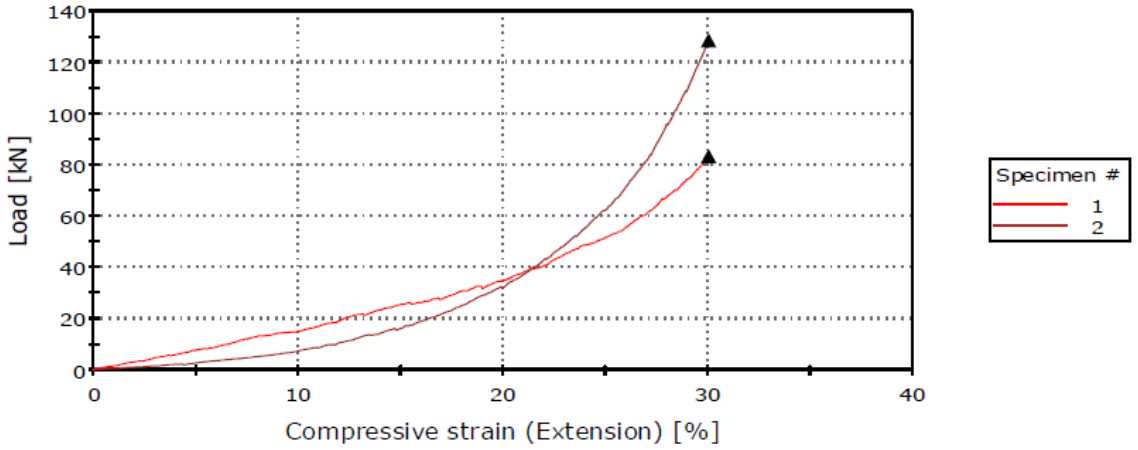

Figure A 35. Force-displacement plot for the 30% compression ratio IPB test series

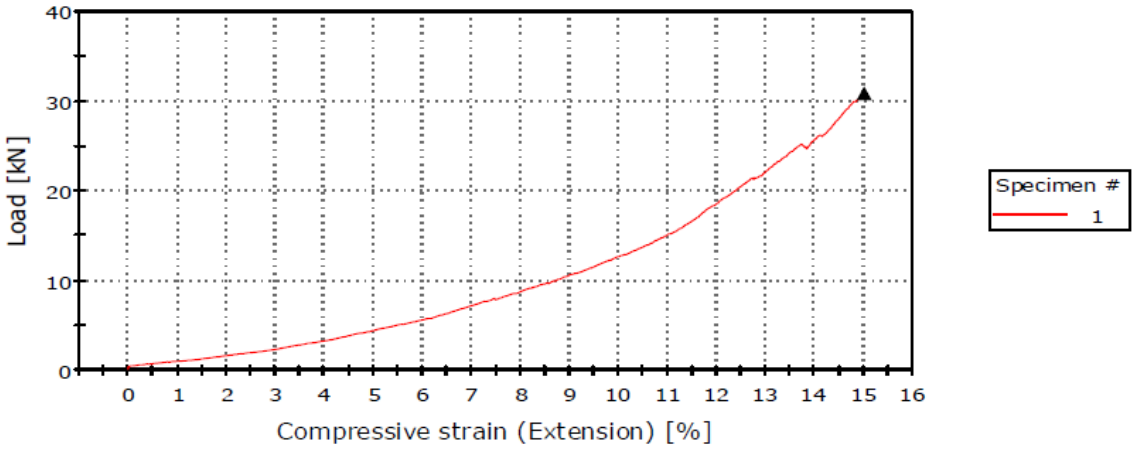

Figure A 36. Force-displacement plot for the 15% compression ratio in the 30% IPB test series

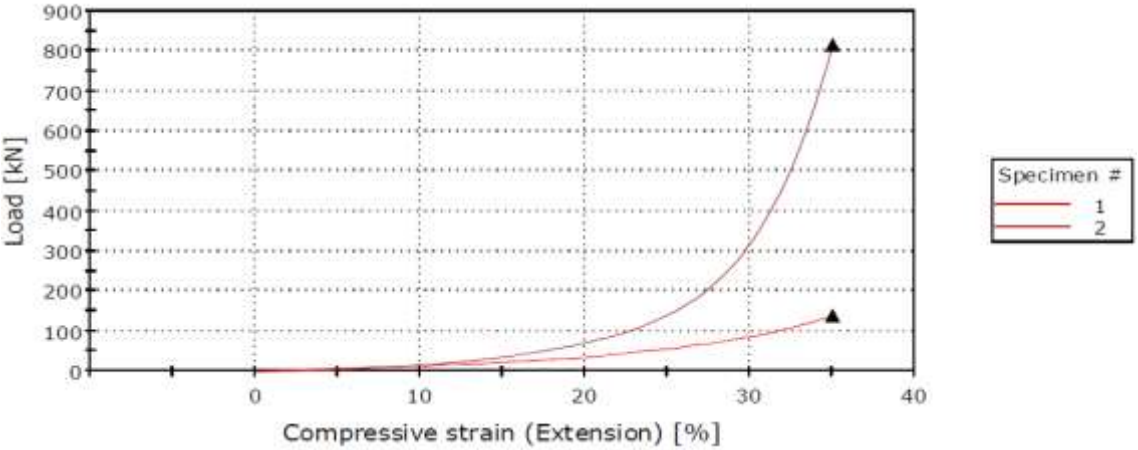

Figure A 37. Force-displacement plot for the 35% compression ration IPB test series